Plasmonic effects of gold nanostructures in organic solar cells

By

Tlangelani Shalot Ngunyulu

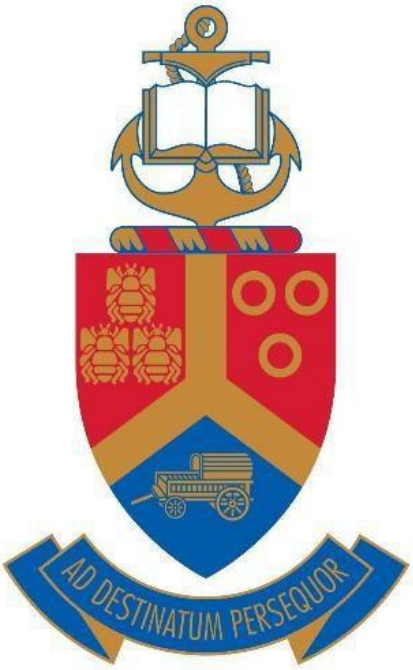

Submitted in partial fulfilment of the requirements

for the degree

Master of Science (MSc) in Physics

in the

Faculty of Natural and Agricultural Sciences

Department of Physics

University of Pretoria

Supervisor: Prof MM Diale

Declaration

I, **Tlangelani Shalot Ngunyulu**, declare that the dissertation, I hereby submit for the degree of Master of Science (MSc) in Physics at the University of Pretoria, is my work and has not been submitted previously by me for a degree at this or any other institution. Any work of others that have been drawn upon is duly cited in the text, and a list of references is presented at the end of every chapter.

Signature: 

Date: 06 May 2022

Student number: 15073212

Abstract

Gold (Au) nanospheres, nanorods and nanoprisms were synthesized using the seed-mediated growth method. The structural, optical, and morphological properties of Au nanostructures were explored. Transmission electron microscope (TEM) and scanning electron microscope (SEM) were used to identify the shape and size of Au nanostructures. The average diameters ofAu nanospheres (AuNSs) and Au seeds were 6 and 4 nm, respectively. Au nanoprisms with average edge length of 68 nm and Au nanorods (AuNRs) with an average length of 70 and width of 40 nm (aspect ratio of 1.9) were obtained. In UV-Vis spectra, plasmon absorption peaks of these nanostructures were located in the range of 395 to 629 nm for Au seeds (with the smallest sizes) to AuNRs (with largest sizes). X-ray diffraction (XRD) confirmed the face-centered cubic crystalline structure of Au, while Raman showed strong vibrational modes. Additionally, the structural, optical, and morphological properties of Poly[N-9'-heptadecanyl-2,7-carbazole-alt- 5,5-(4',7'-di-2-thienyl-2',1',3'-benzothiadiazole)]:[6,6]-Phenyl-C61-butyric acid methyl ester (PCDTBT: $PC_{70}BM$) layers with AuNSs, AuNRs, and Au nanoprisms were characterized.UV-Vis spectra were obtained within the absorption range of 378 – 564 nm. PCDTBT: $PC_{70}BM$ with Au nanoprisms absorbed at high intensity in comparison to the other samples. SEM micrographs revealed compact morphology with pin-hole defects. XRD and Raman analysis showed no crystalline domains. The electron transport layer, titanium dioxide (TiO_2) and hole transport layer, poly(3,4-ethylenedioxythiophene) polystyrene sulfonate (PEDOT: PSS) were spin-coated and characterized. PCDTBT: $PC_{70}BM$ based organic solar cells (OSCs) were fabricated with Au nanostructures were incorporated between the electron-hole transport layer and the active layer. Analysis of the electrical characteristics of the devices was done using current density voltage (J-V). Power conversion efficiency (PCE) for the pristine device was 2.04 %, while AuNSs with plasmonics achieved 1.19%. A month after fabrication, the PCE for pristine and plasmonic devices with AuNSs increased to 2.08 and 1.72%, respectively. When compared to the other plasmonic devices, the device with AuNSs performed the best.

List of Abbreviations

OSCs	organic solar cells
AM	air mass
Au	gold
AuNSs	gold nanospheres
AuNRs	gold nanorods
BHJ	bulk heterojunction
HOMO	highest occupied molecular orbital
LUMO	lowest occupied molecular orbital
ETL	electron transport layer
EDS	energy dispersive x-ray spectroscopy
HTL	hole transport layer
ITO	indium-doped tin oxide
VB	valence band
PCE	power conversion efficiency
$PC_{70}BM$	[6,6]-Phenyl-C70-butyric acid methyl ester
PEDOT: PSS	poly(3,4-ethylenedioxythiophene) polystyrene sulfonate
TEM	transmission electron microscopy
FE-SEM	field emission scanning electron microscopy
XRD	X-ray diffraction
PV	photovoltaic
TiO2	Titanium dioxide
SPR	surface plasmon resonance
LSPR	localized surface plasmon resonance

Dedication

To my lovely parents; Elliot and Roinah Ngunyulu for the love, prayers, endless support and giving me the best education foundation possible.

&

To my lovely siblings and niece; Nkateko, Kulani and Enelo Ngunyulu for unwavering love, support, and prayers.

Acknowledgements

Firstly, I would like to thank my heavenly Father, the Almighty God for life, protection, guidance, strength, wisdom, knowledge, understanding, love, and grace during my entire period of study.

I would like to extend my gratitude to my supervisor Prof. Mmantsae Moche Diale for taking me to be her student. I am grateful for her generous support, guidance positive criticism, and weekly teachings on academic writing. I thank Prof. for her determination, patience, encouragement, and motivation always.

To all the members of the Clean and Green Energy Research group, I thank you for the support, friendship, constructive criticism, and friendships. I thank Dr. Justine Sageka Nyarige, for the guidance, support, and patience in helping me with the synthesis and characterization of nanostructures. I would also like to thank Dr. Juvet Nche Fru, for the guidance, support, and patience in helping with the fabrication and electrical characteristics of solar cells. I extend this gratitude to Prof. Chris Theron the Head of the Physics Department. I thank the Chemistry Department for allowing me to use their labs and XRD equipment. Sincere gratitude to all the workers in the laboratory for microscopy and microanalysis for their help in TEM, SEM, and EDS equipment. I thank the National Research Foundation (NRF) innovation master's scholarship for funding and Grant Cost Centre N0115/115463 of NRF-SARCHi.

Finally, I would like to thank my lovely parents, Elliot and Roinah Ngunyulu, my siblings, my niece, friends, and entire family for the unwavering support, love, encouragement, and motivation during my entire period as an MSc student.

Table of Contents

List of Figures

List of Tables

Chapter 1

Introduction

1.1 Background and motivation

There has been an increase in energy demand which has resulted from the growth in the world population and industrialization. Reports have shown that in developed and developing countries, the energy consumption grows exponentially at a rate of 1 to 5% per year [1]. The primary source of energy, especially in heating, production, and transportation is fossil fuels [2]. However, the disadvantages of using fossil fuels are the release of carbon dioxide (CO_2) and other greenhouse gases that have led to a drastic climate change and global warming [3-5]. Climate change and global warming are a concern because of their impact on life and changing weather patterns. Some of the fossil fuels currently used, include oil, coal, and natural gas [6]. Therefore, moving to renewable energy can help to reduce greenhouse gas emissions and hence save our environment [7].

Renewable energy research has gained more attention in recent decades due to the increase in global energy consumption. Recently, renewable energy sources have been estimated to be 17.9% of global energy consumption in 2018 and 27.3% of global electricity production in 2019 [8]. Renewable energy has become more attractive in producing electricity and it is considered an environmentally friendly resource. These includes hydro, wind, and solar energy, to mention but a few [9]. Solar energy is captured by photovoltaics (PV) devices like solar cells, converted to electricity, and stored in batteries. It is a clean source from the sun, which is eco-friendly (green energy) and has advantages including abundance, and limited impact on the environment [9]. In addition, renewable energy technologies turn these natural energy sources into forms of energy such as heat, fuels, and electricity [7].

Solar PV systems directly convert solar energy into electricity [7]. Over the years, research has been conducted to manufacture various types of solar cells like silicon (Si), cadmium telluride (CdTe), and organic solar cells (OSCs) [10]. Most inorganic solar cells such as silicon with power conversion efficiency (PCE) between 22 and 31% have been commercialized [10]. However, disadvantages of inorganic solar cells are high-cost production [10, 11].

Organic solar cell (OSC) as the new generation of PV devices have become of interest in the renewable energy field because they offer a promising alternative to inorganic solar cells, due

to their unique advantages such as lightweight, low cost, flexibility, tunability of energy level, and large surface area [5]. In 1986, the first double-layer heterojunction OSCs with a PCE of 1% was designed by Deng [12]. The bulk heterojunction (BHJ) was proposed first in 1995 by Heeger to enhance the efficiencies of polymer photovoltaic cells [13]. From that time, different researchers investigated the design and performance of OSC, as shown in Figure 1. *1* the progress in power conversion efficiency (PCE) of OSCs over the years. The reported PCE of OSCs thus far has gone up to 18% [14].

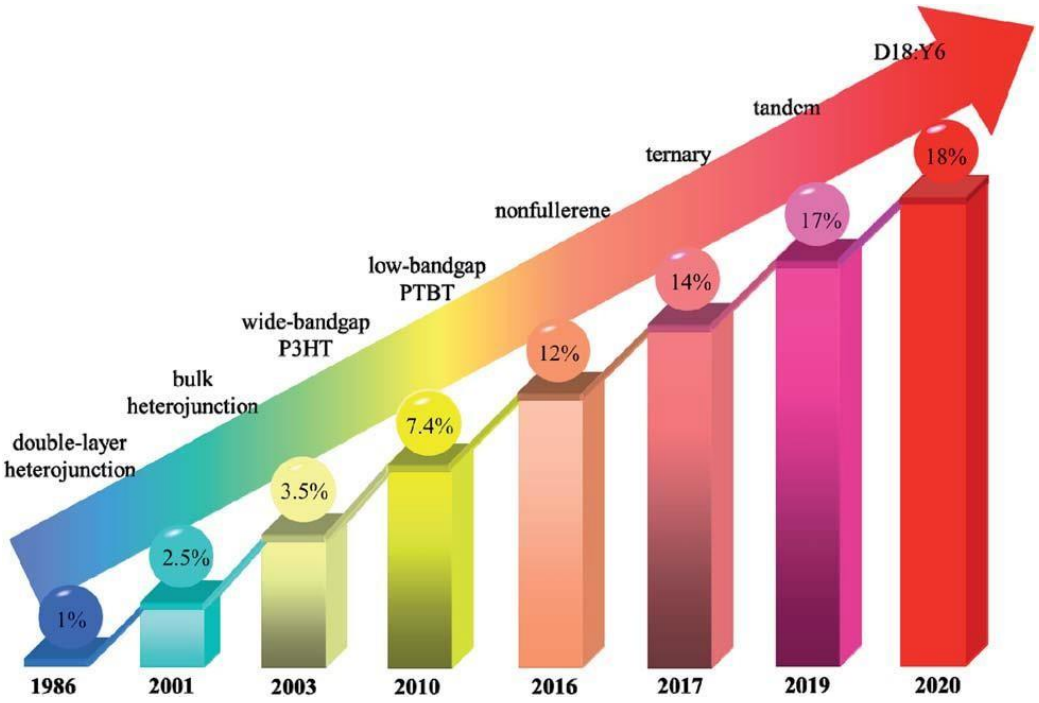

Figure 1. 1 The power conversion efficiency progress of organic solar cells [10].

Among various types of organic solar technologies, BHJ solar cells have high potentials due to their low cost and ease of fabrication. The BHJ structure is the blend of electron-accepting and electron-donating materials which consists of interpenetrating, channel-like domains of separated polymer and fullerene phases [15]. A study by Leclerc *et al.* demonstrated reproducible efficiencies of like Poly[N-9'-heptadecanyl-2,7-carbazole-alt-5,5-(4',7'-di-2-thienyl-2',1',3'-benzothiadiazole)]:[6,6]-Phenyl-C61-butyric acid methyl ester (PDCTBT: PCBM) of more than 3% [16]. PCDTBT is reported to have high solubility, good thermal stability, and near perfect internal quantum efficiency. Hence, PCDTBT-based solar cells have been investigated by different research groups and they demonstrate the high short-circuit current density and PCE, due to their ultrafast charge carrier generation [16, 17].

The performance of solar cells depends mainly on the active layer's ability to absorb incident light, the effectiveness of electron-hole dissociation and the collection of charge carriers [18]. However, there are major problems that contribute to the poor performance of OSCs such as low absorption in the near infrared (I-R) region and low mobility of charge carriers in the active layer [18]. The PCE and stability are still not sufficient for commercial applications [15]. Various approaches such as surface texturing [19], metal nanoparticles gratings [20], and resonance cavity [21] have been investigated to increase optical absorptions of OSCs [22]. Among these approaches, surface plasmon resonance (SPR) of metal nanostructures is one of the promising alternatives [23].

Plasmonics has generated interest in the last decade due to its unique properties. Metal nanoparticles (MNPs) exhibit a strong absorption band in the UV-visible region, which occurs when plasmons waves get excited on their surfaces [24]. The absorption is caused by the coherent oscillation of free electrons induced by the electromagnetic field [25]. The localized surface plasmon resonance (LSPR) effect of MNPs occurs when there is an interaction between incident light and the oscillating free electrons in MNPs [22]. Many research groups have reported the incorporation of MNPs into plasmonic OSCs to enhance the absorption and performance of the devices [26-28]. One of the ways of addressing the problem of absorption and efficiency of OSCs is using noble metals such as gold (Au), silver (Ag) nanoparticles in solar cell structures [29].

Since the dawn of metal nanoparticles, Au nanostructures have gained a lot of attention due to their unique properties such as strong absorption band, high luminescence, and excellent conductivity [30]. Since the properties of Au nanostructures are dependent on their size and shape, there has been continuous effort to control their sizes and shapes [31, 32]. Au nanostructures like nanospheres, nanowires, nanorods, nanocubes, and nanoprisms have been synthesized by different methods [33]. These nanostructures have been reported to enhance the performance of organic solar cells due to their surface modification, tunable sizes, and surface plasmon absorption properties [28, 34, 35]. For these reasons, the incorporation of Au nanostructures into polymer based OSCs can enhance PCE considerably.

1.2 Aims and objectives

This dissertation was aimed at comparing the effect of the synthesized Au nanospheres, nanorods, and nanoprisms on the performance of PDCTBT: $PC_{70}BM$ based organic solar cells. The objectives are as follows:

i. Synthesis of Au nanostructures using the seed-meditated growth method and study their structural, optical, and morphological properties.
ii. Study the structural, morphological, and optical properties of PCDTBT: $PC_{70}BM$ with the addition of Au nanospheres, nanorods and nanoprisms, titanium dioxide (TiO_2), and PEDOT: PSS on soda lime glass substrate.
iii. Fabricate the PCDTBT: $PC_{70}BM$ based OSCs and incorporate Au nanospheres, nanorods, and nanoprisms between electron transport layer and hole transport layer and study the effect of Au nanostructures on the electrical properties of the devices.

1.3 Structure of the dissertation

This dissertation is divided into five (5) chapters as follows:

Chapter 1 presents the background and motivation of this study, the aim, objectives, and the structure of the dissertation.

Chapter 2 reports on the literature review of plasmonic properties of Au nanostructures, working principle of OSCs, design, and architecture of OSCs, and applications of Au nanostructures in OSCs.

Chapter 3 gives a detailed description of the experimental methods, which includes synthesis of Au nanospheres, nanorods, and nanoprisms, preparation of PCDTBT: $PC_{70}BM$ with and without Au nanostructures, TiO_2 and PEDOT: PSS thin films, and fabrication of pristine OSCs and plasmonic devices.

Chapter 4 presents and discusses the results obtained from the synthesis and characterization of Au nanostructures. Structural, morphological, and optical properties result of the thin films are presented. Electrical properties of PCDTBT: $PC_{70}BM$ based OSCs and plasmonic devices are also discussed in this chapter.

Chapter 5 concludes and recommends possible future work.

References

1. Abu-Rumman, G., A.I. Khdair, and S.I. Khdair, *Current status and future investment potential in renewable energy in Jordan: An overview.* Heliyon, 2020. **6**(2): p. e03346.
2. Ağbulut, Ü. and S. Sarıdemir, *A general view to converting fossil fuels to cleaner energy source by adding nanoparticles.* International Journal of Ambient Energy, 2021. **42**(13): p. 1569-1574.
3. Kalair, A., et al., *Role of energy storage systems in energy transition from fossil fuels to renewables.* Energy Storage, 2021. **3**(1): p. e135.
4. Fernández-Solas, Á., et al., *Optical degradation impact on the spectral performance of photovoltaic technology.* Renewable and Sustainable Energy Reviews, 2021. **141**: p. 110782.
5. Wen, Z.-C., H. Yin, and X.-T. Hao, *Recent progress of PM6: Y6-based high efficiency organic solar cells.* Surfaces and Interfaces, 2021: p. 100921.
6. Shahbaz, M., et al., *The effect of financial development on renewable energy demand: The case of developing countries.* Renewable Energy, 2021. **178**: p. 1370-1380.
7. Ellabban, O., H. Abu-Rub, and F. Blaabjerg, *Renewable energy resources: Current status, future prospects and their enabling technology.* Renewable and sustainable energy reviews, 2014. **39**: p. 748-764.
8. Secretariat, R., *Renewables 2020 global status report.* Rep. Paris: REN12, 2020.
9. Mbungu, N.T., et al., *An overview of renewable energy resources and grid integration for commercial building applications.* Journal of Energy Storage, 2020. **29**: p. 101385.
10. Xu, H., et al., *Hole transport layers for organic solar cells: Recent progress and prospects.* Journal of Materials Chemistry A, 2020. **8**(23): p. 11478-11492.
11. Tong, Y., et al., *Progress of the key materials for organic solar cells.* Sci China Chem, 2020. **63**(6): p. 758-65.
12. Tang, C.W. and S.A. VanSlyke, *Organic electroluminescent diodes.* Applied physics letters, 1987. **51**(12): p. 913-915.
13. Yu, G., et al., *Polymer photovoltaic cells: enhanced efficiencies via a network of internal donor-acceptor heterojunctions.* Science, 1995. **270**(5243): p. 1789-1791.
14. Liu, Q., et al., *18% Efficiency organic solar cells.* Science Bulletin, 2020.
15. Mohammadnezhad, M., et al., *Hybrid PCDTBT: PCBM: Graphene-Nanoplatelet Photoabsorbers.* Journal of The Electrochemical Society, 2020. **167**(13): p. 136504.
16. Gendron, D. and M. Leclerc, *New conjugated polymers for plastic solar cells.* Energy & Environmental Science, 2011. **4**(4): p. 1225-1237.
17. Synooka, O., et al., *Influence of thermal annealing on PCDTBT: PCBM composition profiles.* Advanced Energy Materials, 2014. **4**(5): p. 1300981.
18. Alkhalayfeh, M.A., A.A. Aziz, and M.Z. Pakhuruddin, *An overview of enhanced polymer solar cells with embedded plasmonic nanoparticles.* Renewable and Sustainable Energy Reviews, 2021. **141**: p. 110726.
19. Campbell, P. and M.A. Green, *Light trapping properties of pyramidally textured surfaces.* Journal of Applied Physics, 1987. **62**(1): p. 243-249.
20. Yu, Z., A. Raman, and S. Fan, *Fundamental limit of nanophotonic light trapping in solar cells.* Proceedings of the National Academy of Sciences, 2010. **107**(41): p. 17491-17496.
21. Sergeant, N.P., et al., *Design of transparent anodes for resonant cavity enhanced light harvesting in organic solar cells.* Advanced materials, 2012. **24**(6): p. 728-732.

22. Baek, S.-W., et al., *Plasmonic forward scattering effect in organic solar cells: a powerful optical engineering method.* Scientific reports, 2013. **3**(1): p. 1-7.
23. Kang, M.G., et al., *Efficiency enhancement of organic solar cells using transparent plasmonic Ag nanowire electrodes.* Advanced Materials, 2010. **22**(39): p. 4378-4383.
24. Spyropoulos, G.D., et al., *Organic bulk heterojunction photovoltaic devices with surfactant-free Au nanoparticles embedded in the active layer.* Applied Physics Letters, 2012. **100**(21): p. 213904.
25. Souza, K.S., et al., *Interplay between Near-Field Properties and Au Nanorod Cluster Structure: Extending Hot Spots for Surface-Enhanced Raman Scattering.* Journal of the Brazilian Chemical Society, 2019. **30**: p. 2624-2633.
26. Kulkarni, A.P., et al., *Plasmon-enhanced charge carrier generation in organic photovoltaic films using silver nanoprisms.* Nano letters, 2010. **10**(4): p. 1501-1505.
27. Liu, C., et al., *Unique gold nanorods embedded active layer enabling strong plasmonic effect to improve the performance of polymer photovoltaic devices.* The Journal of Physical Chemistry C, 2016. **120**(11): p. 6198-6205.
28. Wang, D.H., et al., *Enhanced light harvesting in bulk heterojunction photovoltaic devices with shape-controlled Ag nanomaterials: Ag nanoparticles versus Ag nanoplates.* Rsc Advances, 2012. **2**(18): p. 7268-7272.
29. Kozanoglu, D., et al., *Power conversion efficiency enhancement of organic solar cells by addition of gold nanostars, nanorods, and nanospheres.* Organic Electronics, 2013. **14**(7): p. 1720-1727.
30. Sun, M., et al., *The effect of iodide on the synthesis of gold nanoprisms.* Journal of Experimental Nanoscience, 2015. **10**(17): p. 1309-1318.
31. Smitha, S., et al., *Size-dependent optical properties of Au nanorods.* Progress in Natural Science: Materials International, 2013. **23**(1): p. 36-43.
32. Zhang, Q., et al., *Facile synthesis of Ag nanocubes of 30 to 70 nm in edge length with CF3COOAg as a precursor.* Chemistry (Weinheim an der Bergstrasse, Germany), 2010. **16**(33): p. 10234.
33. Cramer, H.E., et al., *Shape-controlled gold nanoparticle synthesis*. 2013, army research lab aberdeen proving ground md weapons and materials research
34. Chang, H.-H. and C.J. Murphy, *Mini gold nanorods with tunable plasmonic peaks beyond 1000 nm.* Chemistry of Materials, 2018. **30**(4): p. 1427-1435.
35. Miranda, A., et al., *Synthesis of gold nanocubes in aqueous solution with remarkable shape-selectivity.* Journal of Porphyrins and Phthalocyanines, 2011. **15**(05n06): p. 441-448.

Chapter 2

Gold nanostructures in organic solar cells

2.1 Introduction

Gold (Au) nanostructures have recently been used in organic solar cells. These nanostructures are of advantage in solar cells because of their chemical, physical and optical properties. The shape and size of metal nanostructures are also important due to their effect on these properties. The use of Au nanostructures has shown an improvement in the efficiency of organic semiconductor devices. This chapter discusses the size, shape, synthesis methods, surface plasmons properties, working principle of organic solar cells, and the applications of Au nanostructures in organic solar cells that have been reported by other studies.

2.2 Gold nanostructures

Metal nanostructures (MNSs) are particles with a size range from 1 to 100 nm and are produced using noble metals such as gold (Au), silver (Ag), and copper (Cu). Noble metals have unique properties such as resistance to corrosion and oxidation, non-reactiveness, high reduction potential, high melting point, and high ionization energy [1]. Au has received special attention in nanoscience because of its physical and optical properties which can be manipulated by different processes effectively. These physical properties include electrical conductivity and quantum tunnelling effect [2, 3]. On the other hand, silver nanostructures (AgNSs) have plasmon absorption resonance bands at a shorter wavelength, absorb between 300 and 500 nm, compared to Au nanostructures [4, 5]. Similarly, the synthesis of copper nanoparticles (CuNPs) is not environmentally friendly, and copper is less stable compared to Au [6].

Au nanostructures outweigh other MNSs due to their stability under changing physicochemical conditions such as pH, temperature, and ionic strength [7]. Au nanostructures have a strong absorption band, high luminescent properties, and have plasmon resonance absorption band in the range of 500 to 800 nm [8]. These nanostructures have been used in sensing, photovoltaic, imaging, and therapeutics due to their tunable sizes, excellent optoelectronic properties, and straightforward surface modification [9-11]. Most applications of Au nanostructures depend on their optical properties that are in turn dependent

on size and shape [12]. Some of these optical properties are surface-enhanced Raman scattering (SERs) and surface plasmon resonance (SPR) [13].

2.2.1 Size of gold nanostructures

The size of Au nanostructures has a significant effect on the SPR and the optical properties [14]. Properties such as electrical conductivity, fluorescence, melting point, magnetic permeability, and chemical reactivity, change as the function of the size of the NSs [15, 16]. For example, Cao *et al.* [17] reported the dependence of optical and electrochemical properties on the size of gold nanoparticles (AuNPs). The results showed that with the increase in the size of the NPs, electrochemical oxidation potential was positively shifted (blue shift) and full width at half maximum in the ultraviolet-visible (UV-Vis) absorption spectrum increased. In another work, Pakravan *et al*. [18] reported the synthesis of seven different AuNPs such as rods, stars, hollow, cages, spheres, Fe-Au and Si-Au core shells and investigated the effect of shapes on their optical properties. They measured the photothermal heating capacity and found that all these AuNPs absorb and convert near-infrared light into heat. However, gold nanostars showed the lowest cytotoxicity and highest heat generation compared to the other structures. Properties of Au nanostructures are dependent on the size and shape. Hence, strict control of size and shape is necessary.

In recent work, Hussain *et al.* [19] reported the controlled sizes of AuNPs by using a polarity solvent which is ethanol. They found that high polarity solvent produced smaller and spherical nanoparticles, whereas low polarity solvent produced bigger sizes with different shapes. The seeded-growth method is mostly used and results in the improvement of size distribution and highly monodispersed particles. Three parameters play a huge role in the synthesis of Au nanostructures: pH, concentration of reducing agent, and temperature [20]. Another important parameter is the colour of the solution, which is a wavelength/frequency parameter necessary to understand the optical properties. Au nanostructures usually appear with a complementary colour, like red/ purple/ pink which represents the state of the solution without any gold ions in the solution [16]. This is due to the collective oscillations constrained by the reduced dimensions of the nanostructures in which the electrons are confined, leading to absorption inthe visible region [16, 21]. A study by Karakocak *et al*. [22] reported synthesized AuNPs using sodium citrate as the reducing agents. After stirring for 20 - 30 mins the solution became wine-red, showing the reduction of Au ions. The end product was AuNPs with a size range of 10 – 50 nm.

The differences in the colour of the solution of the MNSs arise as a result of the change in size distribution, surrounding the medium, shape, and high absorption [23]. The colour of the solution is dependent on the size of MNSs and is related to the absorption wavelength. A study by Wrigglesworth *et al.* [24] reported that five AuNPs of different sizes (samples A to E) were synthesized using the seed-meditated method. The transmission electron microscopy (TEM) results have shown an increase in particle size by giving average diameters of 32, 53, 81, 94, 127 nm for samples A, B, C, D, and E, respectively. The colour of the sample solutions changed from pink, dark pink, purple, violet to blue, from sample A to E, respectively. In the same way, the absorption spectrum peak had red-shifted (from 528 nm to 612 nm) and broadened significantly, as the particle size increased from sample A to E. Different sizes cause the difference in the solution colours of Au nanostructures as shown in Figure 2. *1* [25]. As the size of Au nanostructures increases, the colour changes. Nanostructures with a diameter range of 1 – 50 nm are classified as small NPs and a diameter range of 50 – 100 nm are large NPs.

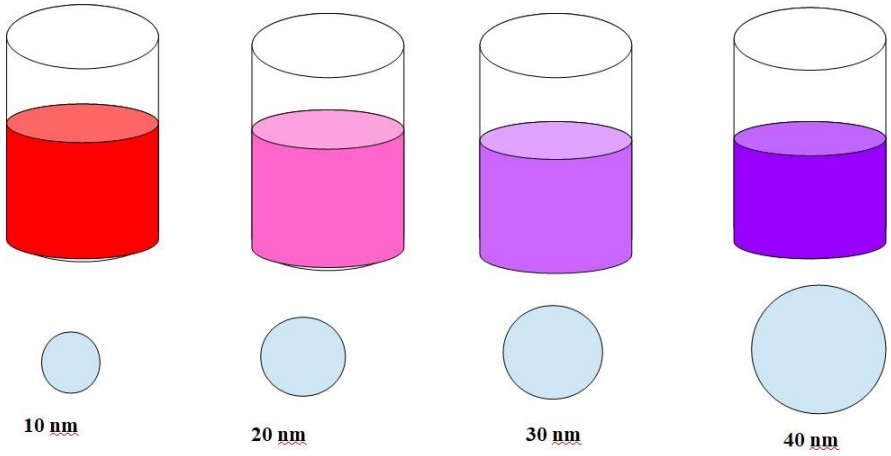

Figure 2. 1. Schematic diagram of AuNPs solutions of various sizes.

The optical properties of MNSs are sensitive to their size, shape, and surrounding medium [26]. When small AuNPs are exposed to light the oscillating electric field causes the conduction electrons to oscillate in a well-organized manner. This happens due to the displacement of the electron cloud; a restoring force arises from coulomb attraction between electrons and nuclei which results in the oscillation of the electron cloud [16]. The shape and size of AuNPs result in plasmonic resonance bands from the visible to the infrared region [27].

Different researchers have reported different sizes of AuNPs. For example, Piella *et al*. results showed that the localized surface plasmon resonance (LSPR) band narrows with the peak position from 505 to 517 nm as the NPs size increases from 3.6 nm to 11.3 nm and redshift was observed. Neither the appearance of new peaks at longer wavelengths nor the broadening of the band was observed, which indicates the absence of any aggregation on the AuNPs. Two regions of different behaviour were recognized. The absorption band, for small AuNPs (< 8 nm), slight variations in the size (from 3.6 to 8 nm) were interpreted into large shifts in the LSPR peak position from 505 to 515 nm. Similarly, for large AuNPs (> 8 nm), the size-dependence was smoother and the size variations from 8 to 13 nm, hence the smaller standard redshift was observed from 515 to 517 nm [20].

Said *et al*., reported a study where AuNPs were synthesized using the thermochemical method. They reported AuNP, mostly dominated by spherical shapes and sizes in the range of 12 - 23 nm. Their measurement of the UV-VIS spectra showed that the surface plasmon resonance shifted to a higher wavelength as the particle size decreased [28]. Zhuang *et al.*, on the other hand, reported AuNPs synthesized using the seeding growth methods, which can achieve a uniform size distribution. Gold nanospheres (AuNSs) showed uniform sizes of 5 ± 1, 10 ± 2, and 20 ± 1 nm. The bigger the size of AuNSs, the higher the shift of the surface plasmon absorption peaks to a higher wavelength, and a redshift was observed. The surface plasmon absorption peaks were observed between 520 – 530 nm. They observed the gold nanorods (AuNRs) with a diameter of 15 nm and a longitudinal ratio of 3 ± 0. 5 [29].

2.2.2 Shape of gold nanostructures

Gold nanostructures with different shapes and dimensions such as 1-D (wires and rods), 2-D (stars and triangles) and 3-D (cubes and spheres) have various optical and electrical properties which are of special interest [30]. Figure 2. *2* shows nanostructures of different shapes. Different shapes and sizes of AuNSs have been shown to create a large localized electromagnetic field enhancement. The study of AuNSs of various sizes revealed that branched nanoparticles have a strong surface-enhanced Raman scattering (SERs) activity compared to the non-branched ones [31]. Nanoparticles can be synthesized into shapes such as rods, wires, prisms, spheres, and cubes [32].

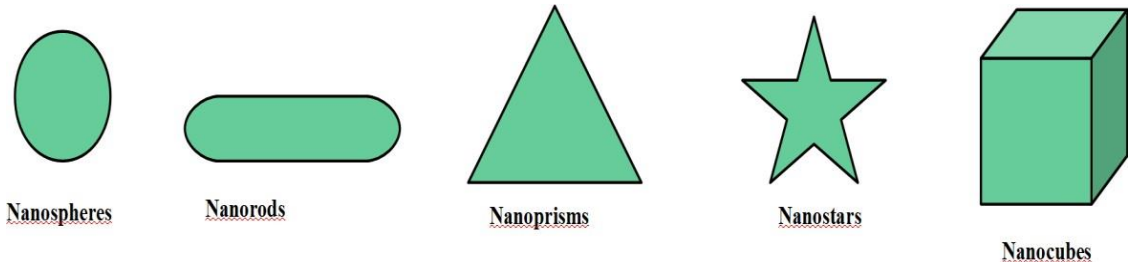

Figure 2. 2. Schematic diagram of nanostructures of different shapes.

Gold nanospheres (AuNSs) are simple to synthesize, scalable, uniform and high-yielding structures that provide access to materials with improved plasmonic properties [33]. Studies show that spheres compared to anisotropic nanoparticles have more intense electric fields localized near the sharp geometry features and the localized surface plasmon resonance (LSPR) wavelength tuneable over a broader range [34, 35]. Gold nanoshells have been shown to provide an SERs enhancement compared to AuNSs [31]. Small spherical seed particles, often less than 5 nm are usually referred to as gold seeds [36]. For example, Cramer *et al.* reported the synthesis of AuNSs and Au seeds by using the seed-mediated method. The Au seed had an average size of 4 nm and AuNSs had average sizes between 5 - 8 nm. Surface plasmon absorption peaks of the seeds were lower (517 nm) compared to that of AuNSs (522 nm), hence red-shift was observed [36]. Sun *et al.* has reported AuNSs with an average diameter of 5.2 ± 0.6 nm and exhibit a plasmon resonance peak at 520 nm [37]. AuNSs and Au seeds can be transformed into other shapes such as nanorods, prisms, and cubes.

The production of non-spherical AuNPs is a complex process and requires multistep synthesis. Different researchers reported the gold nanocubes (AuNCs) and their special properties. AuNCs have interesting plasmon coupling properties [38], photoluminescence [39], and catalytic properties [40], although, difficult to produce due to their six closed-packed 100-planes. A study by Thiele *et al.* [41] reported the synthesis of AuNCs by highly controlled production steps: the synthesis step, seed particle formed, followed by two independent growing steps. Their AuNCs had average edge lengths of 54, 62, 68, and 79 nm, and plasmonic resonance peaks of 558, 566, 584, and 608 nm were observed, respectively. In another work, Miranda *et al.* reported AuNCs with an average edge length of 13 ± 2 nm, synthesized by photocatalytic reduction methods in aqueous solutions. Their shape selectivity was found to be >90% and were reproduceable [40].

Gold nanorods (AuNRs) are easily tunable from visible (vis) to near-infrared (NIR) due to the shape-dependent longitudinal surface plasmon resonance [42, 43]. Their length divided by the width and is known as the aspect ratio, influenced by the location of longitudinal surface plasmon resonance in the spectrum. In addition, AuNRs of smaller sizes have a larger absorption cross-section and improve photothermal conversion due to higher absorption and larger sizes with larger scattering cross-sections and improved scattering-based applications such as imaging [12]. They have high stability, compatibility, easy production, and the special optical phenomenon derived from heterogeneous geometry [44]. The AuNRs have a unique property. It shows two plasma resonance bands because of the high aspect ratio, giving the nanostructures independent electronic collective vibrations. One direction where the free electrons move along the nanorod length is called longitudinal surface plasmon resonance absorption and the other direction is when the free electrons move along the nanorod width called transverse surface plasmon resonance [45].

Different researchers have reported AuNRs and their unique surface plasmon properties. For example, Meng *et al.* reported the synthesis of AuNRs using the seed growth method. Their diameters and lengths were controlled by adjusting silver ion (Ag^+) concentration in the growth solution. AuNRs had length sizes range of 15 - 45 nm and a length-diameter aspect ratio of 4.34. The XRD spectra showed peaks at 38.3, 44.4, 64.6, 77.5, and 82.3 which correspond to 111, 200, 220, 331, and 222 planes of Au according to JCPDS card #04-0784. UV-Vis spectra showed surface plasmon absorption peaks at 530 (TSPR peak) and 620 nm (LSPR peak) [45]. In another study, Huei *et al.* reported mini AuNRs with tunable longitudinal surface plasmon resonance from ~600 to >1300 nm. A seed-mediated growth method was used, and two weak reducing agents were used to tune the aspect ratios of the mini AuNRs from 2.2 to 10.5. The mini AuNRs had a length size range of 19.3 - 21.7 nm and a width size range of 9.0 - 5.8 nm. UV-Vis spectra showed the maximal longitudinal plasmon band wavelengths at 607, 673, 741 and 793 nm [12].

Triangular gold nanoprisms (AuNPrisms) are of high interest due to their sharp corners or tips, which show unique LSPR and high local electric fields when illuminated with light. This makes nanoprisms to be attractive candidates for applications such as SERs [46]. AuNPrisms shows two prominent modes: in-plane and out-of-plane modes. By controlling geometric parameters such as diameter and length, these modes can be fine-tuned. For the production of high-quality Au nanoprisms, iodide (I^-) anions are important [37]. A study by Mojie *et al.*

[37] reported the role of halide ions in the seed-mediated synthesis of AuNPrisms. The iodide concentration of ~30 μM produced sharp tips and high yield. High iodide concentration >80 μM produced AuNPrisms with blunt tips and low yield. Hence, the iodide concentration must be kept low to obtain high-quality triangular nanoprisms with high yield and sharp tips. In another study, Cramer *et al.* reported the synthesis of Au nanoprisms where they used potassium iodide as the reducing agent. Au nanoprisms with an edge length of 150 nm and the surface plasmon resonance peak of 536 nm were observed [36].

2.3 Fundamentals of surface plasmon in gold nanostructures

Surface plasmon (SP) is defined as an interaction between matter and the electromagnetic field of light and it is one of the AuNSs optical properties. The physical meaning of SP can be described as a metallic NP with a lattice of ionic cores that consists of conduction electrons moving freely inside the NP. When light is shining on an NP, a force is exerted on the conduction electrons by the electromagnetic field of light moving them and the surface. An electric dipole is created due to electrons that are restricted inside the NP. Positive charges accumulate on one side and negative charges on the opposite side. Therefore, an electric field is generated by this dipole inside the NP opposite that of the light and it will force the electrons to return to equilibrium position [14].

A force is exerted by the electric field on the conduction electrons of the metal NP causing them to collectively move to the NP surface. The conduction of electrons and the metal lattice leads to restoring force due to the Coulomb force between them. These two forces will cause the electrons to oscillate collectively with a maximal amplitude at LSPR frequency as known as plasmonic frequency [47]. Plasmonics is defined as the coupling of light to charges in metals, where the electric field of light sets free metal charges. The free electrons oscillate and allow strong field enhancement at the metal surface and interfaces of metals. The use of plasmonics makes it possible to create light with sub-diffraction limit wavelengths at optical frequencies [48]. Surface plasmons are free electrons oscillations caused by the optical methods at the metal surfaces. They can either be localized or propagated surface plasmons for metal nanoparticles [49, 50].

2.3.1 Localized surface plasmons (LSPRs) and surface plasmon polaritons (SPPs)

Surface plasmon resonance (SPR) refers to the collective electromagnetic oscillations of electrons between the metal and dielectric medium. These electronic oscillations can be propagated along a flat interface known as surface plasmon polaritons (SPPs) or restricted to the subwavelength structure known as localized surface plasmon resonance (LSPR) [51]. Figure 2. *3* shows SPP and LSPR modes. The unique plasmonic properties of AuNSs arise when interacting with light, where an oscillation of conduction band electrons occurs at a specific frequency, called LSPR [52]. SPPs are localized light waves that propagates along the surface of the planar metal and penetrates to different extents into the NP and dielectric medium [48].

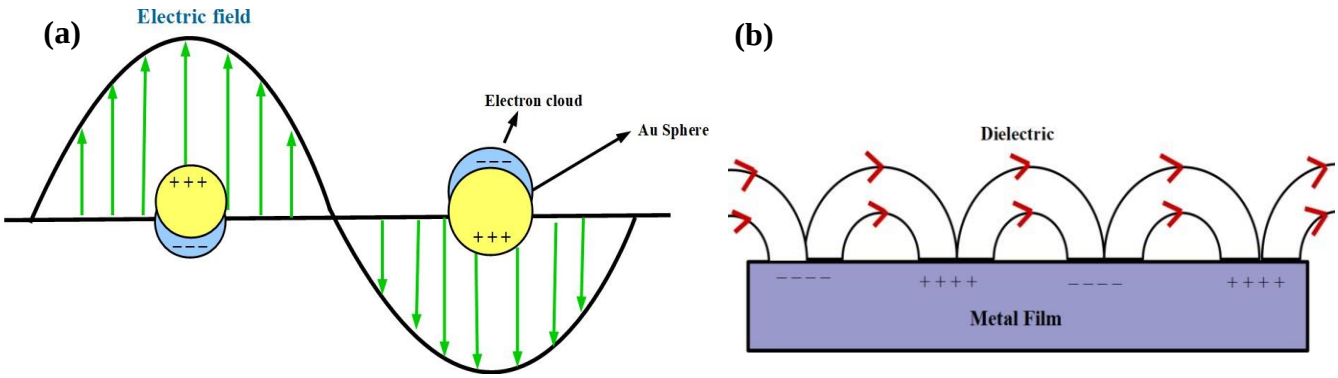

Figure 2. 3. Schematic diagram of (a) Localized surface plasmon resonance (LSPR). (b) Surface plasmon polariton (SPP).

The NP shape strongly affects the SP resonance. The restoring force for the SP is proportional to the charge accumulation and it is influenced by the NP geometry [14]. Figure 2. *4* shows the illustrations of charge accumulations for nanospheres and nanorods. For example, in nanorods at the NP surface, the charge accumulation will be different for electrons oscillating along the rod axis (longitudinal plasmons) and along the perpendicular direction (transversal plasmon). The electrons oscillating in the longitudinal plasmons have small forces and small frequencies, hence larger resonant wavelength, and higher aspect ratio [53]. The transversal plasmons fall at the same position as spherical NPs, hence the resonant wavelength is smaller. Other NP geometries such as nanocubes and triangular prisms give more complicated effects [54].

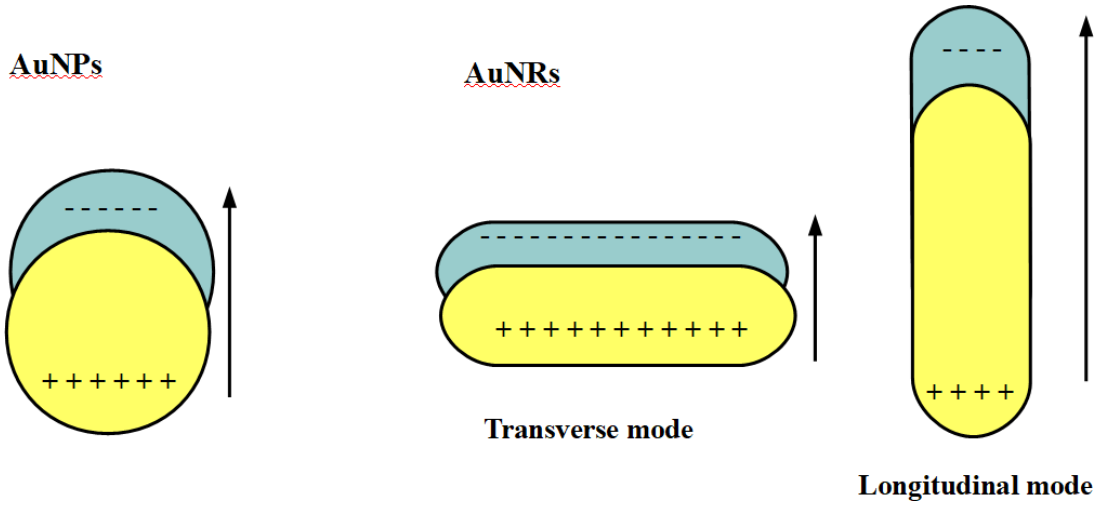

Figure 2. 4. Illustrations of charge accumulations for nanospheres and nanorods.

2.4 Organic solar cells application

Since the first demonstration of a practical photovoltaic cell in the mid-1950s, solar energy has become well known practical alternative energy technology. Traditionally, solar cells were manufactured using crystalline semiconductors, particularly silicon. Recently, the development of organic photovoltaic devices (OPVs) has attracted interest due to their lightweight, low cost, ease of manufacturing, and mechanical flexibility [55]. Solar cells have been known to be one of the important energy conversion devices that convert solar energy directly to electricity. This is done using semiconductor materials with photovoltaic properties [56]. The operation of a solar cell requires three basic characteristics such as the absorption of light-generating electron-hole pairs, separation of charge carriers (electron-hole pairs) of opposite charges, and the separation extraction of the carriers to an external circuit. Figure 2. *5* shows that solar cells are designed using p-type and n-type material to form p-n junctions. Si solar cells have been extensively used to collect solar energy as p-n junction type solar cells. Fabrication and distribution of solar energy through solar cells is a well-established technology, which could be used to supply electricity to non-grid users.

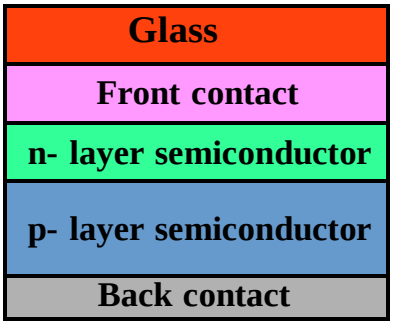

Figure 2. 5. Basic solar cell

However, the cheaper conventional electricity from fossil fuel and nuclear power stations compared to electricity from solar cells [57], has established infrastructure, but cannot reach the communities that are off-grid. Furthermore, high manufacturing costs for conventional solar cells based on inorganic materials require expensive vacuum system and high-temperature processes for production. Hence, organic materials were introduced as light absorption materials to overcome the issue of cost in conventional solar cells. Organic materials processes make use of low temperature and are vacuum-free systems, making them cheap to manufacture [58].

2.4.1 Device architecture

Organic solar cells (OSCs) are a type of optical device that uses organic electronics that deal with conductive organic polymers and are suitable for solar energy harvesting due to their properties [28]. These solar cells utilize light-absorbing polymers to generate an electrical current from sunlight by photovoltaic effects. The advantages of OSCs are lightweight, low cost, low-temperature fabrication process, semi-transparent, and mechanical flexibility [59]. OSCs have the potential to advance applications such as building-integrated photovoltaics (BIPV), PV charges for portable electronics, and large volume flexible solar modules in buildings and can easily be applied to windows, doors, and geysers [60].

OSCs consist of three major parts depending on their function. Firstly, the active layer (AL) is a blend of organic semiconductors and fullerene derivatives. These organic semiconductors can generate excitons and separate charge carriers at the interface of the two components. Electrons flow from electron donors (organic semiconductors) to electron acceptors (fullerene derivatives), due to the energy level alignment of the blend [61]. Secondly, the charge transport layer for electrons and holes; electron transport layer (ETL) and hole transport layer

(HTL). These two layers selectively accept one charge carrier type (electrons or holes) from the active layer and enable charge extraction to the electrode [62]. Thirdly, electrodes that finally collect charge carriers. Electrons are transferred to the cathode and holes are accumulated at the anode. Aluminum (Al), silver (Ag), gold (Au), and indium tin oxide (ITO)have been used as transparent conducting electrodes (TCE) or metal electrodes [63]. Figure 2. *6* demonstrates OSC device architecture. The arrangement of the OSC device is important. When the device is assembled in the order of TCE which is (bottom electrode)/ HTL/ active layer/ETL/metal electrode (top electrode), it is referred to as a conventional organic solar cell. When the device is fabricated in the order of TCE/ETL/active layer/HTL/ metal electrode, it is referred to as an inverted organic solar cell [64].

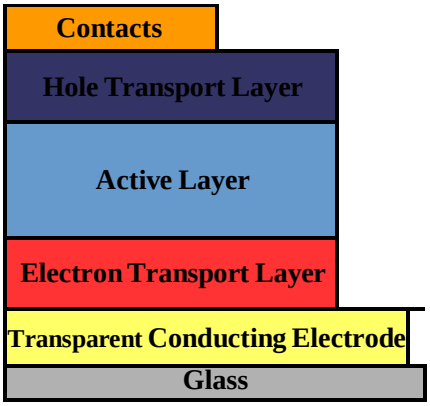

Figure 2. 6. Schematic diagram of OSC device.

There are two types of organic solar materials, conjugated polymers, and low molecular weight organic semiconductors. The difference between these two is how they are fabricated. The conjugated polymers are fabricated using methods such as spray pyrolysis, spin coating, and screen printing [65]. Low molecular weight organic semiconductors are deposited using gas-phase methods such as vapor deposition and sublimation which needs a vacuum environment [66]. There are different types of conjugated polymers, such as Poly[N-9'-heptadecanyl-2,7-carbazole-alt-5,5-(4',7'-di-2-thienyl-2',1',3'-benzothiadiazole)] (PCDTBT) , [6,6]-Phenyl-C61-butyric acid methyl ester (PCBM) and Poly (3,4- ethylene dioxythiophene): polystyrene sulfonate (PEDOT: PSS) [67].Figure 2. *7*, shows how these materials can be used in OSCs.

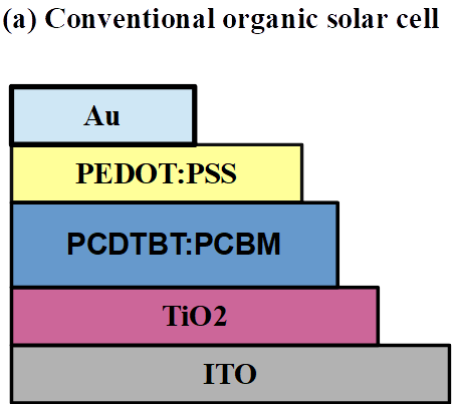

Figure 2. 7. Schematic diagram of a conventional organic solar cell.

The active layer material in the OSC must have good morphology, structural, electrical, and optical properties. Organic polymer like PCDTBT has been used as a promising material for electron donor layer in OSCs. PCDTBT has a shallow bandgap and deeper highest occupied molecular (HOMO) level. By using these advantages this electron donor material increases light absorption area and consequently, the open circuit voltage. The extended red absorption of the PCDTBT leads to the improvement of the performance of the OSC due to the harvesting of a great fraction of the sun's radiation [68]. In addition, a fullerene material, PCBM is used as an electron acceptor material due to their superior electron-transporting property [68]. It is reported to improve the efficiencies of BHJ OSCs because the optical density of $PC_{71}BM$ in the visible region is higher compared to $PC_{60}BM$, and also the improvement in the absorption spectra of the polymer [69]. A study by Heeger and Bazan *et al.* reported the efficiency improvement of $PC_{71}BM$ blend from 5.5 to 7% by controlling the morphology. Hence, it showed improved optical density and mobility compared to $PC_{60}BM$ [70].

Interfacial materials are important in OSCs and are placed between the active layer and transparent conducting oxide. The right HTL and ETL should have the accepted chemical stability making them electrically suitable for conduction [71]. In this case, PEDOT: PSS is the hole transport layer in the OSC. The high transparency of PEDOT: PSS makes it an attractive material to improve the photocurrent of the OSC due to its absorption in the visible range, long-term stability, easy processing OSCs [72]. It is usually a front electrode in organic solar cells because of its high conductivity, transparency, and work function of 5.1 eV which makes it suitable as an anode [73]. In the same way, titanium dioxide (TiO_2) is commonly used as an electron-hole transport layer due to its non-toxicity, low cost, high

electron mobility, chemical stability, and high transparency in the visible range [74]. It is an n-type semiconductor that has been used extensively in OSC [75], lithium-ion batteries [76], and polymer solar cells [77].

2.4.2 Solar cell characteristics

When sunlight reaches the surface of the earth and strikes OSCs, some of the light will be absorbed, scattered, and reflected by materials and electrodes used. The sunlight optical length normalized to the thickness of the earth's atmosphere defines the air mass (AM). It is mostly used to characterize the intensity of solar radiation and account for the absorption and scattering of wavelengths by different atmospheric species [78]. AM value is given by

$$AM = \frac{1}{cos\,\theta} \qquad 2.\ 1$$

where θ is the angle of incident when the sun is directly overhead [79]. The AM 1.5 with θ = 48.2℃ has an intensity of 1000 W/m^2 and used to characterize photovoltaics as standard spectrum [80]. The solar energy intensity is 1353 W/m^2 outside the earth's atmosphere and the spectral distribution is air mass zero (AM 0) radiation spectrum [81]. The spectra of AM 0, blackbody, and AM 1.5 are shown in Figure 2. *8*.

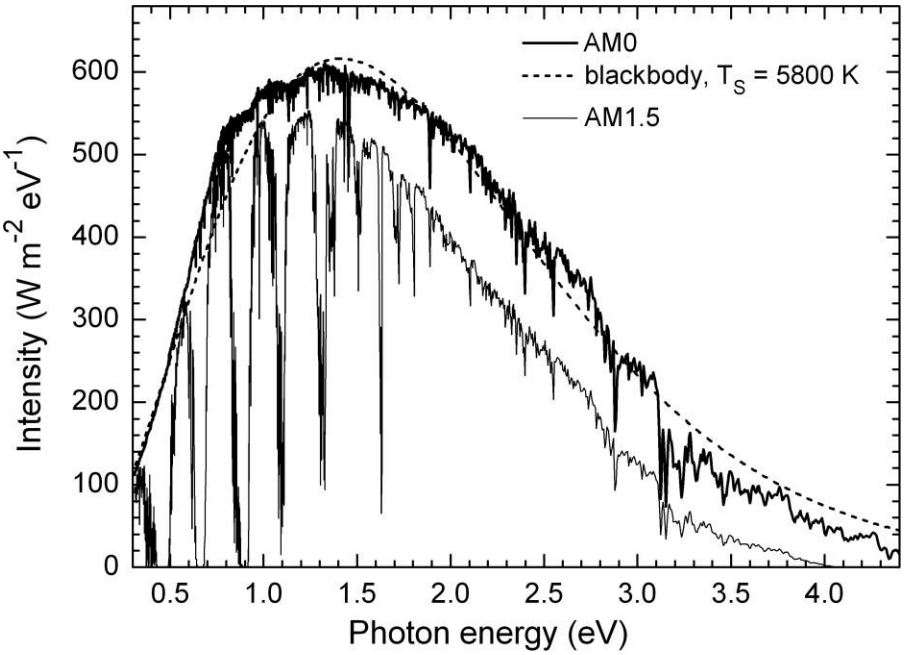

Figure 2. 8. Solar spectra: AM 0, AM 1.5 (θ = 48.2℃) and blackbody with a temperature 5800 K [80].

Under the standard conditions of AM 1.5 G and 1000 W/m^2, the performance of a solar cell can be studied by measuring the current-voltage (J-V) curve in the dark and under illumination. Usually, solar cells behave like diodes in the dark and in illumination, the magnitude of short circuit current (Jsc) shifts the curve down when generating a photocurrent. To obtain the J-V curve, current density (J) is measured with respect to voltage (V) and this studies the photovoltaic characteristics. The parameters of a solar cell that can be measured are short circuit current density (Jsc), open-circuit voltage (Voc), fill factor (FF), and power conversion efficiency (PCE) [82]. Figure 2. *9* shows an example of the J-V curve and these parameters.

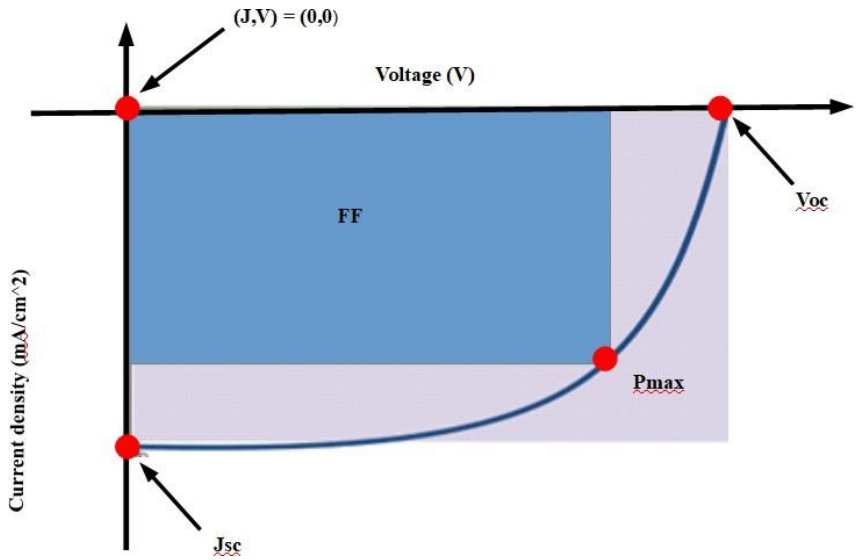

Figure 2. 9. J-V characteristics of a solar cell under illumination [82].

Short circuit current (Jsc) is the maximum current that flows through the external circuit when there is no applied voltage (V = 0). It is the current value obtained per unit area at zero voltage. Due to the charge carries generated, the flow of current contributes to the efficiency of the solar cell. Jsc is related to charge mobility, photon absorption, and charge separation [83]. These properties have a significant effect on the device. For example, charge mobility depends on the intrinsic properties of the solar cell. Photon absorption is dependent on the bandgap of the active layer. According to theoretical results, the ideal bandgap is around 1.3 eV to obtain the highest photon absorption efficiency [84]. For charge separation, it depends on the LUMO levels of the donor, acceptor, and morphology of the active layer [83].

Similarly, open-circuit voltage (Voc) is the voltage value measured at the zero current of the circuit. In other words, at the point where there is no flow of current in the device, voltage is obtained. It is directly associated with the energy bandgap of the acceptor and donor materials. Voc is determined by the difference in the work functions of two metal electrodes [85]. A study by Frohne et al. reported that the doping levels of PEDOT: PSS using electrochemical potential, the Voc is affected [86]. Furthermore, by using electrodes with high differences in work function, Voc can be increased. It is also influenced by other parameters in OSCs such as chemical potential gradient and dark current [87]. The product of Voc and Jsc gives the fill factor (FF) of the device. This is defined as the ratio of maximum power generated by the solar cell. It measures the maximum square area of the J-V curve, and the magnitude of the square shows a higher power output, which shows the quality of the device. In the same way, the FF is influenced by the balance between the hole and electron mobility, and it is dependent on the recombination transport, and resistance of charges [80].

The quality of the thin films and interfaces are determined by series and shunt resistance. Series resistance (Rs) and shunt resistance (Rsh) have a significant effect on the FF through the changes of Jsc and Voc. Series resistance (Rs) is a resistance that accumulates ohmic losses and contributions from electrodes and bulk resistivity of materials, respectively. For a large magnitude of current to flow in the positive biased direction, Rs must be very small [88]. In principle, Rs is sensitive to the thickness, morphology, and intrinsic resistance of the semiconductor blend layer and the quality of the electrode's interfaces [87]. Shunt resistance (Rsh) is the resistance that occurs due to the recombination of charge carriers in the donor or acceptor interfaces and electrodes which results from leakage current. It must be large enough to produce the photogenerated current through the diode and junction of the solar cells to maximize the voltage [89]. Rsh is influenced by the defects and impurities in the active layer and related to the charge recombination [87]. In OSCs, Rsh (>1000 Ω) is usually far larger than Rs (10 ~ 100 Ω) [89]. All these parameters are highly dependent on each other; low Rsh decreases Voc and high Rs decreases the Jsc, while both influence the decrease of FF [87].

2.4.3 OSCs working principle

Organic materials consist of the highest occupied molecular orbital (HOMO) and the lowest occupied molecular orbital (LUMO) [66], similar to valence and conduction band in inorganic semiconductors. Blended organic devices consist of donor and acceptor polymers. The HOMO and LUMO of the donor have the highest energy levels compared to that of the

acceptor polymer, leading to the electron transfer from donor to acceptor. In organic solar cells, electrons are transferred in orbitals [82]. Figure 2. *10* demonstrates the working mechanism of an OSC device. The energy difference between HOMO and LUMO gives the energy bandgap of the organic solar cell. The bandgap is the minimum photon energy required for the excitation of electrons from HOMO to LUMO [82].

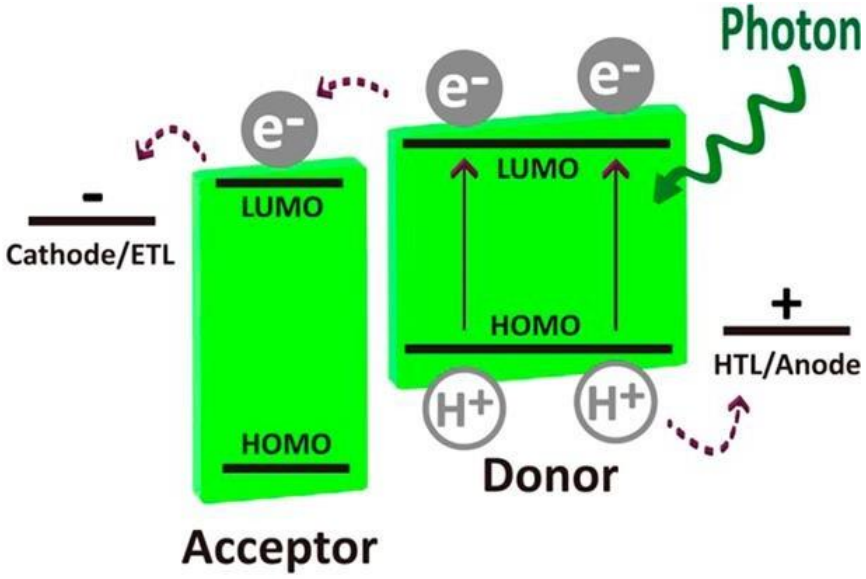

Figure 2. 10. Working mechanisms of an OSC device [82].

Polymer materials that consist of a donor and acceptor blended with nanostructured morphology are called bulk heterojunction (BHJ) material. The advantage of the mixture of donor and acceptor material in BHJ solar cells is one of the best solutions in terms of performance, because it has a large volume of interaction between the acceptor and the donor, resulting in more separate paths for the transport of free carriers and efficient charge separation [25]. The exciton separation at the interface between the donor and acceptor material and the creation of an electron-hole pairs, generate photocurrent from the incident light [90].

Three factors that limit the efficiency of an OSCs are: black body radiation, recombination losses, and spectrum losses [91]. Any material not being able to emit electromagnetic radiation is referred to as blackbody. OSCs work by absorbing photons and creating an electron-hole pair. This process contributes to current. Unfortunately, there is a chance that electrons and holes coming in contact may lead to recombination. This will emit a photon and

cause a decrease in the efficiency of the solar cell, and it is referred to as recombination losses. Spectral losses occur due to two factors: firstly, when the wavelengths are longer than the bandgap energy of the semiconductor, photons cannot be absorbed and do not contribute to the generation of the photocurrent. Secondly, the energy above and beyond the bandgap energy is lost because excited electrons in the conduction band will fall back to the band edge [91].

The commercial applications of OSCs are challenged by the low power conversion efficiency (PCE). Issues with OSCs are due to the low charge mobility and short exciton diffusion length [92], hence, restricting the intensity of the absorbed light and the thickness active layer. The PCE of OSCs is dependent on the thickness of the active layer. Research work has been done to improve efficiency by increasing the thickness of the absorber layer. However, the increase in thickness decreases the charge collection efficiency and conductivity of the device. Therefore, it is important to maintain the thin active layer and carrier mobility generated. Another alternative method is the use of MNSs with SPR properties. Plasmonic MNSs have been widely used in OSCs to enhance performance [93].

2.5 Plasmonic solar cells

One of the promising approaches is the use of MNSs with a plasmonic effect that scatter and absorb light but also confine light within their surrounding surfaces resulting in enhanced light absorption [94]. Various plasmonic MNSs have been incorporated to improve the performance of organic solar devices. Nanostructures such as nanoparticles [93], nanospheres [95], nanowires [96], nanorods [97], and nanostars [97] have been incorporated into different layers of OSCs. When the nanostructures are introduced to OSCs, it is referred to as plasmonic solar cells [93]. The use of MNSs has become an interesting solution to increase the efficiency of OSCs and does not affect the design of the device because it can easily be added to one of the layers [25]. There are different plasmonic enhancement strategies and design of OSCs with MNSs.

2.5.1 Plasmonic enhancement strategies

Light absorption can be enhanced by two mechanisms: a near-field enhancement and increasing of the forward scattering cross-section [98]. These mechanisms are dependent on the shape, size, and surrounding medium of the MNSs, as well as how they are incorporated

in solar cell devices. These are factors determine the optical resonances in coupled plasmonic particles [99]. The plasmonic enhancement in OSCs is achieved via the interaction between MNSs and the active layer. The use of different mechanisms such as far-field scattering, and near-field enhancement also help to achieve plasmonic enhancement in OSCs [64].

MNSs incorporated in OSCs layers scatter light in both forward and reverse directions [25]. When light is illuminated in small spherical NPs it results in more scattering in the forward direction, while large spherical NPs scatter more light in the reverse direction. This is known as the far-field scattering and it is referred to as light trapping [64]. Light trapping is caused by the scattering effect, and it can be achieved using large NPs of 100 nm or more. Parameters such as shape, size, and surrounding medium also contribute to the increased scattering effect in OSCs [98].

Light will scatter more into the devices with larger permittivity if the MNSs are placed close to the metal contacts. The metal contact reflects light to the surface, where MNSs are incorporated. These results increased light scattering in the OSCs as shown in Figure 2. *11*(a). Another way to make use of resonant plasmon excitation in OSCs is the use of local-field enhancement around the MNSs, which can increase light absorption in the surrounding area as shown in Figure 2. *11*(b) [25]. An electromagnetic field that has more energy than the incident photon energy and confined at the surface of plasmonic structures is referred to as the near- fear enhancement. It can increase light absorption and exciton generation, which improves the photon-to-electron conversion efficiency [64].

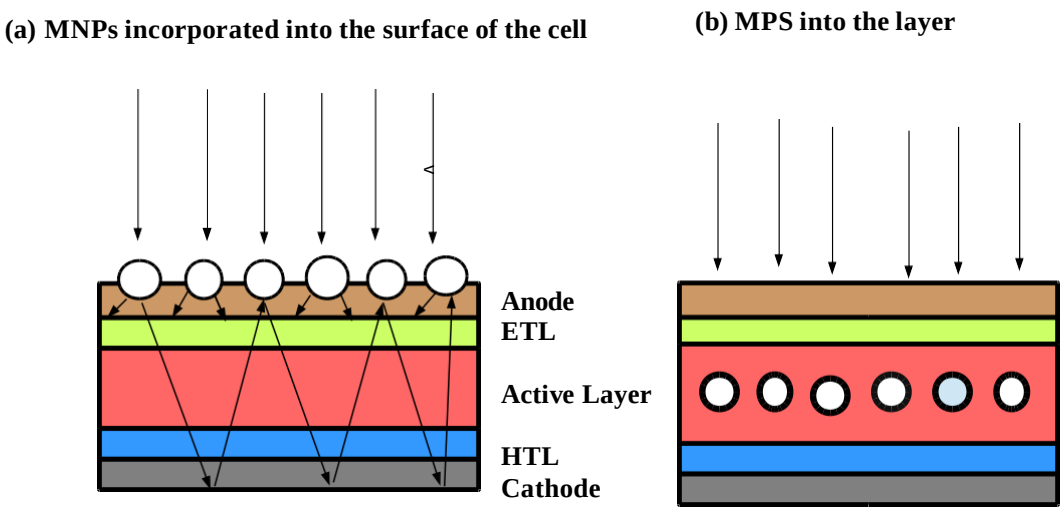

Figure 2. 11. (a) Light scattering from MNPs at the surface of OSCs. (b) Excitation of MNPs added in the OSCs active layer [25].

There are various designs of plasmonic solar cells. Figure 2. *12* shows different configurations on solar cells. Plasmonic nanostructures can be used in three different configurations: on the surface of the cell, embedded into the active layer, and at the bottom interface between the semiconductor and the metal in the form of scattering nanoparticles [100]. When MNPs are on the top surface of the solar cell, light is scattered and trapped by the semiconductor thin film due to high angle scattering, which causes an increase of the effective optical path length inside the cell. When the MNPs are embedded into the semiconductor active layer, the strong localization and enhancement of the near field in the proximity of the particles causes the creation of additional electron-hole pairs within the semiconductor. When the MNPs are at the bottom interface, a metal grating at the back surface consisting of a periodic array of nanostructures can couple light to surface plasmon polaritons (SPP), which propagate in the plane of the semiconductor [101]. It is beneficial to place MNSs on the rear side of the solar cell, because at the front of the cell they could give rise to destructive interference and would reflect and absorb a significant amount of incident light before it reaches the active layer [102].

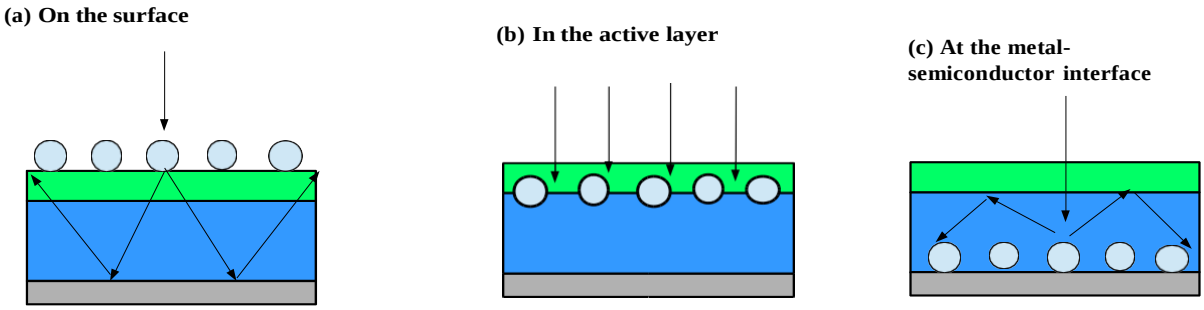

Figure 2. 12. Plasmonic light-trapping configuration for solar cells. (a) MNPs on the top surface of the solar cell. (b) MNPs embedded in the active layer. (c)MNPs at the metal/semiconductor interface.

2.5.2 Gold nanostructures in OSCs

There have been several studies about the addition of Au nanostructures to improve the efficiency of OSCs. Studies have reported the improvement of PCE by embedding MNPs in a hole transport layer such as PEDOT: PSS which is widely used in solar cells [103, 104]. The addition of AuNPs into PEDOT: PSS has been found to increase the photocurrent by SPR as observed in various blend solar cells [105]. For example, Said *et al.* [28] reported that the incorporation of AuNPs with different sizes into PEDOT: PSS enhanced the efficiency from

0.78% to 1.02%. The strong coupling characteristic nature and high stability of AuNPs have attracted the solar cell industry to enhance the performance of the device [104]. Shin *et al.* reported that embedding large size AuNPs (>70 nm) into PEDOT: PSS resulted in far-field scattering enhancement, thus the PCE increased from 5.35% to 8.585% [104]. Furthermore, Stavytska-Barba *et al.* [103] showed that morphological and chemical changes caused by the MNPs in PEDOT: PSS layer can contribute to the performance of the OPV cells. In addition, Jheng *et al.* used decahedral AuNPs of various sizes into the hole transport layer. The edges sizes of AuNPs significantly influenced the device performance and improved the PCE from 3.76% to 4.22%. Furthermore, shapes were found to have a huge effect on the efficiency of the device [106]. In another work, Wu *et al.* [107] reported Au nanospheres blended into the anode buffer layer (PEDOT: PSS) to trigger LSPR, which enhanced the PCE to 4.24% from 3.57% without dramatically affecting the electrical properties of the device. Meanwhile, Fung *et al.* [108] showed that from their nanoparticles in PEDOT: PSS the optical enhancement was small due to the strong near-field LSPR. In addition, when the PCE measurements originated from the interfacial area between hole transport layer and active layer, the shut resistance is reduced.

Optical enhancement effects from plasmonic MNPs in an active layer have been widely studied [105]. For example, He *et al.* reported the improvement of the PCE of an inverted OSC by the incorporation of Au nanorods into the active layer PCDTBT: PCBM. When the Au nanorods were incorporated the OSC device showed an enhanced light absorption. This increased PCE by 6.83%, accounting for PCE of up to 18.9%. Hence, the plasmonic effect contributes greatly to the performance of the OSC [109]. In another work, Liu *et al.* [110] incorporated Au arrowhead nanorods (AHNRs) into the photoactive layer PCDTBT: PCBM of an inverted solar cell. There was a significant increase in the efficiency of the device by 28.7%, due to the strong plasmonic effect of nanorods. In addition, the use of AuNPs in PCDTBT: PCBM blend active layer has improved light absorption by scattering of large nanoparticles (>40 nm) of the incident light, which cause the optical path length to be significantly increased [105, 111]. These MNPs decreased series resistance in OSC by increasing charge transport in the photoactive layer [111]. Furthermore, MNPs with different shapes such as nanoplates and nanowires in the PCDTBT: PCBM layer shows absorption enhancement due to LSPR and scattering effect, which gives relatively 40% increased PCE [105].

Similar studies have been done by incorporating Ag nanostructures in the active layer. For example, Wang *et. al* [112] used two types of Ag nanostructures which are Ag nanoplates and AgNPs. These nanostructures were added into the active layer blend PCDTBT: $PC_{71}BM$ of an OSC device. Ag nanoplates showed an increase of the PCE from 5.9% to 6.6% compared to the AgNPs. In another work, Wang *et al.* reported the positive effects of Ag clusters in the PCDTBT: $PC_{70}BM$ active layer of an OSC device. The values of the devices such as open-circuit voltage (Voc), short-circuit density (Jsc) and fill factor (FF) were reported to have improved due to the addition of Ag clusters. Hence, light absorption was enhanced, and charge transport was increased, while resistance was decreased. Ag clusters (average size of 40 nm) increased the PCE of the device from 6.3% to 7.1% [111].

In some cases, the incorporation of MNSs between the interfaces will affect the PCE of the OSCs. Wu *et al.* have reported the addition of Ag nanotriangle (NT) arrays on the ITO substrate. The PCE was improved from 4.24% to 4.52% due to the increase in exciton generation caused by the strong local field and scattering generated by the LSPRs of the AgNTs [94]. However, MNPs between the nanoparticle and active layer contribute exciton recombination sites which reduces the performance of the device [113].

References

1. Pareek, V., et al., *Synthesis and applications of noble metal nanoparticles: a review.* Advanced Science, Engineering and Medicine, 2017. **9**(7): p. 527-544.
2. Kong, F.-Y., et al., *Unique roles of gold nanoparticles in drug delivery, targeting and imaging applications.* Molecules, 2017. **22**(9): p. 1445.
3. Abdelhalim, M.A.K., M.M. Mady, and M.M. Ghannam, *Physical properties of different gold nanoparticles: ultraviolet-visible and fluorescence measurements.* J Nanomed Nanotechol, 2012. **3**(3): p. 178-194.
4. Yong, K.-T., et al., *Synthesis and plasmonic properties of silver and gold nanoshells on polystyrene cores of different size and of gold–silver core–shell nanostructures.* Colloids and Surfaces A: Physicochemical and Engineering Aspects, 2006. **290**(1-3): p. 89-105.
5. Solati, E. and D. Dorranian, *Comparison between silver and gold nanoparticles prepared by pulsed laser ablation in distilled water.* Journal of Cluster Science, 2015. **26**(3): p. 727-742.
6. Camacho-Flores, B., et al., *Copper: synthesis techniques in nanoscale and powerful application as an antimicrobial agent.* Journal of Nanomaterials, 2015. **2015**.
7. Kim, H., et al., *Multifunctional photonic nanomaterials for diagnostic, therapeutic, and theranostic applications.* Advanced Materials, 2018. **30**(10): p. 1701460.
8. Rahme, K. and J.D. Holmes, *Gold nanoparticles: synthesis, characterization, and bioconjugation,* in *Dekker Encyclopedia of Nanoscience and Nanotechnology, Third Edition*. 2015, CRC Press, Taylor & Francis. p. 1-11.
9. Burrows, N.D., et al., *Surface chemistry of gold nanorods.* Langmuir, 2016. **32**(39): p. 9905-9921.
10. Li, N., P. Zhao, and D. Astruc, *Anisotropic gold nanoparticles: synthesis, properties, applications, and toxicity.* Angewandte Chemie International Edition, 2014. **53**(7): p. 1756-1789.
11. Dreaden, E.C., et al., *The golden age: gold nanoparticles for biomedicine.* Chemical Society Reviews, 2012. **41**(7): p. 2740-2779.
12. Chang, H.-H. and C.J. Murphy, *Mini gold nanorods with tunable plasmonic peaks beyond 1000 nm.* Chemistry of Materials, 2018. **30**(4): p. 1427-1435.
13. Huang, X., et al., *Gold nanoparticles: interesting optical properties and recent applications in cancer diagnostics and therapy.* 2007.
14. García, M.A., *Surface plasmons in metallic nanoparticles: fundamentals and applications.* Journal of Physics D: Applied Physics, 2011. **44**(28): p. 283001.
15. Daniel, M.-C. and D. Astruc, *Gold nanoparticles: assembly, supramolecular chemistry, quantum-size-related properties, and applications toward biology, catalysis, and nanotechnology.* Chemical reviews, 2004. **104**(1): p. 293-346.
16. De Souza, C.D., B.R. Nogueira, and M.E.C. Rostelato, *Review of the methodologies used in the synthesis gold nanoparticles by chemical reduction.* Journal of Alloys and Compounds, 2019.
17. Cao, P., et al., *Size-dependent optical and electrochemical properties of gold nanoparticles to L-cysteine.* Gold Bulletin, 2021: p. 1-7.
18. Pakravan, A., R. Salehi, and M. Mahkam, *Comparison study on the effect of gold nanoparticles shape in the forms of star, hallow, cage, rods, and Si-Au and Fe-Au core-shell on photothermal cancer treatment.* Photodiagnosis and Photodynamic Therapy, 2021. **33**: p. 102144.
19. Hussain, M.H., et al., *Synthesis of Various Size Gold Nanoparticles by Chemical Reduction Method with Different Solvent Polarity.* Nanoscale research letters, 2020. **15**(1): p. 1-10.

20. Piella, J., N.G. Bastús, and V. Puntes, *Size-Controlled Synthesis of Sub-10-nanometer Citrate-Stabilized Gold Nanoparticles and Related Optical Properties.* Chemistry of Materials, 2016. **28**(4): p. 1066-1075.
21. Pluchery, O., H. Remita, and D. Schaming, *Demonstrative experiments about gold nanoparticles and nanofilms: an introduction to nanoscience.* Gold Bulletin, 2013. **46**(4): p. 319-327.
22. Karakocak, B.B., et al., *Hyaluronate coating enhances the delivery and biocompatibility of gold nanoparticles.* Carbohydrate polymers, 2018. **186**: p. 243-251.
23. Khurana, K. and N. Jaggi, *Localized Surface Plasmonic Properties of Au and Ag Nanoparticles for Sensors: a Review.* Plasmonics, 2021: p. 1-19.
24. Wrigglesworth, E.G. and J.H. Johnston, *Mie theory and the dichroic effect for spherical gold nanoparticles: an experimental approach.* Nanoscale Advances, 2021. **3**(12): p. 3530-3536.
25. Notarianni, M., et al., *Plasmonic effect of gold nanoparticles in organic solar cells.* Solar Energy, 2014. **106**: p. 23-37.
26. Tan, H., et al., *Plasmonic light trapping in thin-film silicon solar cells with improved self-assembled silver nanoparticles.* Nano letters, 2012. **12**(8): p. 4070-4076.
27. Tao, A.R., S. Habas, and P. Yang, *Shape control of colloidal metal nanocrystals.* small, 2008. **4**(3): p. 310-325.
28. Said, D., et al., *A study of the influence of plasmonic resonance of gold nanoparticle doped PEDOT: PSS on the performance of organic solar cells based on CuPc/C60.* Heliyon, 2019. **5**(11): p. e02675.
29. Zhuang, Y., et al., *Size and Shape Effect of Gold Nanoparticles in "Far-Field" Surface Plasmon Resonance.* Particle & Particle Systems Characterization, 2019. **36**(1): p. 1800077.
30. Khan, A., et al., *Shape-dependent performance of gold nanocrystals supported on TiO2 for photoelectrochemical water oxidation under different radiations.* International Journal of Hydrogen Energy, 2019. **44**(41): p. 23054-23065.
31. Njoki, P.N., et al., *Size correlation of optical and spectroscopic properties for gold nanoparticles.* The Journal of Physical Chemistry C, 2007. **111**(40): p. 14664-14669.
32. Kim, F., et al., *Platonic gold nanocrystals.* Angewandte Chemie International Edition, 2004. **43**(28): p. 3673-3677.
33. Ashley, M.J., et al., *Shape and size control of substrate-grown gold nanoparticles for surface-enhanced raman spectroscopy detection of chemical analytes.* The Journal of Physical Chemistry C, 2018. **122**(4): p. 2307-2314.
34. Nikoobakht, B. and M.A. El-Sayed, *Preparation and growth mechanism of gold nanorods (NRs) using seed-mediated growth method.* Chemistry of Materials, 2003. **15**(10): p. 1957-1962.
35. O'Brien, M.N., et al., *Universal noble metal nanoparticle seeds realized through iterative reductive growth and oxidative dissolution reactions.* Journal of the American Chemical Society, 2014. **136**(21): p. 7603-7606.
36. Cramer, H.E., et al., *Shape-controlled gold nanoparticle synthesis*. 2013, ARMY RESEARCH LAB ABERDEEN PROVING GROUND MD WEAPONS AND MATERIALS RESEARCH ….
37. Sun, M., et al., *The effect of iodide on the synthesis of gold nanoprisms.* Journal of Experimental Nanoscience, 2015. **10**(17): p. 1309-1318.
38. Lee, Y.H., et al., *Nonlinear optical switching behavior of Au nanocubes and nano-octahedra investigated by femtosecond Z-scan measurements.* Applied Physics Letters, 2009. **95**(2): p. 023105.

39. Zhou, Y., et al., *A comparison study of detecting gold nanorods in living cells with confocal reflectance microscopy and two-photon fluorescence microscopy.* Journal of microscopy, 2010. **237**(2): p. 200-207.
40. Miranda, A., et al., *Synthesis of gold nanocubes in aqueous solution with remarkable shape-selectivity.* Journal of Porphyrins and Phthalocyanines, 2011. **15**(05n06): p. 441-448.
41. Thiele, M., et al., *Gold nanocubes–Direct comparison of synthesis approaches reveals the need for a microfluidic synthesis setup for a high reproducibility.* Chemical Engineering Journal, 2016. **288**: p. 432-440.
42. Lohse, S.E. and C.J. Murphy, *The quest for shape control: a history of gold nanorod synthesis.* Chemistry of Materials, 2013. **25**(8): p. 1250-1261.
43. Abadeer, N.S., et al., *Distance and plasmon wavelength dependent fluorescence of molecules bound to silica-coated gold nanorods.* ACS nano, 2014. **8**(8): p. 8392-8406.
44. Shi, W., et al., *Synthesis and characterization of gold nanoparticles with plasmon absorbance wavelength tunable from visible to near infrared region.* International Scholarly Research Notices, 2012. **2012**.
45. Meng, L.-q., et al., *Preparation and plasmon resonance properties of Au nanorods and Au nanorods@ SiO 2.* Gold Bulletin, 2020. **53**(1): p. 31-37.
46. Grzelczak, M., et al., *Shape control in gold nanoparticle synthesis.* Chemical Society Reviews, 2008. **37**(9): p. 1783-1791.
47. Pitarke, J., et al., *Theory of surface plasmons and surface-plasmon polaritons.* Reports on progress in physics, 2006. **70**(1): p. 1.
48. Elhani, S., et al., *Surface enhanced Visible Absorption of Dye Molecules in the near-field of Gold nanoparticles.* Scientific reports, 2020. **10**(1): p. 1-11.
49. Yang, X. and B. Li, *Localized and propagated surface plasmons in metal nanoparticles and nanowires.* Intech Open, 2018: p. 21-38.
50. Pillai, S.a. and M. Green, *Plasmonics for photovoltaic applications.* Solar Energy Materials and Solar Cells, 2010. **94**(9): p. 1481-1486.
51. Sharifi, M., et al., *Plasmonic gold nanoparticles: Optical manipulation, imaging, drug delivery and therapy.* Journal of Controlled Release, 2019. **311**: p. 170-189.
52. Ali, M.R., et al., *Synthesis, structure evolution, and optical properties of gold nanobones.* Research on Chemical Intermediates, 2019. **45**(8): p. 3973-3983.
53. Hu, M., et al., *Gold nanostructures: engineering their plasmonic properties for biomedical applications.* Chemical Society Reviews, 2006. **35**(11): p. 1084-1094.
54. Eustis, S. and M.A. El-Sayed, *Why gold nanoparticles are more precious than pretty gold: noble metal surface plasmon resonance and its enhancement of the radiative and nonradiative properties of nanocrystals of different shapes.* Chemical society reviews, 2006. **35**(3): p. 209-217.
55. Li, G., R. Zhu, and Y. Yang, *Polymer solar cells.* Nature photonics, 2012. **6**(3): p. 153-161.
56. Corkish, R., et al., *Applied photovoltaics*. 2013: Routledge.
57. Kalowekamo, J. and E. Baker, *Estimating the manufacturing cost of purely organic solar cells.* Solar Energy, 2009. **83**(8): p. 1224-1231.
58. Kim, H., et al., *Organic solar cells based on conjugated polymers: History and recent advances.* Korean Journal of Chemical Engineering, 2014. **31**(7): p. 1095-1104.
59. Wu, J., et al., *Broadband efficiency enhancement in quantum dot solar cells coupled with multispiked plasmonic nanostars.* Nano Energy, 2015. **13**: p. 827-835.
60. Chen, C.-C., et al., *Visibly transparent polymer solar cells produced by solution processing.* ACS nano, 2012. **6**(8): p. 7185-7190.

61. Liu, Y., et al., *Synergistic effect of surface plasmon resonance and constructed hierarchical TiO 2 spheres for dye-sensitized solar cells.* Nanoscale, 2012. **4**(21): p. 6863-6869.
62. Yeh, N. and P. Yeh, *Organic solar cells: Their developments and potentials.* Renewable and Sustainable Energy Reviews, 2013. **21**: p. 421-431.
63. Mazzio, K.A. and C.K. Luscombe, *The future of organic photovoltaics.* Chemical Society Reviews, 2014. **44**(1): p. 78-90.
64. Jang, Y.H., et al., *Plasmonic solar cells: from rational design to mechanism overview.* Chemical reviews, 2016. **116**(24): p. 14982-15034.
65. Świst, A. and J. Sołoducho, *Organic semiconductors–materials of the future.* CHEMIK nauka-technika-rynek, 2012. **1**: p. 289-296.
66. Brütting, W., et al., *Device efficiency of organic light-emitting diodes: Progress by improved light outcoupling*. 2013, Wiley Online Library.
67. Kahle, F.J., et al., *Crosslinked semiconductor polymers for photovoltaic applications.* Advanced Energy Materials, 2017. **7**(16): p. 1700306.
68. Shin, P.-K., et al., *Effects of organic solvents for composite active layer of PCDTBT/PC71BM on characteristics of organic solar cell devices.* International journal of photoenergy, 2014. **2014**.
69. Mayer, A.C., et al., *Polymer-based solar cells.* Materials today, 2007. **10**(11): p. 28-33.
70. Peet, J., et al., *The role of processing in the fabrication and optimization of plastic solar cells.* Advanced Materials, 2009. **21**(14-15): p. 1521-1527.
71. Lattante, S., *Electron and hole transport layers: their use in inverted bulk heterojunction polymer solar cells.* Electronics, 2014. **3**(1): p. 132-164.
72. Zhang, F., et al., *Polymer photovoltaic cells with conducting polymer anodes.* Advanced Materials, 2002. **14**(9): p. 662-665.
73. Ranjith, K. and R.R. Kumar, *Facile construction of vertically aligned ZnO nanorod/PEDOT: PSS hybrid heterojunction-based ultraviolet light sensors: efficient performance and mechanism.* Nanotechnology, 2016. **27**(9): p. 095304.
74. Ranjitha, A., et al., *Effect of doped TiO2 film as electron transport layer for inverted organic solar cell.* Materials Science for Energy Technologies, 2019. **2**(3): p. 385-388.
75. Löckinger, J., et al., *TiO2 as intermediate buffer layer in Cu (In, Ga) Se2 solar cells.* Solar Energy Materials and Solar Cells, 2018. **174**: p. 397-404.
76. Mishra, A., et al., *Electrode materials for lithium-ion batteries.* Materials Science for Energy Technologies, 2018. **1**(2): p. 182-187.
77. Kim, S.-W., et al., *Fabrication and electrochemical characterization of TiO2 three-dimensional nanonetwork based on peptide assembly.* Acs Nano, 2009. **3**(5): p. 1085-1090.
78. Würfel, P., *Physics Today*. 2005, Wiley-VCH Verlag GmbH & Co. KGaA, Weinheim.
79. Jäger, K.-D., et al., *Solar energy: fundamentals, technology and systems*. 2016: UIT Cambridge.
80. Dittrich, T., *Materials concepts for solar cells*. 2015: World Scientific.
81. Luque, A. and S. Hegedus, *Handbook of photovoltaic science and engineering*. 2011: John Wiley & Sons.
82. Heeger, A.J., *25th anniversary article: bulk heterojunction solar cells: understanding the mechanism of operation.* Advanced Materials, 2014. **26**(1): p. 10-28.
83. Hoppe, H. and N.S. Sariciftci, *Organic solar cells: An overview.* Journal of materials research, 2004. **19**(7): p. 1924-1945.

84. Scharber, M.C., et al., *Design rules for donors in bulk-heterojunction solar cells—Towards 10% energy-conversion efficiency.* Advanced materials, 2006. **18**(6): p. 789-794.
85. Parker, I.D., *Carrier tunneling and device characteristics in polymer light-emitting diodes.* Journal of Applied Physics, 1994. **75**(3): p. 1656-1666.
86. Frohne, H., et al., *Influence of the anodic work function on the performance of organic solar cells.* ChemPhysChem, 2002. **3**(9): p. 795-799.
87. Zang, L., *Energy efficiency and renewable energy through nanotechnology*. 2011: Springer.
88. Petritsch, K., *Organic solar cell architectures*. 2000: na.
89. Gupta, D., S. Mukhopadhyay, and K. Narayan, *Fill factor in organic solar cells.* Solar Energy Materials and solar cells, 2010. **94**(8): p. 1309-1313.
90. Mihailetchi, V.D., et al., *Compositional dependence of the performance of poly (p-phenylene vinylene): methanofullerene bulk-heterojunction solar cells.* Advanced Functional Materials, 2005. **15**(5): p. 795-801.
91. Centeno, A. and F. Xie. *Plasmonic enhanced solar cells*. in *2016 IEEE 6th International Conference on Photonics (ICP)*. 2016. IEEE.
92. Shen, P., et al., *High-performance polymer solar cells enabled by copper nanoparticles-induced plasmon resonance enhancement.* The Journal of Physical Chemistry C, 2016. **120**(16): p. 8900-8906.
93. Wang, M., et al., *Recent process of plasma effect in organic solar cells.* Journal of Energy Chemistry, 2020.
94. Wu, B., et al., *Efficiency enhancement in bulk-heterojunction solar cells integrated with large-area Ag nanotriangle arrays.* The Journal of Physical Chemistry C, 2012. **116**(28): p. 14820-14825.
95. Magdi, S. and M.A. Swillam, *Investigating several ZrN plasmonic nanostructures and their effect on the absorption of organic solar cells.* Journal of Physics D: Applied Physics, 2017. **50**(38): p. 385501.
96. Chalh, M., et al., *Plasmonic Ag nanowire network embedded in zinc oxide nanoparticles for inverted organic solar cells electrode.* Solar Energy Materials and Solar Cells, 2016. **152**: p. 34-41.
97. Xia, F., et al., *Efficiency enhancement of inverted structure perovskite solar cells via oleamide doping of PCBM electron transport layer.* ACS applied materials & interfaces, 2015. **7**(24): p. 13659-13665.
98. Atwater, H.A. and A. Polman, *Plasmonics for improved photovoltaic devices.* Materials for sustainable energy: A collection of peer-reviewed research and review articles from nature publishing group, 2011: p. 1-11.
99. Singh, Y.P., et al., *Enhancement in optical absorption of plasmonic solar cells.* The Open Renewable Energy Journal, 2013. **6**(1).
100. Peter Amalathas, A. and M.M. Alkaisi, *Nanostructures for Light Trapping in Thin Film Solar Cells.* Micromachines, 2019. **10**(9): p. 619.
101. Enrichi, F., A. Quandt, and G.C. Righini, *Plasmonic enhanced solar cells: Summary of possible strategies and recent results.* Renewable and Sustainable Energy Reviews, 2018. **82**: p. 2433-2439.
102. Niesen, B., et al., *Plasmonic efficiency enhancement of high performance organic solar cells with a nanostructured rear electrode.* Advanced Energy Materials, 2013. **3**(2): p. 145-150.
103. Stavytska-Barba, M. and A.M. Kelley, *Surface-enhanced Raman study of the interaction of PEDOT: PSS with plasmonically active nanoparticles.* The Journal of Physical Chemistry C, 2010. **114**(14): p. 6822-6830.

104. Shin, J., et al., *Harvesting near-and far-field plasmonic enhancements from large size gold nanoparticles for improved performance in organic bulk heterojunction solar cells.* Organic Electronics, 2019. **66**: p. 94-101.
105. Park, H.J. and L.J. Guo, *Optical enhancement effects of plasmonic nanostructures on organic photovoltaic cells.* Chinese Chemical Letters, 2015. **26**(4): p. 419-425.
106. Jheng, J.-Y., et al., *Decahedral gold nanoparticles for enhancing performance of polymer solar cells.* Dyes and Pigments, 2017. **138**: p. 83-89.
107. Wu, J.-L., et al., *Surface plasmonic effects of metallic nanoparticles on the performance of polymer bulk heterojunction solar cells.* ACS nano, 2011. **5**(2): p. 959-967.
108. Fung, D.D., et al., *Optical and electrical properties of efficiency enhanced polymer solar cells with Au nanoparticles in a PEDOT–PSS layer.* Journal of Materials Chemistry, 2011. **21**(41): p. 16349-16356.
109. He, Y., et al., *Improved power conversion efficiency of inverted organic solar cells by incorporating Au nanorods into active layer.* ACS applied materials & interfaces, 2015. **7**(29): p. 15848-15854.
110. Liu, C., et al., *Unique gold nanorods embedded active layer enabling strong plasmonic effect to improve the performance of polymer photovoltaic devices.* The Journal of Physical Chemistry C, 2016. **120**(11): p. 6198-6205.
111. Wang, D.H., et al., *Enhanced power conversion efficiency in PCDTBT/PC70BM bulk heterojunction photovoltaic devices with embedded silver nanoparticle clusters.* Advanced Energy Materials, 2011. **1**(5): p. 766-770.
112. Wang, D.H., et al., *Enhanced light harvesting in bulk heterojunction photovoltaic devices with shape-controlled Ag nanomaterials: Ag nanoparticles versus Ag nanoplates.* Rsc Advances, 2012. **2**(18): p. 7268-7272.
113. Topp, K., et al., *Impact of the incorporation of Au nanoparticles into polymer/fullerene solar cells.* The Journal of Physical Chemistry A, 2010. **114**(11): p. 3981-3989.

Chapter 3

Experimental

3.1 Introduction

The synthesis of different gold (Au) nanostructures was successfully achieved using seed-mediated growth method. The Au nanostructures were thereafter incorporated into the PCDTBT: $PC_{70}BM$ active layer. Organic solar cells (OSCs) with TiO_2 as an electron transport layer (ETL) and PEDOT: PSS as the hole transport layer (HTL) were fabricated. This chapter presents the synthesis and characterization of Au nanospheres, nanorods, and nanoprisms. In addition, the active layer, ETL and HTL were deposited. Fabrication of OSCs, their *I-V* measurements performance under dark and light are also discussed.

3.2 Materials and Substrate cleaning

3.2.1 Materials

Hydrogen tetrachloroaurate (III) trihydrate ($HAuCl_4.3H_2O$), cetyltrimethylammonium bromide (CTAB), sodium borohydride ($NaBH_4$), L- ascorbic acid, silver nitrate ($AgNO_3$), trisodium citrate dihydrate ($Na_3C_6H_5O_7$), potassium iodide (KI), hydrochloric acid (HCl, 32%) and titanium (IV) isopropoxide (TTIP, 97%) were obtained from Sigma-Aldrich and used as received. Deionized (DI) water and 1-butanol and chlorobenzene were used as solvents for all the solution preparations. Poly[N-9'-heptadecanyl-2,7-carbazole-alt-5,5-(4',7'-di-2-thienyl-2',1',3'-benzothiadiazole)] PCDTBT, [6,6]-Phenyl-C_{70}-butyric acid methyl ester ($PC_{70}BM$), Poly (3,4- ethylene dioxythiophene): polystyrene sulfonate (PEDOT: PSS), and patterned indium tin oxide (ITO) were purchased from Ossila.

3.2.2 Substrate cleaning

All glassware was cleaned using aqua regia, which is a mixture of hydrochloric acid and nitric acid in a molar ratio of 3:1. The ITO glass substrates were sonicated with deionized water, ethanol, and acetone for 10 min each and dried with pressurized nitrogen gas. The ITO

substrates were then exposed to UV Ozone for 15 min to further remove fatty contaminations on the surface before spin coating.

3.3 Synthesis of gold nanorods

3.3.1 Preparations of gold seeds

The schematic diagram of Au seed preparation is shown in Figure 3. *1*. The Au seed solution was prepared by dissolving 0.3644 g of CTAB in 10 ml of DI water. This was followed by addition of 500 µl of 10 mM $HAuCl_4.3H_2O$, and 600 µl of 10 mM $NaBH_4$. The solution turned to golden orange after 1 h with vigorously stirring. Thereafter, the solution was set to age at room temperature for 2 h. After 2 h, the precursor solution was used in the preparation of Au seeds.

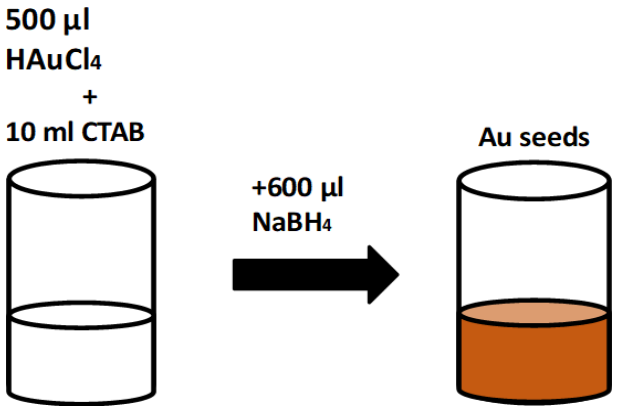

Figure 3. 1. Schematic illustration of the preparations of gold seeds.

3.3.2 Growth of gold nanorods

Figure 3. *2* shows the schematic diagram of the preparation of gold nanorods (AuNRs). The solution was prepared by dissolving 3.646 g of CTAB in 100 ml of DI water. The solution became clear and transparent after vigorous stirring. 0.0152 g of $HAuCl_4.3H_2O$ (5 ml of 10 mM), 0.3 mg of $AgNO_3$ (0.2 ml of 10 mM), 2 ml of 10.2 M HCl, and 0.0145 g of ascorbic acid (800 µl of 0.1 M) were respectively added at 27°C with constant stirring at 800 rpm/min using the magnetic bead. Before the addition of ascorbic acid, the solution was golden orange and it quickly became colourless, indicating the reduction of the Au^{3+} ions in solution to Au^{+}. Ascorbic acid is too weak to fully reduce the Au salt without the addition of Au seeds.

Finally, 240 µl of Au seeds were added, while the mixture was rapidly stirred for 10 s and restored to 800 rpm/min. After 2 h of stirring, no colour change was observed. After 20 h, the color changed from colourless to dark purple. AuNRs were separated from the mother solution by centrifugation at 5300 rpm for 20 min, then washed with DI water 2 times to remove excess CTAB surfactant which dispersed in DI water.

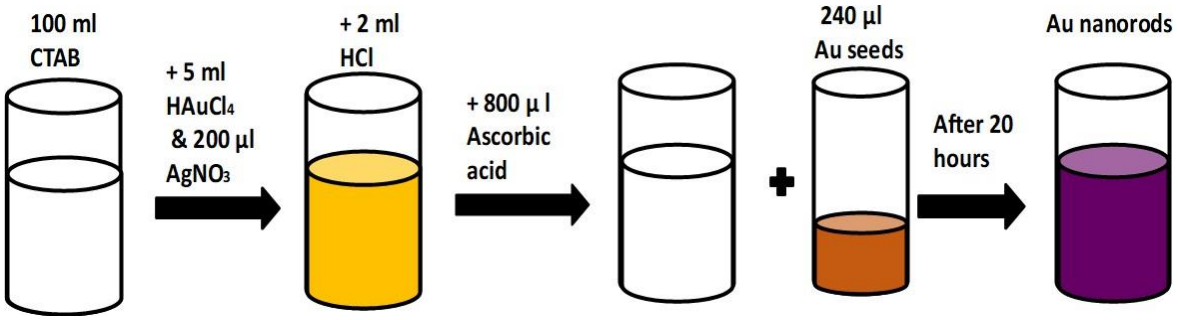

Figure 3. 2 The schematic diagram for preparation of gold nanorods.

3.4 Synthesis of gold nanospheres and nanoprisms

3.4.1 Synthesis of gold nanospheres

The schematic illustration of the preparation of Au nanospheres is shown in Figure 3. *3*. Au seed solution was prepared by mixing 1.6 mg of $HAuCl_4$ (10 ml of 0.5 mM) with 1.4 mg of $Na_3C_6H_5O_7$ (10 ml of 0.5 mM) in a beaker. While vigorously stirring, 2.2 mg of $NaBH_4$ (600 µl of 0.1 M) was added to the beaker, which turned the solution to light red. After 2 min the colour changed to red-maroon, and it was stirred for 5 min at 1000 rpm at 27.9°C. The red-maroon solution was set for 2 h in the dark before further processing.

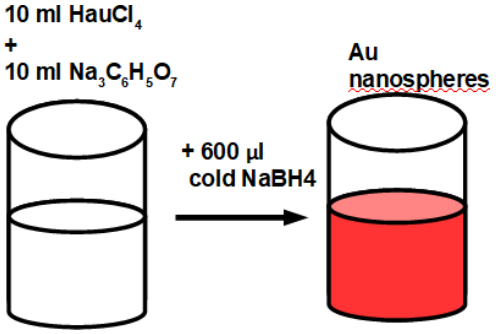

Figure 3. 3. Schematic illustration of the preparations of gold nanospheres.

3.4.2 Synthesis of Au nanoprisms

3.4.2.1 Stock growth solution

A 20 ml stock growth solution containing 1.3 mg $HAuCl_4$ (10 ml of 2.5 x 10^{-4} M) and 0.36445 g CTAB (10 ml of 0.1 M) was prepared in a beaker. It was stirred and heated at 50°C for 10 min to dissolve CTAB. After 10 min, the solution was clear orange in colour. The solution was then cooled to room temperature for 15 min before being used.

3.4.2.2 Growth of Au nanoprisms

Figure 3. *4* presents the schematic diagram used for the preparation of Au nanoprisms. 1.0 mg of KI (5 ml of 100 µM) was added to the 20 ml stock solution. The solution was stirred at 250 rpm for 10 min while the temperature was maintained at 15°C and a light-yellow colour was observed. After the freshly prepared 7 mg ascorbic acid (400 µl of 0.1 M) solution was added, it became colourless and was stirred for 10 min. 50 µl of Au seeds were added and stirred for 20 min until the colour was dark purple. The dark purple solution was placed in a water bath at (27°C) and kept overnight. It was later centrifuged for 10 min at 1600 rpm.

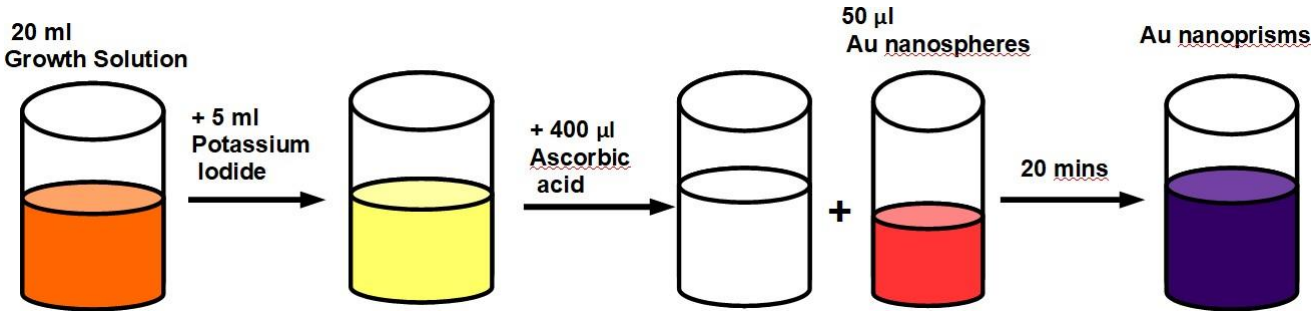

Figure 3. 4. Schematic diagram for the preparations of gold nanoprisms.

3.5 Fabrication of the solar cell

3.5.1 The blend PCDTBT: $PC_{70}BM$ deposition

The active layer blend solution was prepared by dissolving PCDTBT and $PC_{70}BM$ in a ratio of 1:4 in chlorobenzene. The blend was stirred at 500 rpm at 25°C for 12 h using a magnetic

stirrer and thereafter filtered using a 0.01 μm filter before spin coating. Three different nanostructures such as Au nanospheres, nanorods, and nanoprisms (1% v/v each sample) were drop-casted into the glass substrate to prepare thin films, and the PCDTBT: $PC_{70}BM$ was spin-coated at 700 rpm for 30 s and dried in a vacuum oven at 70°C for 10 min. The active layer of the solar cell was prepared by spin-coating PCDTBT: $PC_{70}BM$ (1:4) in chlorobenzene onto titanium dioxide (TiO_2) coated substrate, and the films were dried in a vacuum oven at 70°C for 10 min. Au nanospheres, nanorods and nanoprisms with volume ratio of 1% v/v were added between TiO_2 and PCDTBT: $PC_{70}BM$ layers.

3.5.2 TiO_2 deposition

The precursor solution of compact TiO_2 layer of 0.3 M was prepared by mixing 5 ml of 1-butanol and 0.55 ml of titanium diisopropoxide all sourced from Sigma-Aldrich. The compact TiO_2 was deposited by spin coating the 0.3 M precursor solution into the ITO at 3000 rpm for 30 s. The films were dried in an oven for 5 min at 125°C. The experiment was repeated once before annealing in a furnace at 500°C for 30 min to form the electron transport layer.

3.5.3 PEDOT: PSS deposition

PEDOT: PSS was sourced from Ossilla in a solution form. The hole transport layer was deposited by spin-coating PEDOT: PSS onto the active layer at 3000 rpm for 40 s. The film was dried on a hot plate at 150°C for 15 min. The 80 nm silver (Ag) metal was deposited as top contact using thermal evaporation at the pressure of 5.5×10^{-6} mbars.

3.6 Characterization

3.6.1 Ultraviolet-Visible spectroscopy

Ultraviolet-visible (UV-Vis) spectroscopy is an equipment used to determine the light absorption across the ultraviolet and visible ranges of the electromagnetic spectrum [1]. The UV-Vis absorbance causes the excitation of electrons from a low-energy state to an excited state. When incident light strikes a material, absorbance, transmittance, and reflectance can take place. The sample is illuminated with electromagnetic rays ranging from 200 - 400 nm for ultraviolet and 400 - 700 nm for visible is used. The UV-Vis absorption is analyzed by

measuring the intensity of light before (*Io*) and after the sample (*I*) is placed in the light path [2]. Figure 3. *5* present the schematic diagram of the UV-Vis spectrophotometer.

In this study, the absorbance measurements of AuNSs and PCDTBT: PCBM thin films were obtained using Agilent Cary 60 UV-Vis spectrophotometer. Before the measurements, baseline correction was done using deionized water (solvent for Au nanostructures) and a clean glass substrate for the thin films. After the baseline and zero correction, the solution of Au nanostructures was poured into the cuvettes using a dropper, and then placed into the sample holder for measurement. A different sample holder was used for the measurements of absorbance of PCDTBT: PCBM thin films to avoid contaminations.

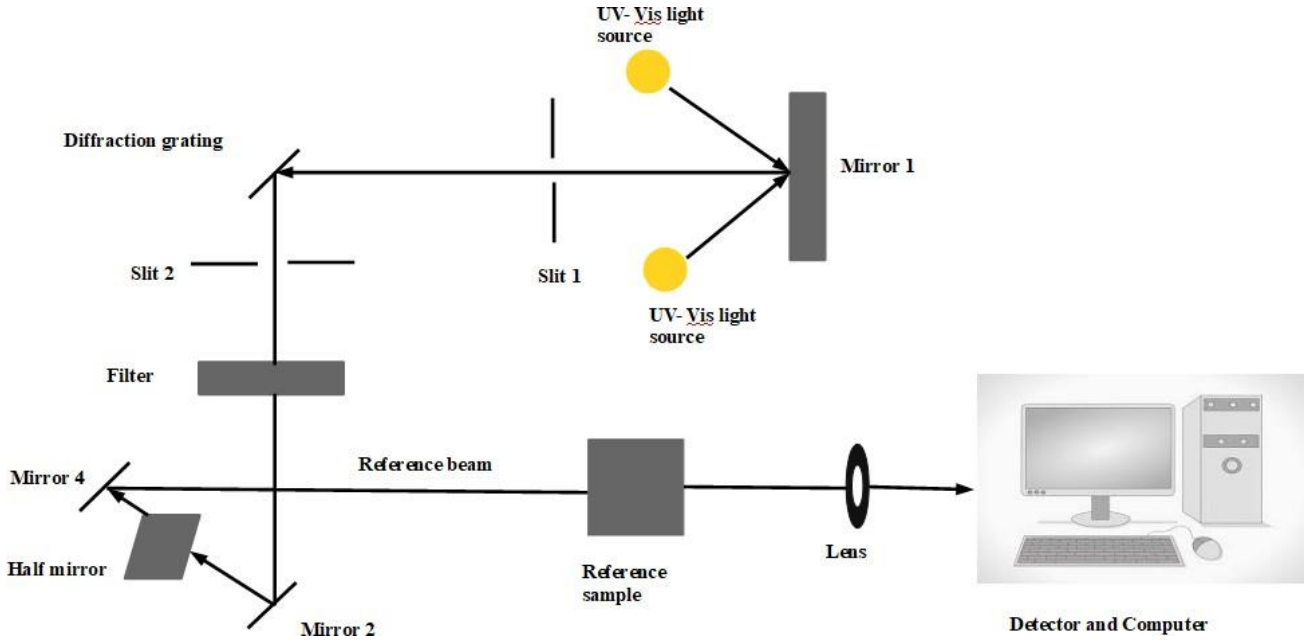

Figure 3. 5. Schematic diagram of UV-Vis spectrophotometer.

3.6.2 X-ray diffraction

X-ray diffraction (XRD) is a technique used for studying the structural properties of materials. This is done by determining the crystal structure, size, defects of materials, and lattice parameters. Also, the XRD can give more information if material prepared is amorphous, crystalline, and has unit cell dimensions. When an x-ray beam with a particular wavelength strikes a sample at an incident angle θ, constructive interference takes place when Bragg's law is satisfied as in equation 3. 1 [3]

$$n\lambda = 2d\,Sin\,\theta \qquad 3.\ 1$$

where n is the integer, λ is the wavelength, d is the spacing between diffracting planes and θ is the incident angle. To calculate the crystallite size Debye-Scherrer's formulae presented by equation 3. 2 and equation 3. 3 were used to calculate lattice parameters and crystallite sizes:

$$D = \frac{K\,\lambda}{\beta\,cos\,\theta} \qquad 3.\ 2$$

$$a = d\,(h^2 + k^2 + l^2)^{\frac{1}{2}} \qquad 3.\ 3$$

where D is the crystallite size, K is the dimensionless shape factor, λ is the X-ray wavelength, β is the full width at half maximum, θ is Bragg's angle, a is the lattice constant, d is d-spacing and (hkl) is the miller indices [4]. The schematic diagram of the XRD machine and components is shown in Figure 3. *6*. In this study, the German Bruker D2 Phase X-ray diffractometer with CuKα radiation (1.5418 Å) source and 2θ range of 20℃ to 80℃ was used. Au nanostructures were dried on the glass substrate since the equipment cannot run liquid samples prior to measurements. The other thin films were used as prepared.

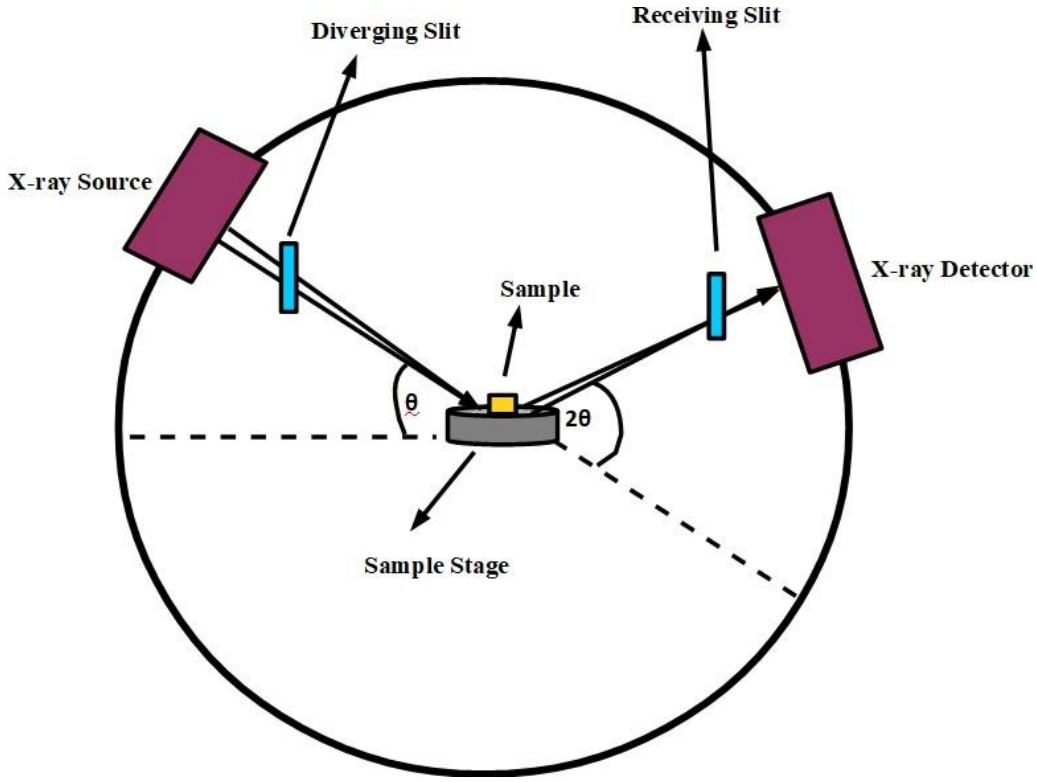

Figure 3. 6. Schematic diagram of XRD components.

3.6.3 Raman Spectroscopy

Raman spectroscopy is a non-destructive and non-invasive technique that is used to assess molecular vibrations and has potential as an analytical method in the characterization of materials in any state (solid, liquid, gas) [5]. Raman spectrum can be used for crystalline materials (phonon interaction) and organic substances (functional groups fingerprinting), amorphous, polymers, and liquids depending on the strength of Raman modes. Raman scattering is an inelastic scattering, whereby the kinetic energy of an incident photon is increased (stokes Raman scattering) or reduced (anti-stokes Raman scattering) during an interaction [6]. It depends on the inelastic scattering of electromagnetic radiation by molecules or atoms. The scattering of the photons with different frequencies from the light is due to the inelastic scattering. These two scattering processes are Rayleigh and anti-strokes scattering.

The light from the laser source interacts with the sample emitting radiation, which is then collected by lens, and passed as a signal into a grating monochromator. This signal is therefore measured by a photomultiplier tube camera before being processed by a computer which depicts the intensity against the Raman Shift spectrum. Figure 3. *7* presents a schematic diagram of the Raman spectroscopy setup. In this study, WiTec alpha300 RAS+ confocal Raman microscope with a 532 nm excitation laser was used. Before doing the measurements AuNSs were dried on a glass substrate and for thin films were spin-coated, then placed in the sample holder.

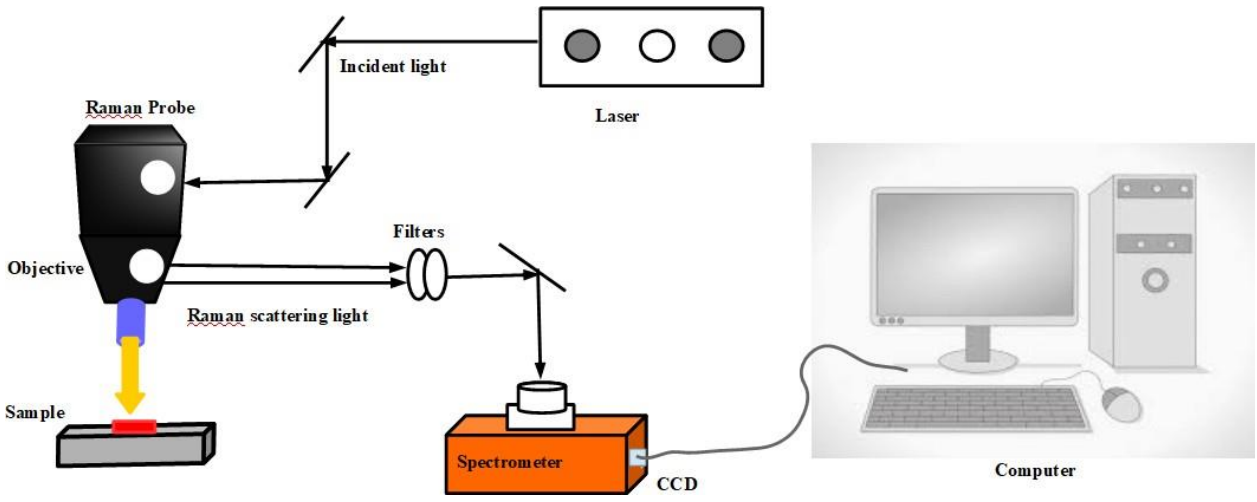

Figure 3. 7. Schematic diagram of the Raman spectroscopy setup.

3.6.4 Transmission electron microscopy

Transmission electron microscopy (TEM) is an equipment used to study the elemental composition, oxidation states of elements, bond distances, morphology, symmetry, and nano porosity [7]. Compared to light microscopes, electron microscopes generate images of material microstructure with higher magnification and resolution. The high resolution of electron microscopes results from electrons short wavelengths. The wavelength of electrons is about 10 000 times shorter than that of visible light [3]. TEM is made up of different components along its optical paths which are: light source, condenser lenses, specimen stage, objective lenses, and projector lenses.

The electron gun is used to generate a high-energy electron beam for illumination. The electron's energy determines the wavelength; hence the acceleration voltage determines the resolution. The higher the acceleration, the higher the resolution. Electromagnetic lenses utilize the electron charge interaction to produce a high-energy beam. The other lenses (condensing lenses) are used to decrease the magnification of the electron beam produced. The objective, intermediate, and projector lenses are used to control the magnification. Intermediate lenses are used between the diffraction mode and image mode [8]. The schematic diagram of TEM is shown in Figure 3. *8.* In this work, the morphology of the nanostructures was studied using JEM-2100F Field Emission transmission electron (FE-TEM). The gold nanostructure solution was sonicated for 15 mins before being drop-casted into the copper grid and left to dry.

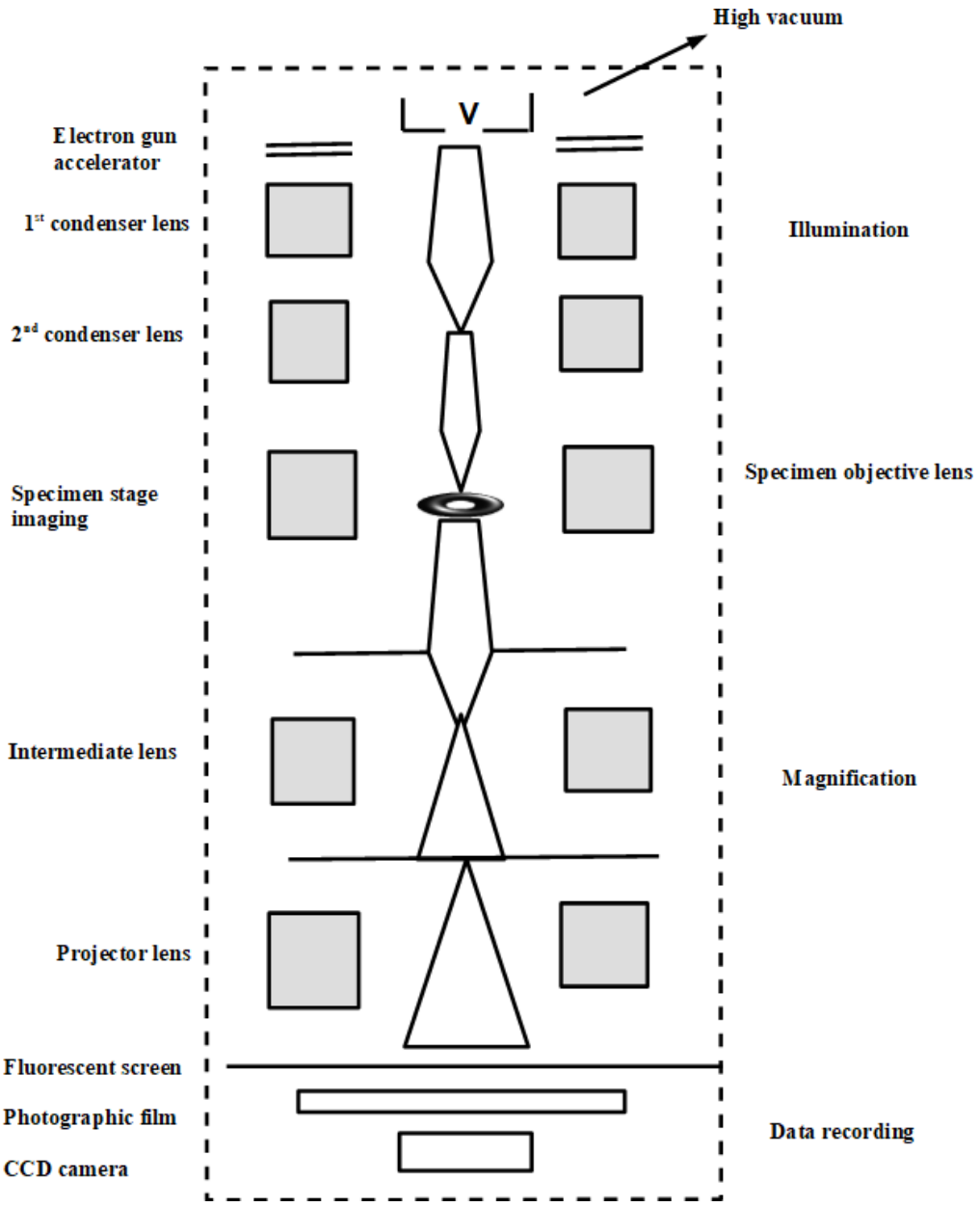

Figure 3. 8. Schematic structure of transmission electron microscope (TEM) and the optical path.

3.6.5 Scanning electron microscopy

Scanning electron microscope (SEM) is the widely used type of electron microscope. It determines microscope structure by scanning the surface of materials like the scanning confocal microscopes but with much higher resolution and greater depth of field. SEM image is formed by a focused electron beam that scans over the surface area of the specimen [3]. The magnetic lenses are used to focus the electrons to a spot. The main components of SEM include electron gun, condenser lenses, objective lenses, vacuum pump, detectors, control

balance, and monitor. The backscattered electrons are used for performing SEM measurements due to their low energies and determining the brightness of the signal. Figure 3. *9* shows the schematic diagram of SEM and its components. In this study the Field emission scanning electron microscope (Zeiss cross beam 540 FE-SEM microscopes) operating at 2 Kv was used. Before analyzing the samples in the SEM machine, they were coated using carbon to reduce the charging effect and enhance the surface conductivity from the incoming electron beam.

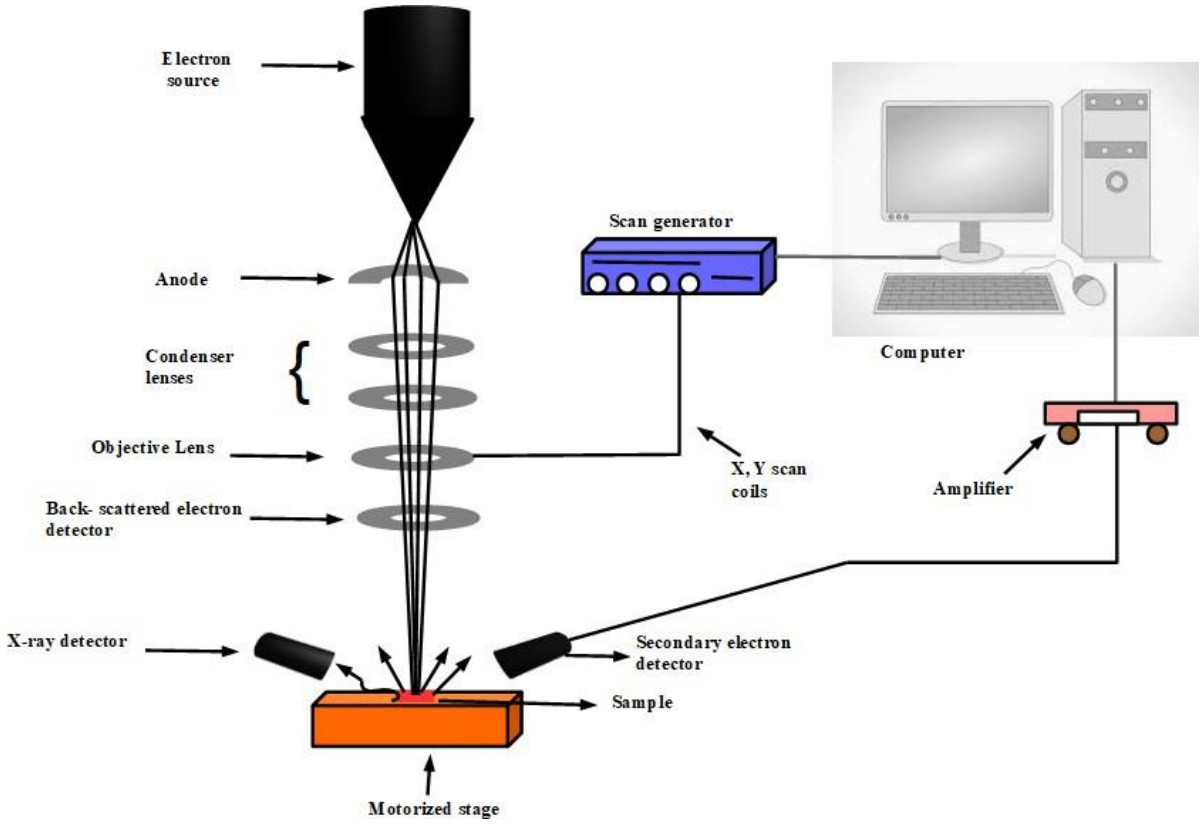

Figure 3. 9. Schematic diagram of a scanning electron microscope.

3.6.6 Energy- dispersive x-ray spectroscopy

Energy-dispersive X-ray spectroscopy (EDS) is a technique used to identify the elements or elemental composition present in any given material. It is usually coupled with SEM or TEM. The EDS microanalyzer in an electron microscope uses a primary electron beam to excite the emission of characteristics X-rays from the sample atoms. It can also examine chemical compositions in a microscopic area since the electron beam can be focused onto the area on a

sample [3]. The elements in the materials are obtained when the EDS detector separates the x-rays of different elements into the energy spectrum. The spectrum has the peak intensity (x-ray count) against energy (KeV). In this study, EDS (oxford instruments) coupled with SEM, operating at 20 Kv using Aztec 3.0 SPI software was used for elemental composition.

3.6.7 Current density-voltage (J-V) measurement of the solar cells

Figure 3. *10* present the setup I-V system. In this study, dark current-voltage measurements were conducted in a dark room using the automatic I-V system from Ossila. The light measurements were performed under a solar simulator (Oriel LCS-100^{TM} Small Area So11A Series, Newport) with simulated solar output conditions of 100 mW/cm^2 and AM1.5 G reference spectral filtering and the automatic I-V system. This was used to measure the performance of the solar cells.

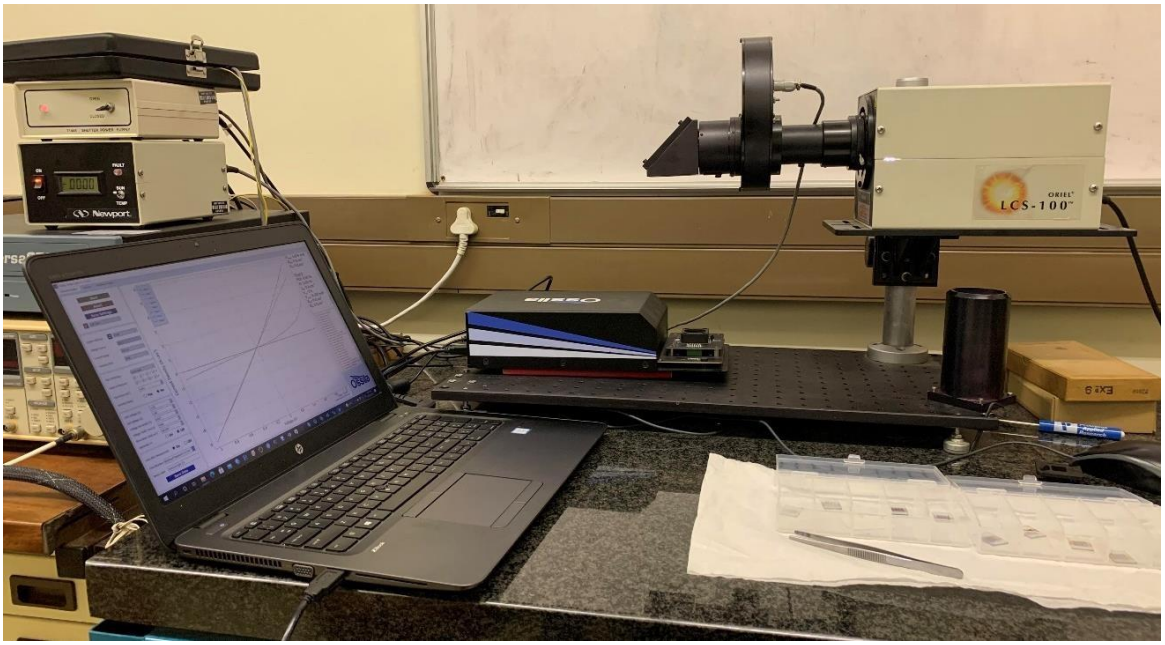

Figure 3. 10. A picture of the I-V system with the Oriel Cornerstone Newport solar simulator used in I-V measurements.

References

1. Vo-Dinh, T., *Handbook of spectroscopy*. 2006: John Wiley & Sons.
2. Picollo, M., M. Aceto, and T. Vitorino, *UV-Vis spectroscopy.* Physical sciences reviews, 2019. **4**(4).
3. Leng, Y., *Materials characterization: introduction to microscopic and spectroscopic methods*. 2009: John Wiley & Sons.
4. Ogundare, O.D., et al., *Crystallite size determination of thermally deposited Gold Nanoparticles.* Procedia Manufacturing, 2019. **30**: p. 173-179.
5. Omidi, M., et al., *Characterization of biomaterials*, in *Biomaterials for oral and dental tissue engineering*. 2017, Elsevier. p. 97-115.
6. Jacob, L.J., and H.-P. Deigner, *Nanoparticles and nanosized structures in diagnostics and therapy*, in *Precision Medicine*. 2018, Elsevier. p. 229-252.
7. Che, M. and J.C. Védrine, *Characterization of solid materials and heterogeneous catalysts: from structure to surface reactivity*. 2012: John Wiley & Sons.
8. Deepak, F.L., A. Mayoral, and R. Arenal, *Advanced transmission electron microscopy: Applications to nanomaterials*. 2015: Springer.

Chapter 4

Results and discussion

4.1 Introduction

In this chapter, results obtained from the synthesis of gold (Au) nanostructures using the seed-mediated method are reported. These Au nanostructures (nanospheres, nanorods, and nanoprisms) were incorporated into the PCDTBT: $PC_{70}BM$ active layer of the solar cell. A comparative study on the effect of different Au nanostructures on the performance of PCDTBT: $PC_{70}BM$ solar cells was performed. The active layer of organic solar cell, hole transport layer and electron transport layer were spin-coated individually and characterized. The fabrication of the solar cell, current-voltage (I-V) measurements, and solar cell parameters of the pristine device and related plasmonic devices are also discussed in this chapter.

4.2 Optical, structural, and morphological properties of gold nanostructures synthesized by the seed-meditated method.

In this section, the results from the synthesized Au nanostructures (nanospheres, nanorods, and nanoprisms) by the seed-mediated growth method are presented. The optical, structural, and morphological properties of Au nanospheres, nanorods, and nanoprisms are discussed. XRD spectra showed the face-centered cubic (fcc) crystal structure and Raman spectroscopy showed sharp and strong vibrational modes for Au. UV-Vis shows a red shift in the absorption of Au nanostructures, observed from 395 to 629 nm. On the other hand, SEM and TEM confirmed the shapes and sizes of Au nanostructures and Au seeds and nanospheres with average sizes of 4 and 6 nm, respectively. The average edge length of 68 nm for Au nanoprisms while the Au nanorods had a length of 70 nm and a width of 40 nm (aspect ratio of 1.9).

4.2.1 Optical properties

Au nanostructures absorb light in the ultraviolet and visible regions due to surface plasmon resonance. The UV-Visible absorption spectra of Au nanostructures are presented in Figure 4.*1*. From this study, an absorbance peak of 395 nm was obtained for Au seeds. For Au nanospheres (AuNSs), a broader absorbance peak of 511 nm was observed. Au nanoprisms

presented a broader and low-intensity absorbance peak of 543 nm. Two absorbance peaks were observed for Au nanorods (AuNRs). The transverse plasmon peak was 528 nm and the longitudinal plasmon peak was 629 nm, confirming that AuNRs of large sizes were successfully synthesized. In this study, a red shift in the absorption spectra was noted for Au seeds, NSs, NRs, and nanoprisms. As the sizes of the different Au nanostructures increased the wavelength also increased, with Au seeds being the smallest and AuNRs the largest.

The plasmonic absorption peaks of the Au nanostructures obtained in this study are similar to what other researchers have reported [1, 2]. For example, Zhuang *et al*. reported the synthesis of gold nanoparticles (AuNPs) using the seed-mediated method. The results showed that AuNSs had an absorption peak at 530 nm. AuNRs had two absorption peaks at 520 and 780 nm, due to the transverse and longitudinal plasmon absorption, where the peaks were broader and more intense. The concentration of AuNPs has been standardized by absorption [1]. Another study by Hailey *et al*. reported Au nanoprisms absorption peaks at 526 nm and a second extended peak at 774 nm was observed. The absorption peaks depend on the shape and sizes of AuNPs [2].

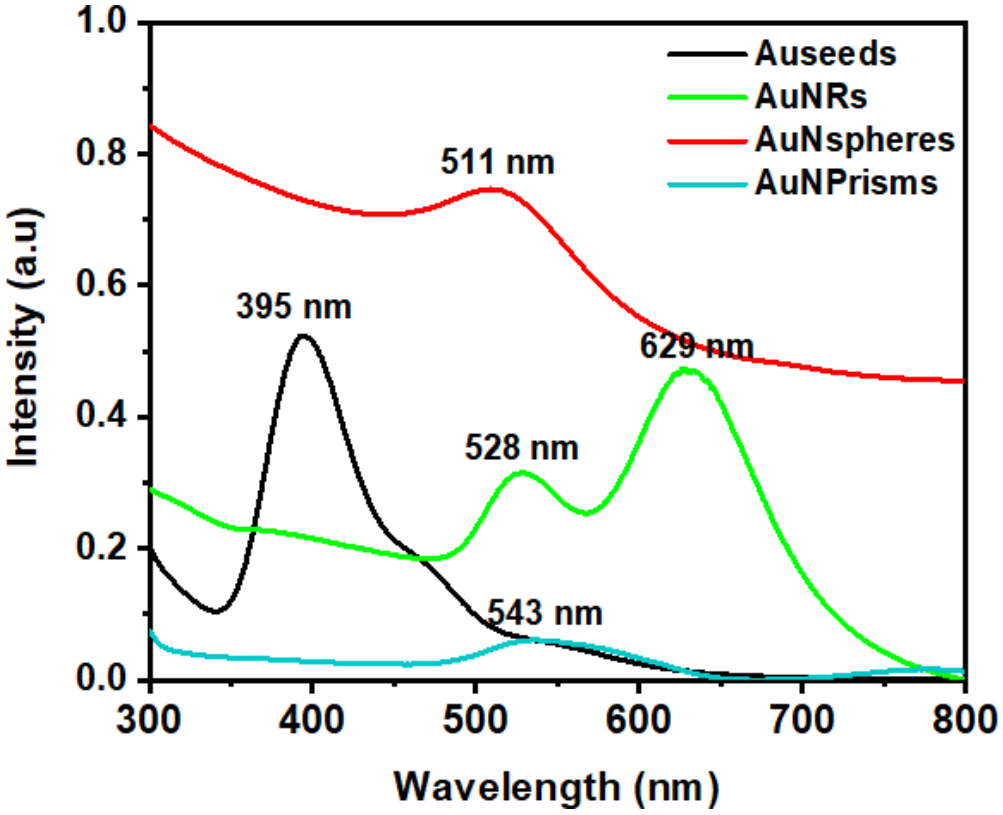

Figure 4.1. UV-Vis absorption spectra for Au seeds, nanospheres, nanorods, and nanoprisms.

4.2.2 Surface morphology

4.2.2.1 TEM analysis

TEM images of Au nanostructures confirm that Au NSs, NRs, and nanoprisms were successfully synthesized using the seed-mediated approach method. Figure 4.*2*(a) and (b) show Au seeds and AuNSs with an average diameter of 4 and 6 nm, respectively. Monodisperse and well-formed shape AuNRs are presented in Figure 4.*3* and the length of 70 nm and width of 40 nm was determined as shown by the histogram in Figure 4.*4*, giving the aspect ratio of 1.9. The TEM micrographs of Au nanoprisms are presented in Figure 4.*5*. Most of the nanoprisms have an edge length of 68 nm, although smaller and larger prisms were observed. The shape is well-formed with no sharp edge tips.

Similar studies have been reported by other researchers. For example, Cramer *et al*. reported the synthesis of AuNSs and Au seeds by using the seed-mediated method. The Au seed had an average size of 4 nm and AuNSs had average sizes ranging from 5-8 nm [2]. Huei *et al.* [3] reported mini AuNRs with tunable longitudinal surface plasmon resonance from 600 - 1300 nm. A seed-mediated growth method and two weak reducing agents were used to tune the aspect ratios of the mini AuNRs from 2.2 to 10.5. The mini AuNRs had a length size ranging from 19.3 to 21.7 nm and a width size range of 9.0 - 5.8 nm. Mojie *et al.* [4] reported the role of halide ions in the seed-mediated synthesis of Au nanoprisms. Au seeds had an average size of 5.2 nm and Au nanoprisms had an average edge length of 145 nm.

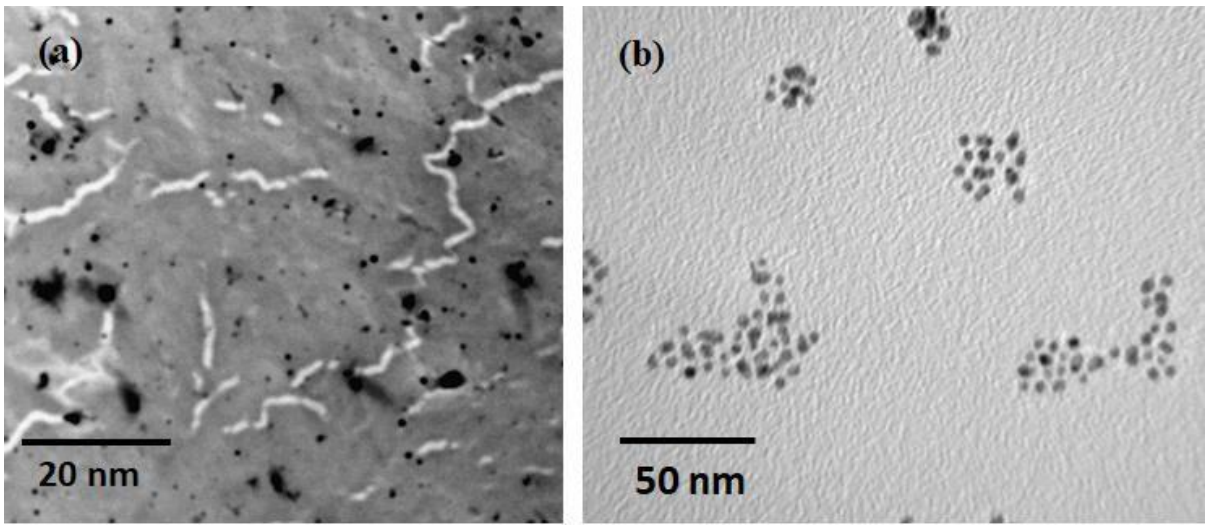

Figure 4.2. TEM images of (a) Au seeds with an average size of 4 nm and (b) Au nanospheres with an average size of 6 nm.

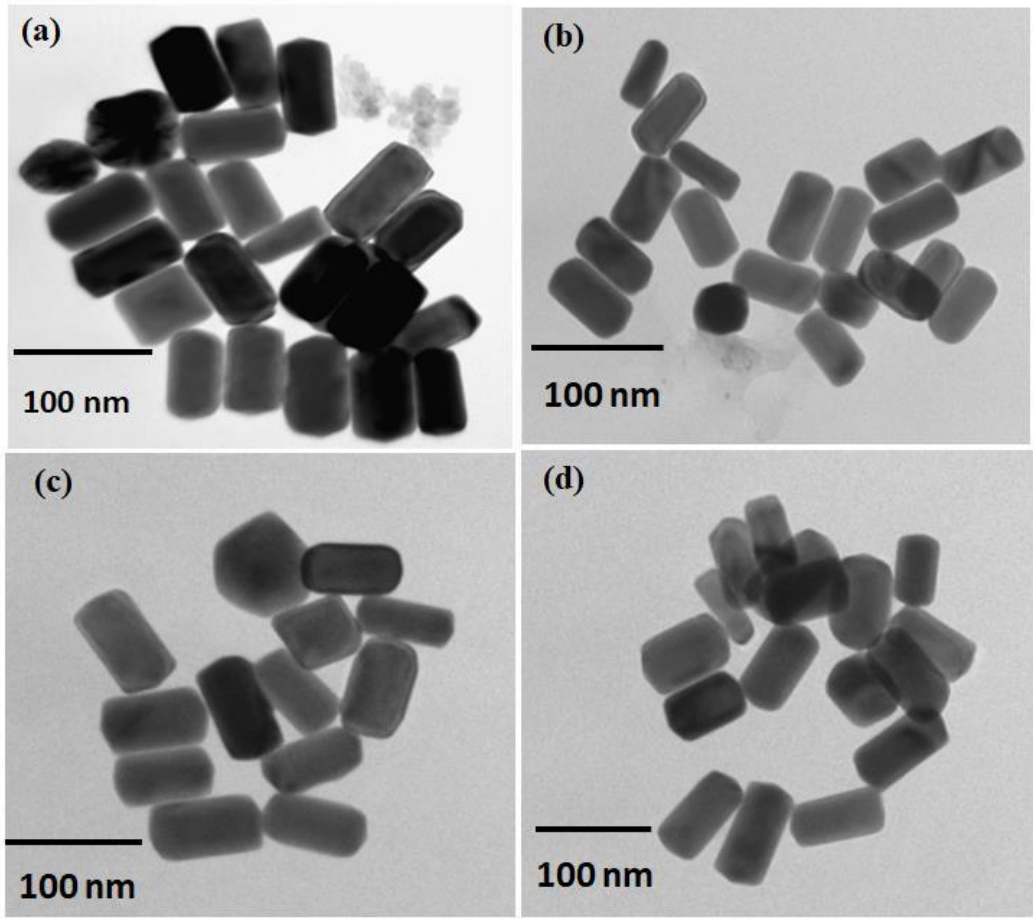

Figure 4.3. TEM images for Au nanorods with length × width of 70 × 40 nm (aspect ratio 1.9).

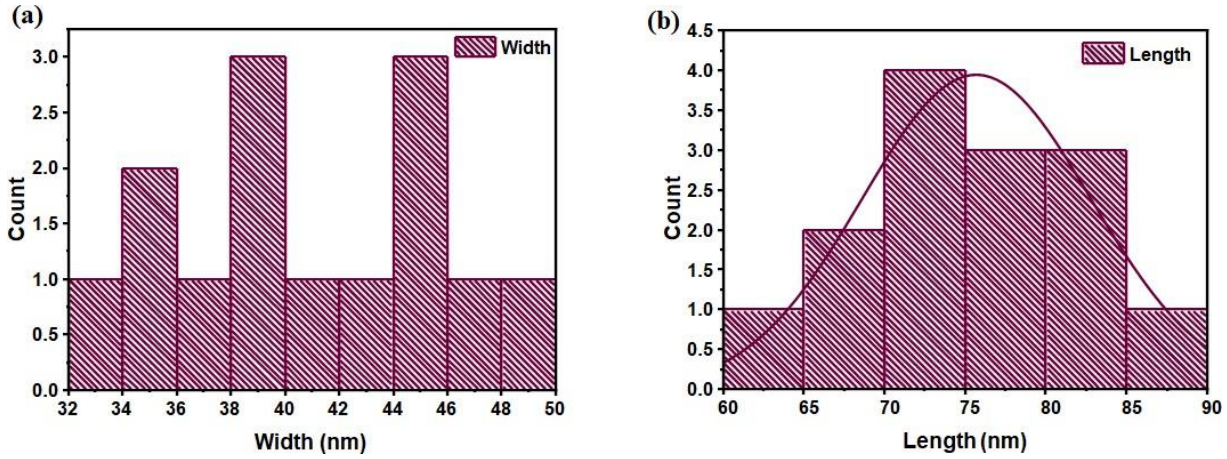

Figure 4. 4 Histogram for Au nanorods (a) width and (b) length.

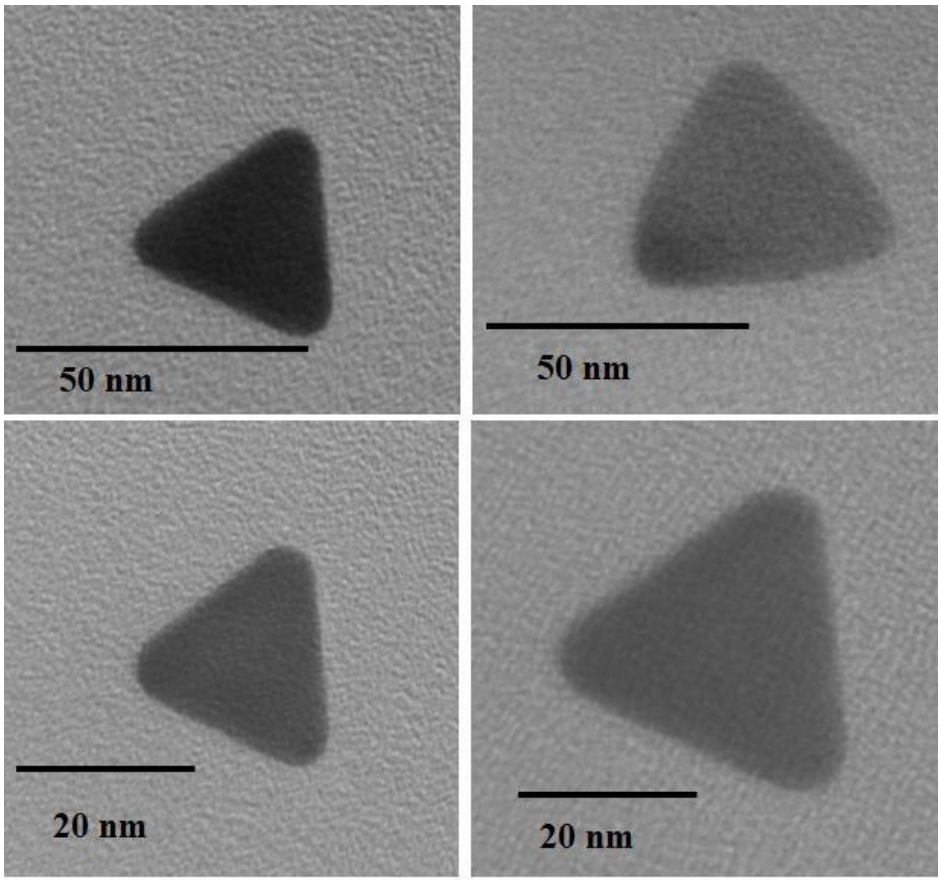

Figure 4.5. TEM images of Au nanoprisms with an edge length of 68 nm.

4.2.2.2 SEM analysis

Figure 4.*6* shows the SEM images of Au nanostructures. The micrographs revealed that the synthesized AuNPs consist of Au seeds, nanorods and nanospheres. Au seeds which were used to synthesize AuNRs, revealed small, aggregated particles with a grain size of 2.6 nm, as shown in Figure 4.*6*(a) and AuNRs in Figure 4.*6*(b) with an aspect ratio of 1.9, confirming that the sample had good surface morphology and grain size of 130 nm. The obtained grain size was largely due to the large size of the AuNRs. For AuNSs in Figure 4.*6*(c), spherical nanoparticles with a grain size of 14 nm were observed. Figure 4.*6*(d) shows Au nanoprims sample with a grain size of 14 nm, desired shape of triangular nanoprisms was not observed but only impurities that resembled rods-like and spherical were seen. Figure 4.*7* shows the Gaussian fit of Au NRs, NSs, and nanoprisms. From the fitting, the distribution size increased as the shape of AuNRs revealed the highest diameter while Au seeds were the smallest. The Energy-dispersive X-ray spectroscopy (EDS) shown in Figure 4. 8, confirmed the presence of

Au in the solution of all samples. The other peaks are associated with the glass substrate that was used in drying the samples.

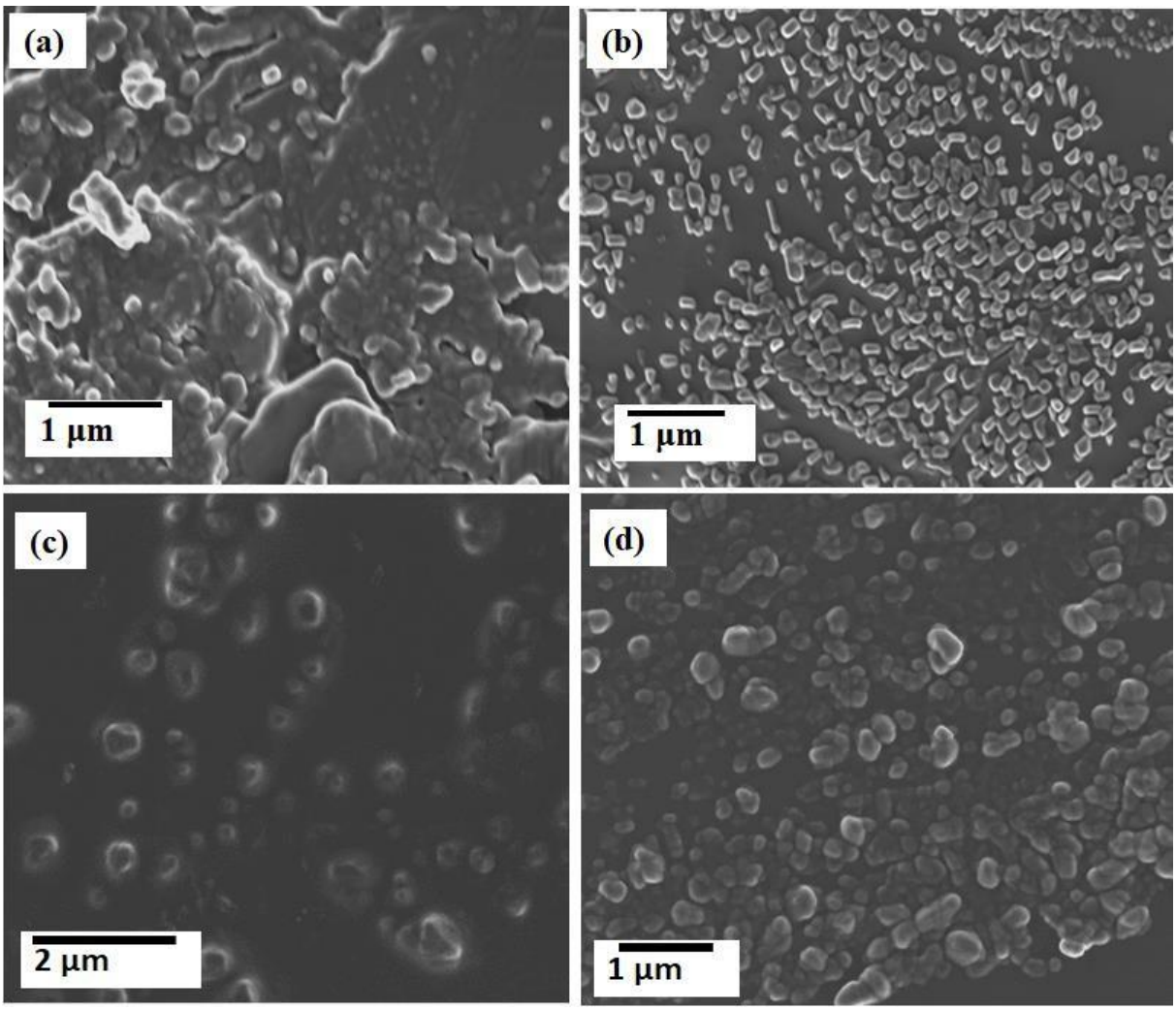

Figure 4.6. SEM images for (a) Au seeds, (b) Au nanorods, (c) Au nanospheres, and (d) Au nanoprisms.

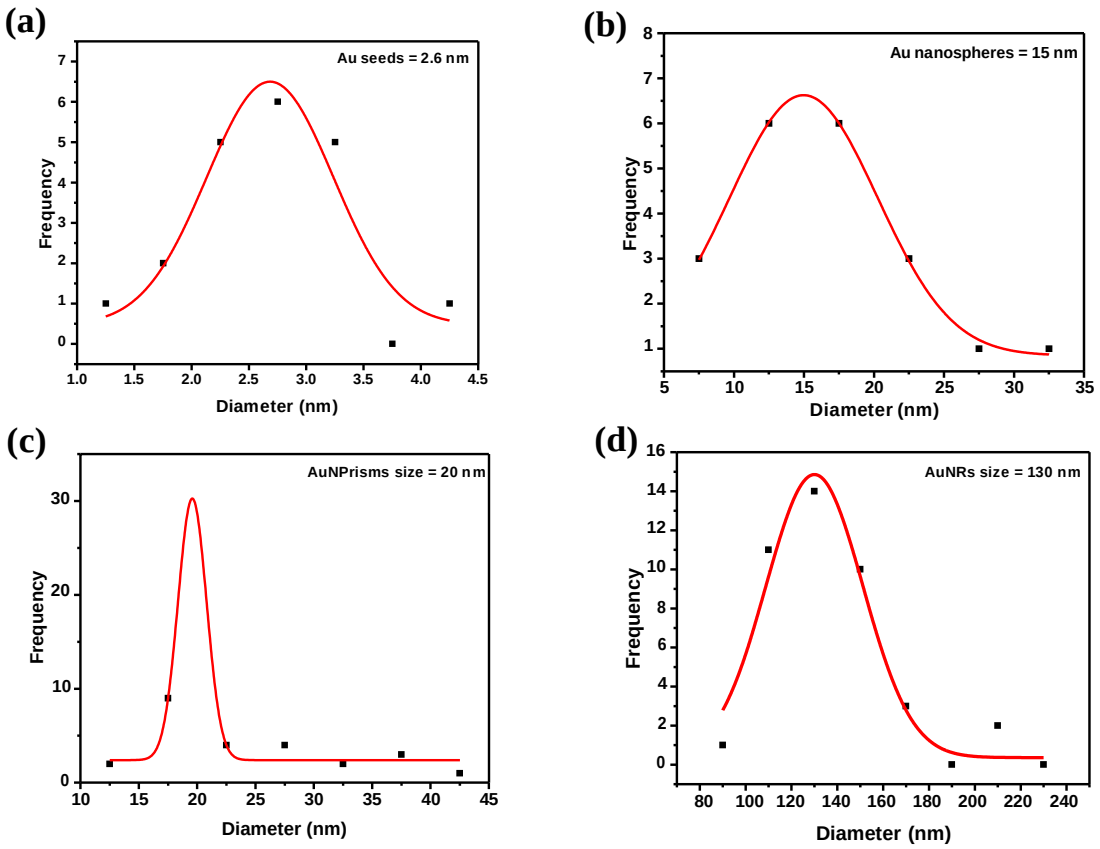

Figure 4.7. The Gaussian fit of the size distribution of (a) Au seeds, (b) Au nanospheres, (c) Au nanoprisms, and (d) Au nanorods.

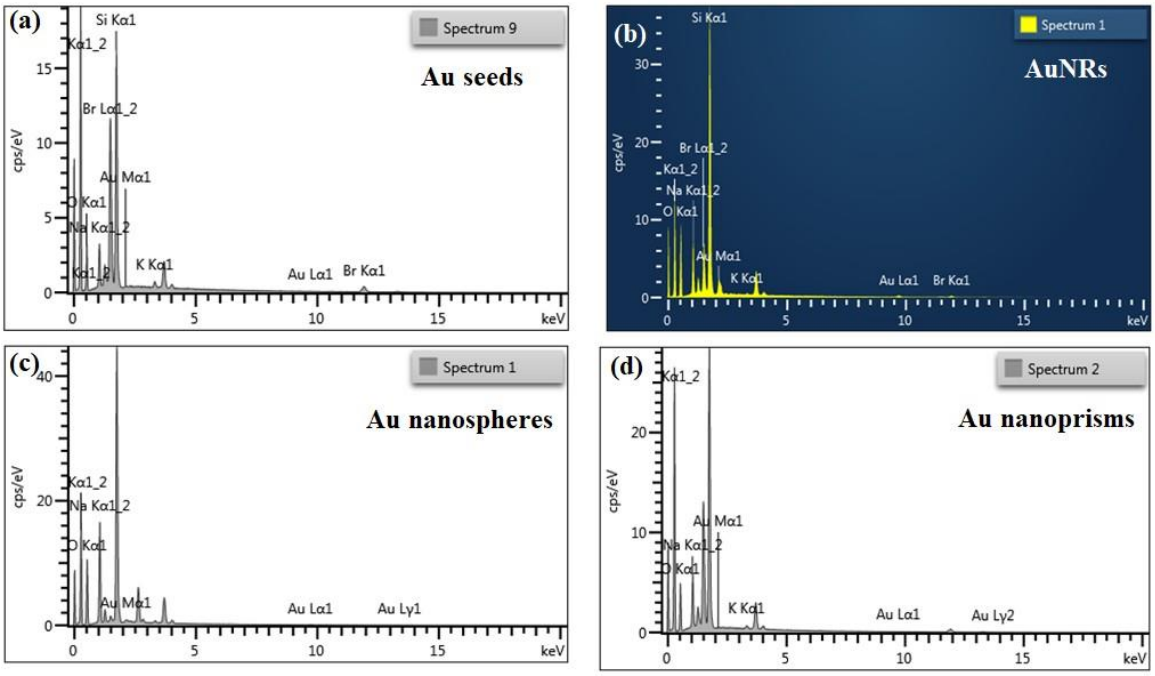

Figure 4. 8 EDS for (a) Au seeds, (b) Au nanorods, (c) Au nanospheres, and (d) Au nanoprisms.

4.2.3 Structural properties

4.2.3.1 Raman analysis

Raman peaks of Au nanostructures are presented in Figure 4.9. The synthesized nanostructures showed sharp and strong Raman vibrational modes. For AuNSs, the Raman peaks at 562, 781, 955, and 1097 cm^{-1} were obtained. The 1097 cm^{-1} was the most intense peak for that sample. Au nanoprisms showed peaks at 562, 782, 955, and 1097 cm^{-1}. The peak at 1097 cm^{-1} is more intense than that of Au nanospheres and this can be due to the increase of the size of the particles. Au seeds revealed peaks at 774, 948, 1072, 1137,1307, 1451, 1477, and 1607 cm^{-1}, AuNRs showed peaks at 773, 944, 1072, 1137, 1306, and 1583 cm^{-1}. The integrated surface-enhanced Raman signal (SERS) signal for each type of Raman sample shows that the maximum surface-enhanced Raman signal was obtained from samples of different shapes [5]. SERs occur when a nanoparticle exhibits a LSPR under electromagnetic wave irradiation. At the resonance frequency, the electrons of the nanoparticle start to oscillate generating an intense new localized electric field called near-field enhancement during an optical exposure, usually known as a confined or trapped electromagnetic field [6].

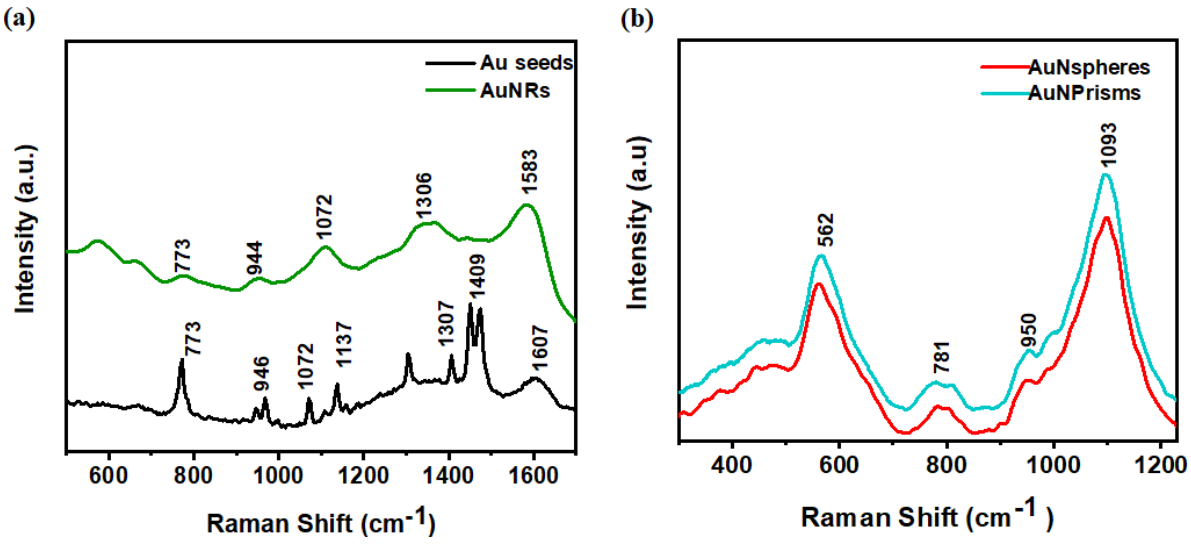

Figure 4.9. Raman spectra of (a) Au seeds and nanorods, (b) Au nanospheres and nanoprisms.

4.2.3.2 XRD analysis

Figure 4. *10* represents the XRD analysis of Au nanostructures. The XRD patterns for Au seeds and NSs revealed diffraction peaks at 37.3, 43.6, 63.9, and 76.9º 2-theta angles that correspond to (111), (200), (220), and (311) planes, respectively as shown in Figure 4. *10*. AuNRs showed peaks at 37.3, 43.6, 63.9, and 76.9º 2-theta angles, corresponding to (111), (200), (220), and (311) planes, respectively of Au according to JCPDS card #04-0784 [7]. These planes show the reflection planes of the face-centred-cubic (fcc) of Au. For Au nanoprisms, the peaks at 37.3, 43.6, 63.9 and 76.9º corresponding to (111), (200), (220), and (311) planes respectively, which belongs to face-centred-cubic (fcc) metallic Au structure (ICCD, PDF2 65-8601) [4] in Figure 4. *10*(b). The Au peaks at (111) and (200) are more intense than the other peaks and were used to calculate the crystallite sizes and lattice constants for both AuNRs and Au nanoprisms. The crystallite size and lattice constants were calculated using Debye-Scherrer equation 4. 1 while equation 4. 2 was used to calculate lattice constants [8].

$$D = \frac{K\,\lambda}{FWHM\ cos\,\theta} \qquad 4.\ 1$$

$$a = d\,(h^2 + k^2 + l^2)^{\frac{1}{2}} \qquad 4.\ 2$$

where D is the crystallite size, K is the dimensionless shape factor, λ is the X-ray wavelength, FWHM is the full width at half maximum, θ is Bragg's angle, a is the lattice constant, d is d-spacing and (hkl) is the miller indices. The results showed that the average crystallite size of Au seeds was 25.9 nm with a lattice constant of $a = b = c$ =3.8 Å and for AuNSs was 25.3 nm and lattice constant of $a = b = c$ =3.8 Å. For AuNRs, the average crystallite size was 14.4 nm with lattice constants $a = b = c$ = 4.15 Å and 11.4 nm was obtained for Au nanoprisms with lattice constants $a = b = c$ = 4.10 Å. In the same way, Ogundare *et al.* [8] discussed the crystallite size determination of thermally deposited AuNPs. The average crystallite size of AuNPs deposited on the glass slide was 14.4 nm with lattice constants: $a = b = c$ = 4.0789 Å.

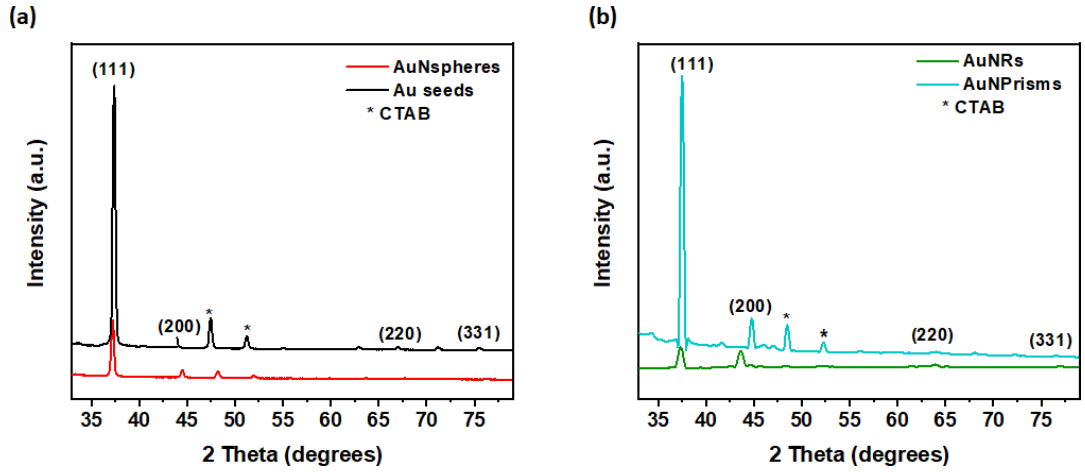

Figure 4. 10 XRD spectra of (a) Au nanospheres and seeds, (b) Au nanorods and nanoprisms.

4.3 Properties of PCDTBT: $PC_{70}BM$ layer with Au nanostructures.

In this section, the results from the preparation of PCDTBT: $PC_{70}BM$ thin films by a spin coating method and addition of Au nanospheres, nanorods, and nanoprisms by drop-casting are presented. The optical, morphological, and structural properties of PCDTBT: $PC_{70}BM$ thin films with and without Au nanostructures are discussed. UV-Vis showed the absorption maxima of the thin films at 378, 470, and 564 nm for all the samples at different intensities. Raman studies showed vibrational modes that confirmed that the polymer was dominant, and no crystalline domains were observed. From SEM images, the compact layer, well-dispersed particles, and the pin-holes defects were observed. EDS confirmed that Au nanospheres, nanorods, and nanoprisms were successfully added to the thin film PCDTBT: $PC_{70}BM$.

4.3.1 Optical properties

UV-Vis spectroscopy was used to measure the optical properties of PCDTBT: $PC_{70}BM$ thin films in the wavelength ranging from 300 to 800 nm to obtain absorbance. Figure 4.*11* shows the absorbance for the PCDTBT: $PC_{70}BM$ (1:4) layer that has different Au nanostructures. The spectra showed similar broad light absorption for all the samples. It was observed that the most intense absorption is in the ultra-violet region. However, the reference PCDTBT: $PC_{70}BM$ layer show three absorbance maxima at 378, 470, and 564 nm. The PCDTBT: $PC_{70}BM$ with AuNSs had the same intensity but different absorbance at 378, 470, and 567 nm. On the other hand, the layer with AuNRs had absorbance peaks at 380, 478, and 571 nm

with higher intensity compared to the reference and layer with AuNSs. The layer with Au nanoprisms showed high intensity than the other samples but the absorbance peaks (379, 473, and 560 nm) were similar.

The solar energy conversion efficiency depends on the steady-state absorption spectral properties of the PCDTBT: PCBM active layer [9]. Similar results have been reported by Song *et al.* on their UV-Vis absorption spectra of polymer blend (PCDTBT: PCBM) film with and without Au nanobumb structures. It was observed that films with Au nanobumb structures consistently absorb more light compared to films without, within 450 - 650 nm wavelength range [10]. For instance, He *et al.* [11] showed the UV-Vis absorption spectra of PCDTBT: PCBM blend films with AuNRs and it showed great optical absorption covering the wavelength range of 350 and 700 nm. Partly, attribute the enhanced optical absorption to LSPR and scattering effect of AuNRs. The low absorption for the active layer with AuNSs could be due to degradation taking place, according to Mohammadnezhad *et al*. [12].

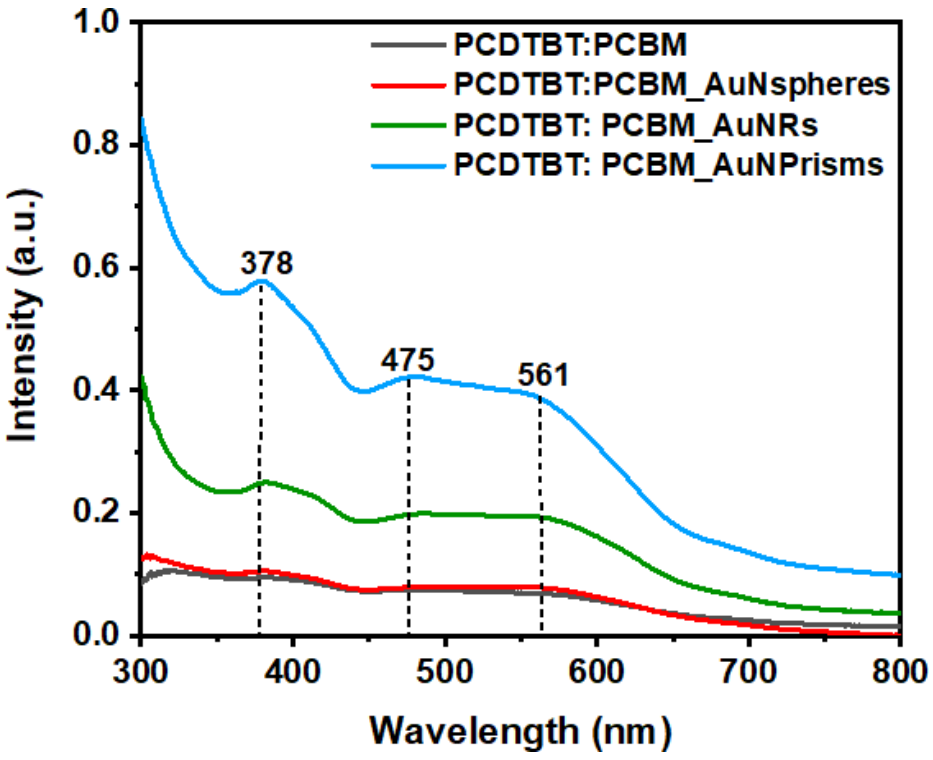

Figure 4.11. UV-Vis absorption spectra of active layer PCDTBT: $PC_{70}BM$ layer with incorporated Au nanostructures.

4.3.2 Structural properties

Figure 4.*12* presents Raman spectroscopy of PCDTBT: $PC_{70}BM$ active layer with Au nanostructures and the sample scan that ranged from 300 to 800 cm^{-1}. The spin-coated active layer thin films revealed sharp and strong vibrational modes. The vibrational modes of the samples were 573, 774,1102, 1376, 1447, and 1596 cm^{-1}. These prominent vibrational modes observed confirm that polymer vibrations are dominant. For instance, Fuchs *et al.* [13] reported similar Raman results of PCDTBT: PCBM with ratios of 1:1 and 1:4. The vibrational modes with the highest Raman intensities were observed at 1272, 1340 - 1390, and 1527 cm^{-1}. The assigned vibrations are considered the blend PCDTBT: PCBM, which is commonly used as the active layer.

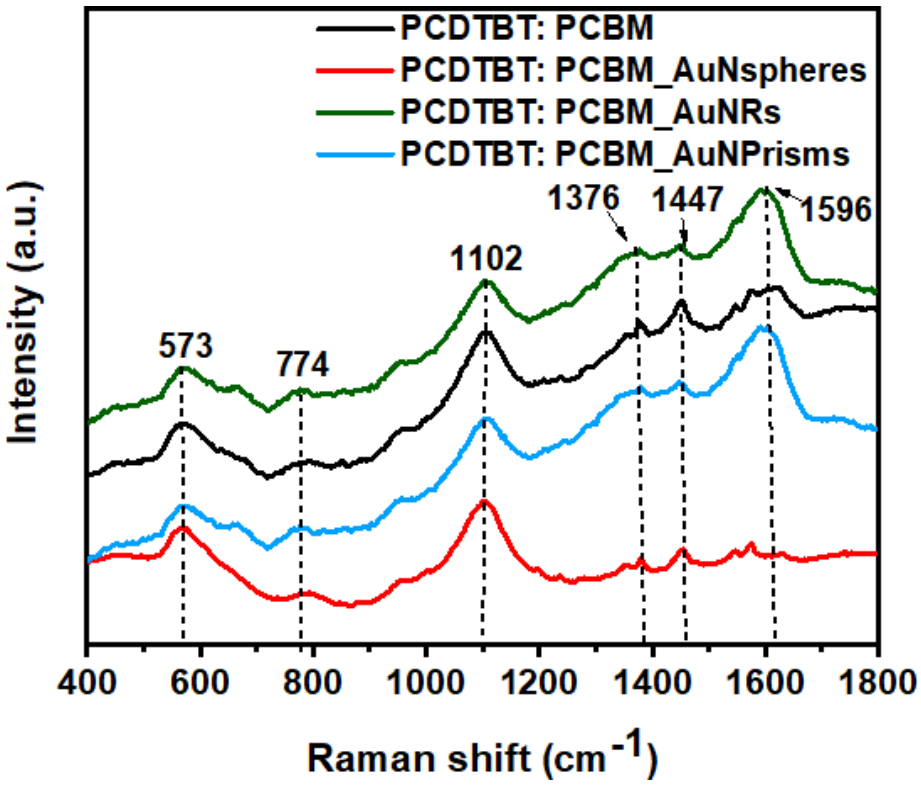

Figure 4.12. Raman spectra of PCDTBT: $PC_{70}BM$ active layer with Au nanostructures.

XRD was used to study the structure of the active layer with incorporated AuNSs with the 2θ angle that ranged from 25º to 70º, as shown in Figure 4.*13*. The XRD peaks for the PCDTBT: $PC_{70}BM$ with and without Au nanostructures were very small. The sample with only PCDTBT: $PC_{70}BM$ and layer with AuNRs showed the same peak at 27º. The XRD patterns

of a layer with AuNSs had peaks at 29, 38, 43, 47, 52, and 57º Similar peaks were observed for the layer with Au nanoprisms at 30, 34, 37, 38, 45, and 50º. These two samples had two diffraction peaks at 38º and 43º that indicates the presence of Au. The XRD results show that no crystalline domains were present in the PCDTBT: $PC_{70}BM$ active layer, indicating that the layers may have been amorphous [14]. Similar results were reported by Huh *et al*. The XRD peaks of PCDTBT: PCBM layers showed only broader patterns between 12º and 40º, which indicate no crystalline structures [15].

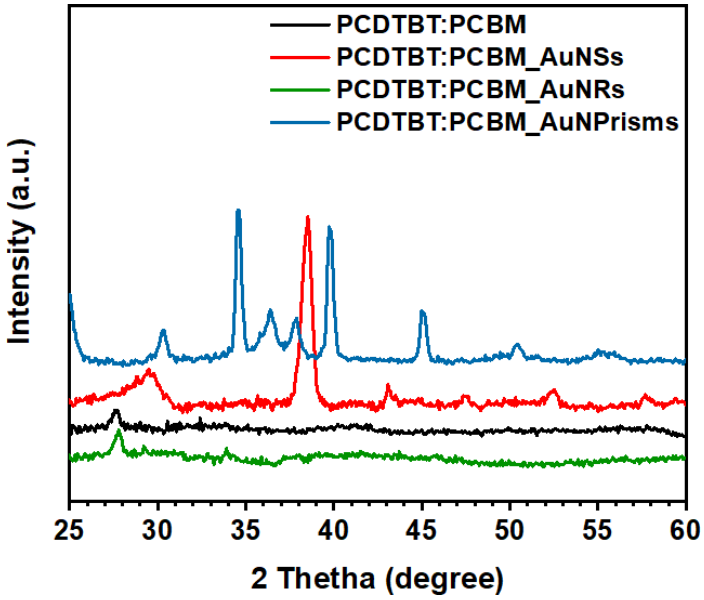

Figure 4.13. XRD spectra of PCDTBT: $PC_{70}BM$ with and without Au nanostructures.

4.3.3 Surface morphology

The morphology of PCDTBT: $PC_{70}BM$ with and without Au nanostructures is presented in Figure 4.*14*. There was an increase in grain size with the variations of shapes from an active layer without nanostructures to an active layer with AuNRs. The active layer is compact, and the particles are very well dispersed. The reference PCDTBT: $PC_{70}BM$ layer had good morphology and compact particles with a grain size of 17.28 nm. Also, there were pinholes defects observed on the PCDTBT: $PC_{70}BM$ layer. For PCDTBT: $PC_{70}BM$ with AuNSs, the morphology was similar to the reference active layer and the obtained grain size was 15.86 nm. In the same way, the layer with AuNRs and Au nanoprisms had grain sizes of 34.51 and 20.23 nm, respectively. Figure 4.*15* shows the Gaussian fit for the active layer with and without AuNSs, NRs, and nanoprisms. From the fitting, the distribution increased as the layer

with AuNRs revealed the highest diameter. To confirm the incorporation of Au nanostructures in the active layer, the energy-dispersive X-ray spectroscopy (EDS) shown in Figure 4.*16* was used. All the spectrums showed Au peaks which confirmed that Au nanostructures were successfully added to the active layer.

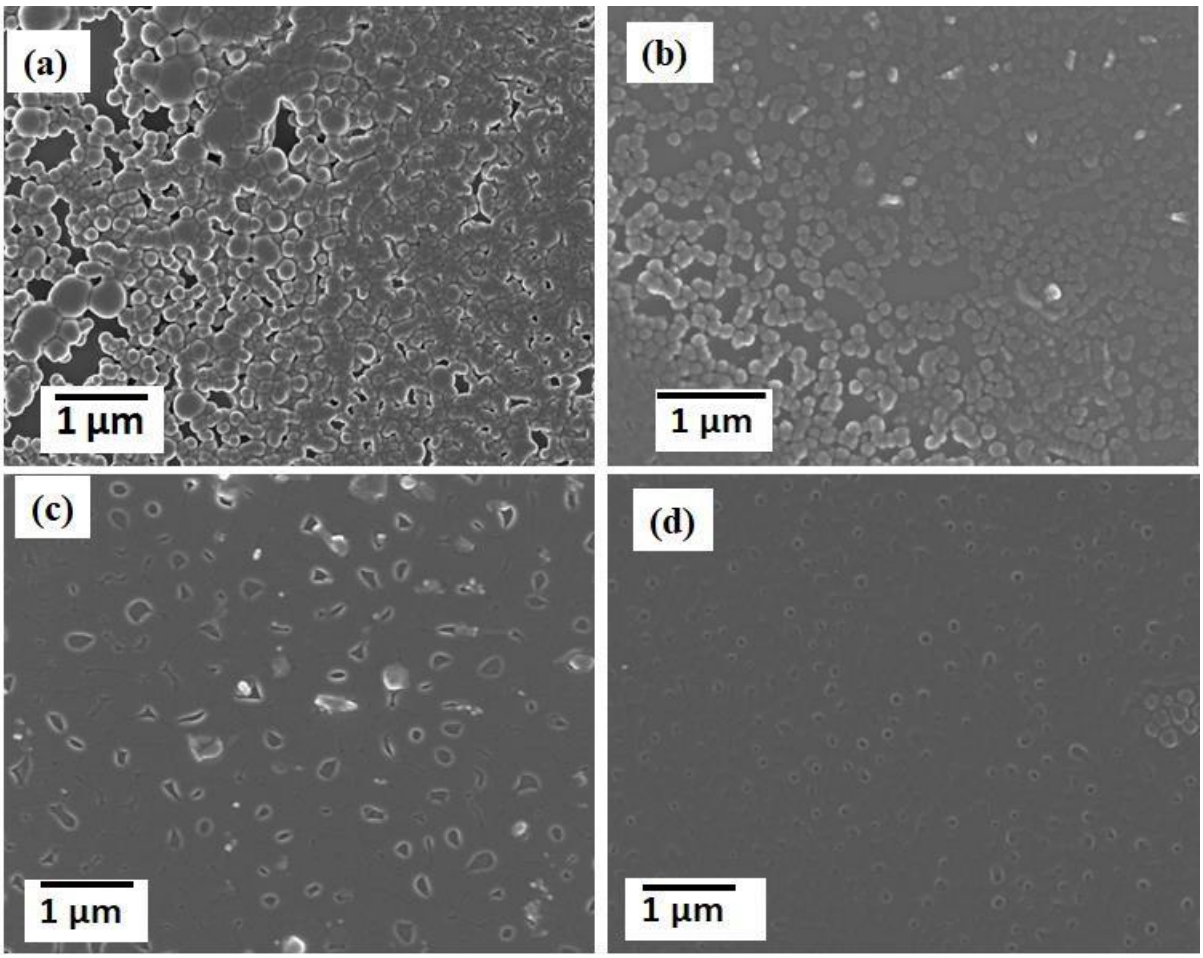

Figure 4.14. The SEM images of PCDTBT: $PC_{70}BM$ with (a) without nanostructures, (b) Au nanospheres, (c) Au nanorods, and (d) Au nanoprisms.

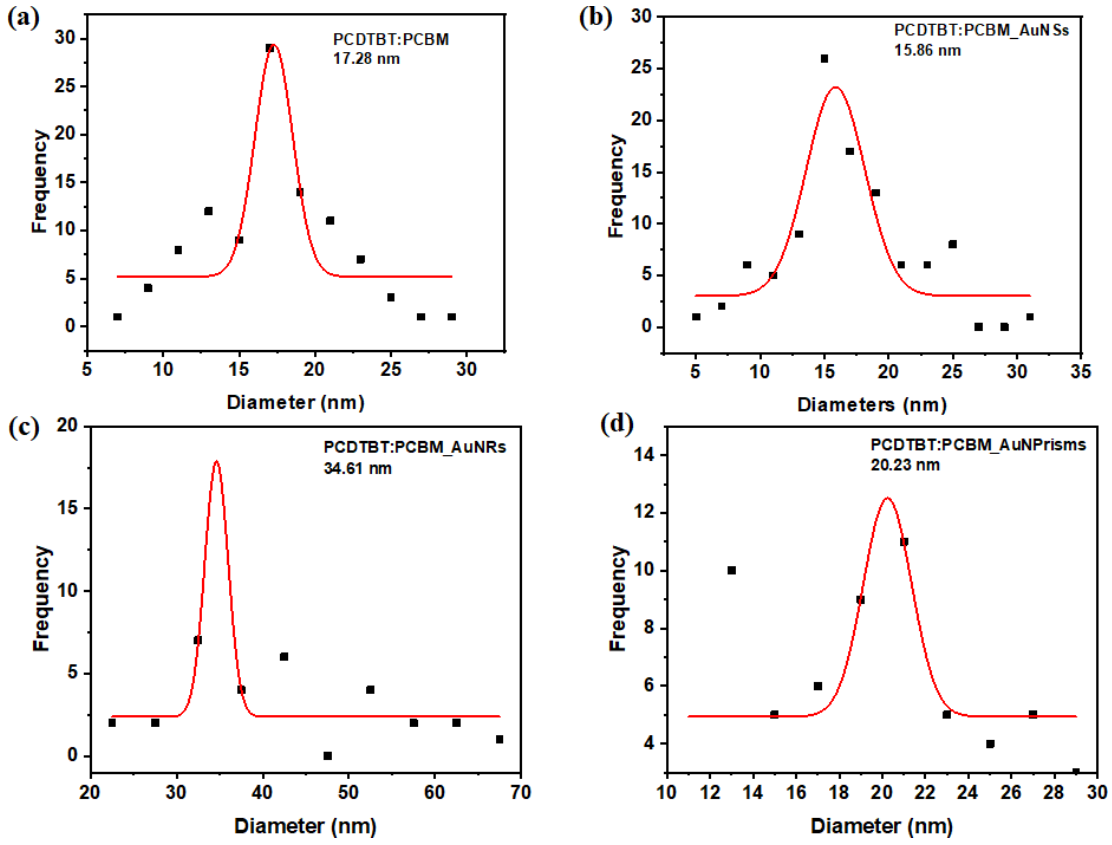

Figure 4.15. The Gaussian fit for PCDTBT: $PC_{70}BM$ size distribution with (a) no nanostructure, (b) Au nanospheres, (c) Au nanorods, and (d) Au nanoprisms.

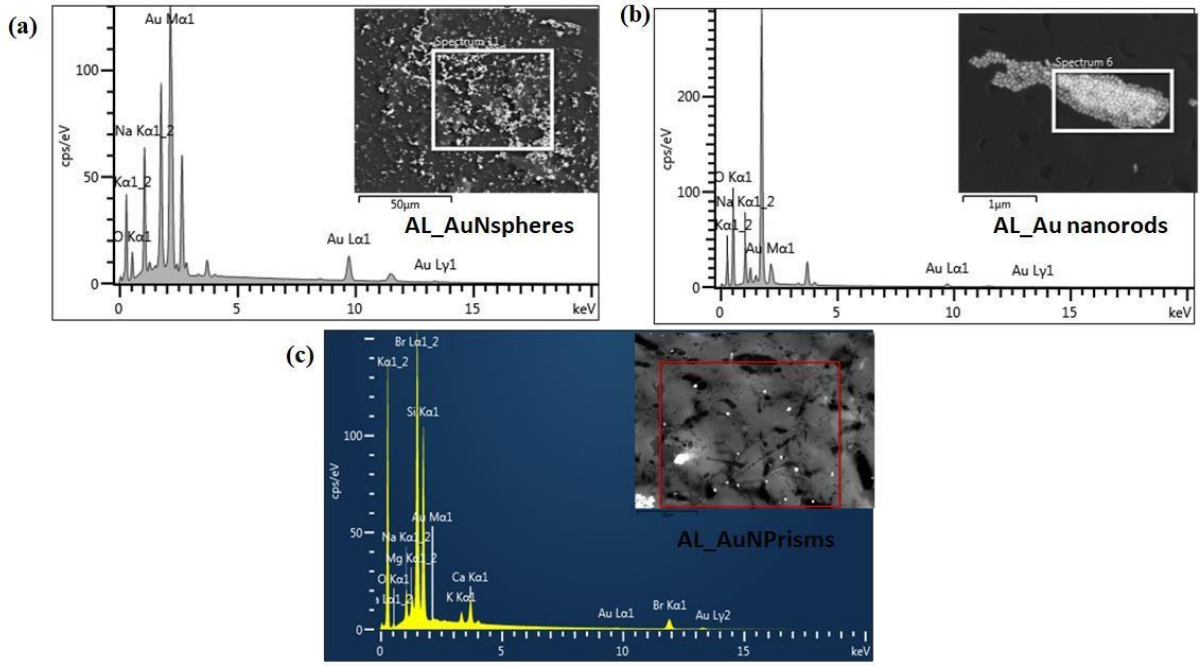

Figure 4.16. The EDS for active layer (AL) PCDTBT: $PC_{70}BM$ with (a) Au nanospheres (b) Au nanorods and (c) Au nanoprisms.

4.4 Structural, optical, and morphological properties of TiO_2 electron transport layer.

The results from the preparation of TiO_2 thin films by the spin coating method are discussed in this section. The optical, structural, and morphological properties are presented. XRD confirmed the tetragonal crystal structure and anatase phase of TiO_2 by showing 2θ peaks at 25, 37, 51, 61,70, and 78º. Similarly, Raman spectroscopy showed four characteristics with symmetries at E_g, B_{1g}, A_{1g}, and E_g and these active modes confirmed the anatase TiO_2 phase. UV-Vis absorption maxima at 313 nm were observed. From SEM images the thin film surface was uniformly distributed and compact, the calculated average grain size was 14.61 nm.

4.4.1 Structural properties

XRD was used to confirm the crystal structure of TiO_2 thin films. Figure 4.17 shows the XRD pattern of the TiO_2 layer on fluorine-doped tin oxide (FTO) substrates. All the phases of TiO_2 were confirmed with the correct indexing in their 2θ angles. The diffraction peaks at 25.1, 37.7, 51.6, 61.5, 70.7 and 78.2º corresponding to (101), (004), (200), (105), (204), (220) and (301) planes, respectively. These planes confirm the anatase TiO_2 phase according to JCPDS card no. 21-1272. From Figure 4.*17*, peak (101) was used to calculate the crystallite size by the Debye-Scherrer formula, and the lattice parameters were obtained. The results showed that the average crystallite size is 22.85 nm, and the lattice parameters are $a = b = 3.769$ Å and $c = 9.429$ Å, which confirms the tetragonal crystal structure of TiO_2. These results are similar to those reported in the literature. Ba-Abbad *et al.* [16] reported the XRD spectra of TiO_2 with a weak diffraction peak at 26.48º, which corresponds to the (101) plane of anatase phase according to JCPDS no. 21-1272. In the same way, Theivasanthi *et al.* reported that the experimental XRD pattern agrees with the JCPDS no. 21-1272, and the strong diffraction peaks at 25º and 48º indicate the TiO_2 anatase phase [17]. Another study by Challagula *et al.* reported the formation of pure phase tetragonal anatase TiO_2. For the (101) plane, the crystallite size was 15.0 nm, and the lattice parameters were obtained to be $a = b = 3.7794$ Å and $c = 9.4984$ Å [18].

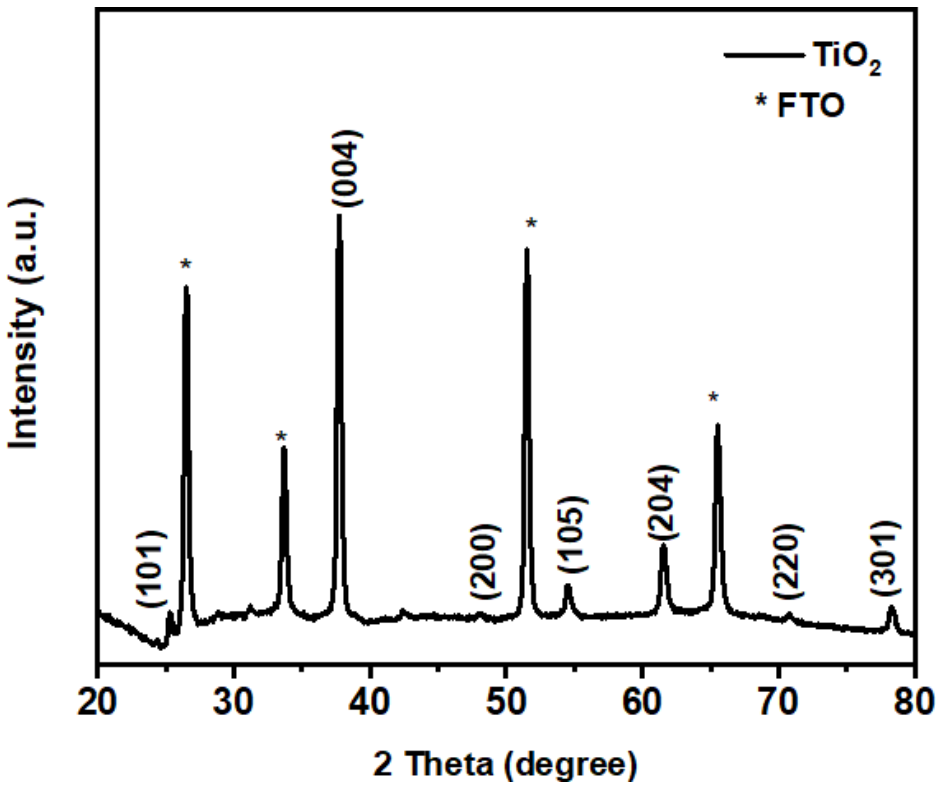

Figure 4.17. X-ray diffraction patterns of TiO_2.

Raman spectroscopy was used to confirm the crystal structure of TiO_2 thin films. Figure 4.*18*. Raman spectrum of TiO_2. reveals the structural information from Raman spectra. Four characteristics of Raman active modes with symmetries E_g, B_{1g}, $A_{1g,}$ and E_g were observed at 153, 406, 525, and 648 cm^{-1}, respectively. These characteristics vibrational frequencies and their intensity ratios confirmed the anatase TiO_2 phase [19]. Challagulla *et al.* reported structural information for the TiO_2 anatase phase at 134, 382, 500, and 618, which corresponds to E_g, B_{1g}, $A_{1g,}$ and E_g vibrational modes, respectively [18]. Similarly, Frank *et al.* reported the Raman spectra of anatase TiO_2 with corresponding isotopes mutations ($Ti^{16}O_2$, $Ti^{17}O_2$, $Ti^{18}O_2$) measured at 295 K and 5 K. The Raman active modes E_g (1), E_g (2), B_{1g} (1), B_{1g} (2) + A_{1g} and E_g (3) were observed [20].

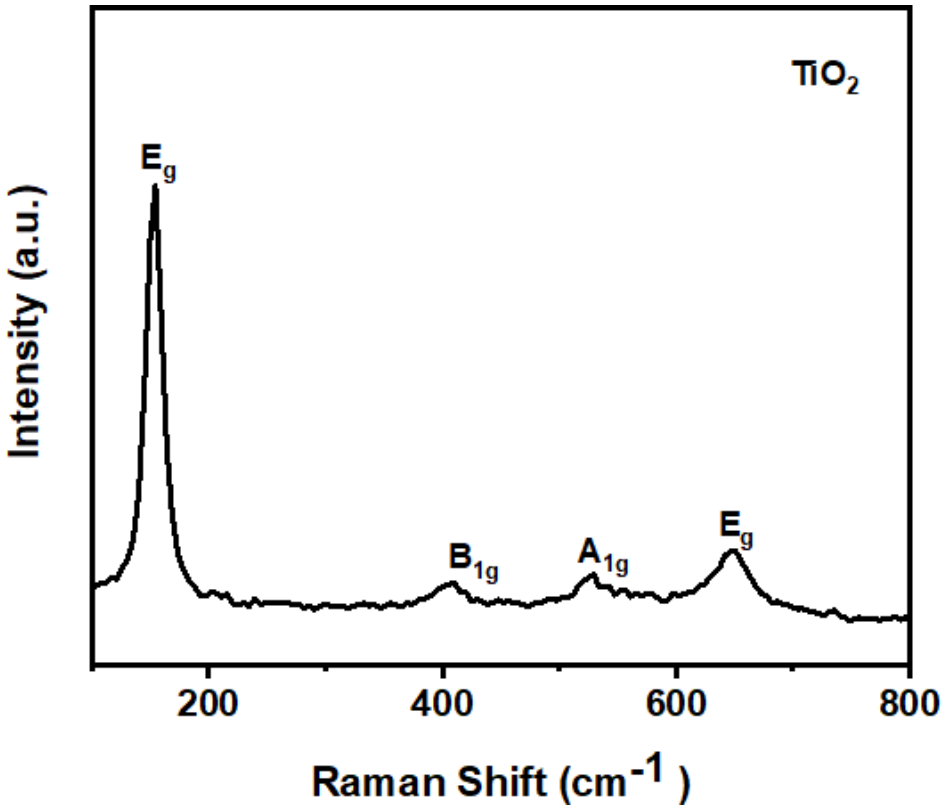

Figure 4.18. Raman spectrum of TiO_2.

4.4.2 Optical properties

UV-Vis spectroscopy was used to measure the absorbance of TiO_2 thin films prepared by the spin coating method. There was a relatively highest absorbance of this film in the ultraviolet region, hence it is used as the electron transport layer (ETL). Figure 4.19 present the absorption maxima at 313 nm for anatase TiO_2. There was only one absorption peak that confirms the absorbance of the anatase TiO_2 phase. This is similar to the results obtained by Al-Oubidy *et al.* who reported the absorption spectrum of TiO_2 which showed moderate absorption wavelengths shorter than 300 nm to reach its maximum at 310 nm. The absorbance rapidly dropped to reach its minimum at 400 nm [21].

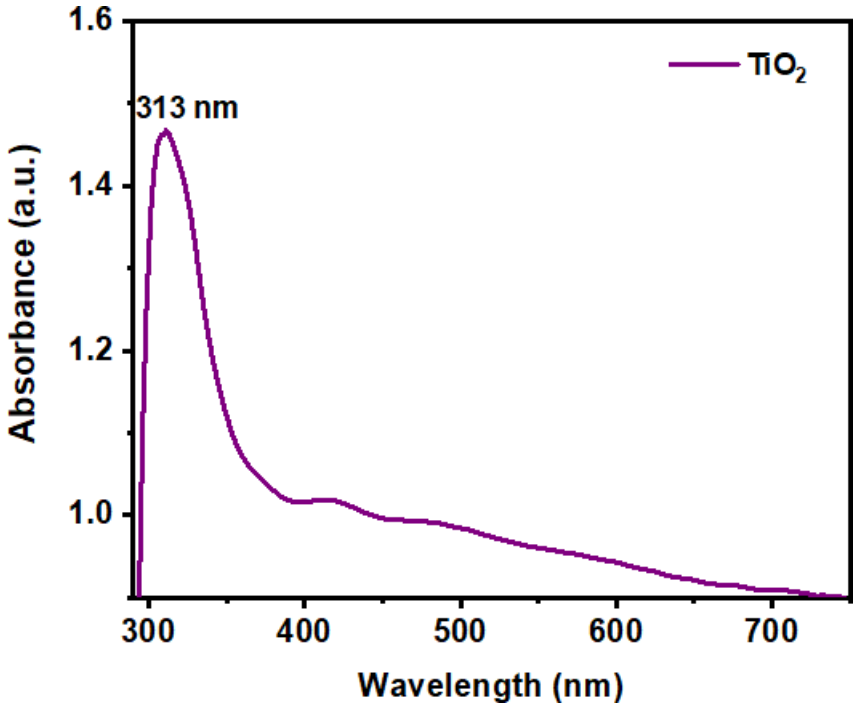

Figure 4.19. UV-Vis spectrum of TiO_2.

4.4.3. Surface morphology

The surface morphology and grain size of the prepared thin film were obtained by scanning electron microscopy (SEM). Figure 4.*20*(a) presents the SEM image of anatase TiO_2 which indicates that the particles are uniformly distributed, crack-free, homogenous in size, and small. The average particle size was 14.61 nm. A study by Al-Oubidy *et al.* reported results of TiO_2 SEM images with good morphology and average particle size ranging from 5 - 7 nm [21]. A typical cross-section SEM image of TiO_2 ETL is presented in Figure 4.*20*(b). The thickness measured was 500 nm. The TiO_2 film has a very well-defined column, structure in its entire thickness. Another study conducted by Parreira *et al.* reported the SEM results of TiO_2 with a thickness of 2 μm and it was evident that the thin film has a well-defined structure and thickness [22].

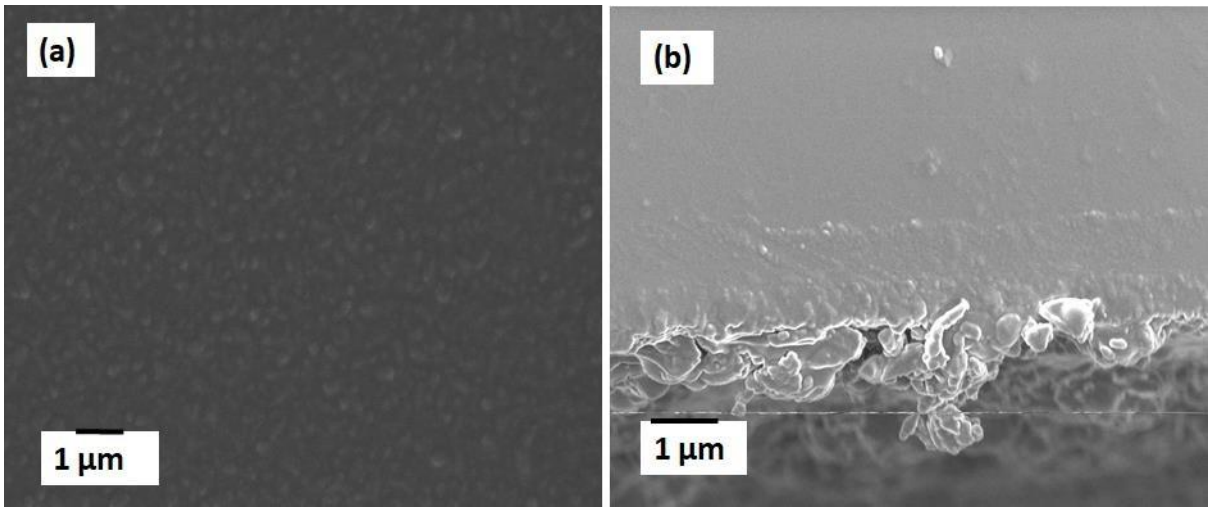

Figure 4.20. SEM images of TiO_2 thin film (a) top view and (b) cross-section.

4.5 Structural, optical, and morphological properties of PEDOT: PSS hole transport layer.

The results from the preparation of PEDOT: PSS thin films by spin coating method were obtained and discussed in this section. It presents the structural, optical, and morphological properties of PEDOT: PSS thin film. The UV-Vis spectroscopy showed an absorption peak at 310 nm. Raman spectroscopy revealed strong vibrational peaks at 1254, 1443, 1508, and 1570 cm^{-1}. SEM images showed good morphology. From XRD no diffraction peaks were observed due to the amorphous nature of PEDOT: PSS.

UV-Vis spectroscopy was used to measure the optical absorption of the spectrum of PEDOT: PSS in the wavelength range of 300 to 800 nm. Figure 4. *21*(a) shows the absorption spectrum of PEDOT: PSS thin film within the UV-Visible range. A peak in absorbance was observed at 310 nm. The PEDOT: PSS film has negligible absorbance as clear from where the light was observed. A study by Mustafa *et al*. reported similar UV-Vis spectra with no clear absorption of PEDOT: PSS [23]. In the same way, the optical property of the PEDOT: PSS peak is in the wavelength area of ~300 nm as Susanti *et al.* reported [24].

Raman spectroscopy was used to analyze the structural properties of PEDOT: PSS [25]. Figure 4. *21*(b) presents the Raman spectroscopy of PEDOT: PSS thin films with the sample scan that ranged from 1000 and 1800 cm^{-1}. The vibrational peaks at 1254, 1443, 1508, and 1570 cm^{-1} modes were observed. These vibrational peaks attribute to C_α-C_α' inter-ring stretching vibration, $C_\alpha = C_\beta$ symmetric stretching vibration, and asymmetrical stretching vibration [25]. A study by Xiong *et al.* reported Raman spectra of PEDOT: PSS films. The

major characteristic peaks of PEDOT: PSS were observed between 1200 and 1600 cm^{-1}. The three principal peaks obtained are 1265, 1444, and 1506 cm^{-1} [26].

Figure 4. *21*(c) presents the surface morphology of PEDOT: PSS thin film which was obtained by using SEM. The morphology was homogenous, and the nanoparticles observed were well dispersed. Susanti *et al.* reported the morphology of PEDOT: PSS with a good surface [24]. Figure 4. *21*(d) represents the XRD pattern for PEDOT: PSS. There were no diffraction peaks observed for ETL PEDOT: PSS polymer due to the amorphous nature [27]. Sayyad *et al.* reported the XRD diffraction pattern of PEDOT: PSS with and without doping. In the XRD spectra, PEDOT: PSS without doping had no diffraction peaks compared to a layer with doping [28].

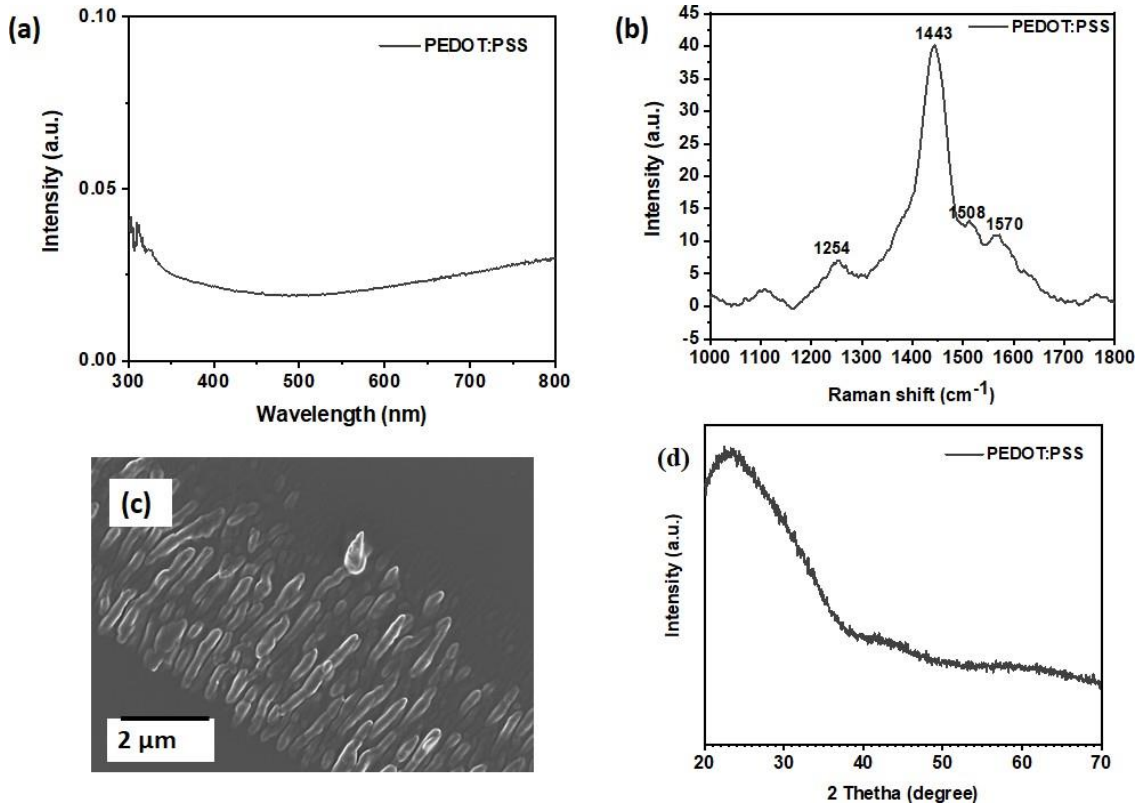

Figure 4. 21. The properties of PEDOT: PSS thin film (a) UV-Vis spectra, (b) Raman spectra, (c) SEM image, and (d) XRD pattern.

4.6 Electrical properties of PCDTBT: PCBM organic solar cells

From the previous sections, all the layers were used to fabricate organic solar cells (OSCs). TiO_2 was used as an ETL (500 nm), PCDTBT: PCBM active layer with approximately 70 nm thickness, PEDOT: PSS as the HTL (62 nm), and 80 nm silver (Ag) contacts as back contacts. Figure 4.*22* present the schematic diagram of the OSCs devices, pristine (without nanostructures), and plasmonic devices.

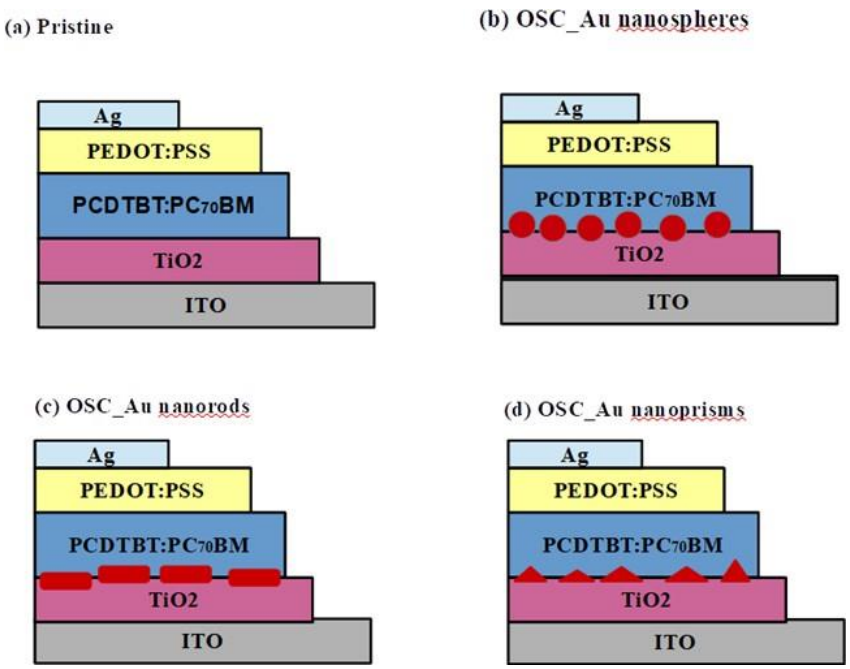

Figure 4.22 Schematic diagrams of fabricated OSCs (a) reference, with (b) Au nanospheres, (c) Au nanorods, and (d) Au nanoprisms.

In this section, the results of the fabricated PDCTBT: $PC_{70}BM$ with and without Au nanostructures by spin coating method are reported. The electrical properties of pristine OSCs and plasmonic devices are discussed. The pristine devices had an efficiency of 2.04% immediately after fabrication which was higher compared to plasmonic devices with 1.19, 0.92, and 0.32% for the device with AuNSs, AuNRs, and Au nanoprisms, respectively. After a month, the efficiency of the pristine and device with AuNSs increased to 2.80 and 1.72%, respectively. The plasmonic device with AuNSs showed an LSPR effect due to the slight increase in current density, even though the efficiency is still lower than the pristine. While the device with AuNRs and Au nanoprisms decreased to 0.83 and 0.23%, respectively. It was

also observed that the change of pixel area from 0.010 to 0.001 cm^2 in the I-V solar system causes the performance to be enhanced drastically.

4.6.1 Electrical properties

Figure 4.*23* shows current density (J-V) characteristics of the fabricated ITO/TiO_2/PCDTBT: $PC_{70}BM$/PEDOT: PSS/Ag organic solar cells with and without Au nanostructures under illumination with 100 mW cm^{-2}. The device parameters such as short-circuit current (J_{sc}), open-circuit voltage (V_{oc}), fill factor (FF) and power conversion efficiency (PCE) are summarized in Table 4.*1*. These parameters are defined by the equation 4. 3 , where P_{in} is the power density of the incident light source [29].

$$PCE = \frac{V_{oc} \, . J_{sc} \, . FF}{P_{in}} \qquad 4.\ 3$$

In the pristine device, a PCE of 2.04% was obtained with a J_{sc} of 12 mA/cm^2, V_{oc} of 0.48 V, and FF of 33.83%. Au nanostructures were incorporated between the TiO_2 (ETL) and PCDTBT: $PC_{70}BM$ active layer. The devices with AuNSs (6 nm) and AuNRs (70 × 40 nm) showed PCE of 1.19% (J_{sc} = 13.27 mA/cm^2, FF = 29.20% and V_{oc} = 0.27 V) and 0.92% (J_{sc} = 11.90 mA/cm^2, FF = 28.26% and V_{oc} = 0.51 V), respectively. The values of PCE, J_{sc}, V_{oc}, and FF all decreased compared to the pristine device. The device with Au nanoprisms (68 nm) had a PCE of 0.32% was the lowest efficiency, and a significant decrease in J_{sc} of 1.47 mA/cm^2 was observed, compared to the other devices. Meanwhile, an increase in FF and V_{oc} with values of 42.79% and 0.51 V, respectively was observed.

The low V_{oc} may be attributed to the increase in carrier recombination at the interface of the active layer and nanostructured layer [30]. Song *et al.* obtained the PCE of OSCs containing NPs (nanospheres- 5 nm: 3.30% and nanospheres-10 nm: 4.70%) which decreased compared to the OSCs without NPs. This low PCE was attributed to the decrease in FF and V_{oc} without any enhancement in J_{sc} [10]. In the same way, Olieslaeger *et al.* reported that annealing the PCDTBT: PCBM active layer at 160ºC for 4 min resulted in a decrease in V_{oc} and FF [31]. Similar effects have also been reported by Gusian *et al.* that annealing PCDTBT: PCBM active layer at 180ºC for 4 min showed low PCE possibly due to the low V_{oc} and FF in the NPs device [32]. In this study, the PCDTBT: $PC_{70}BM$ layer was on top of TiO_2. The low

parameters of our devices could be due to the annealing of the spin coated PEDOT: PSS layer at 150ºC for 15 min.

Qiao *et al.* reported that according to their simulation results, the AuNPs localized surface plasmon resonance (LSPR) effect can enhance their surrounding electromagnetic fields, which could increase the absorption ability of the active layer around them and increase the probability of exciton generation and dissociation. An increase of Au nanostructure doped devices is supposed to prove this [33]. One of the possible assumptions is the increased series resistance and recombination process involved in the active layer regarding the decrease in energy conversion efficiencies [34]. Namkoong *et al.* reported PCDTBT: PCBM OSCs with different active layer thicknesses from 70 to 150 nm. The energy conversion efficiencies were ranging from 6.5 to 4.7% which is attributed to the recombination processes with different thicknesses of the active layer. They observed that PCDTBT: PCBM based OSCs with increased thickness has decreased efficiencies [35]. The crucial effect of reduced efficiency in OSCs is the non-radiative recombination in a material which leads to energy loss, limited carrier mobility, and light absorption [36]. In this study, as observed in Figure 4.*1* the absorption intensity is significantly low, and this may be the reason for the decreased efficiency of the devices. In addition, the low absorption in the near infrared region the spectrum of the active layer which leads to incomplete light harvesting according to Spyropoulos et al. could be the reason of limited efficiencies of the devices [37]. Therefore, the results of plasmonic devices measured after fabrication showed no plasmonic enhancement.

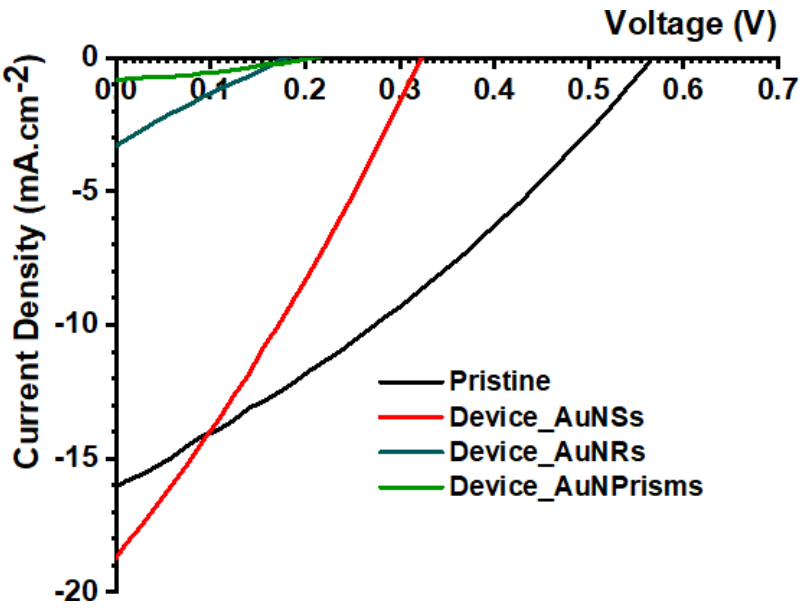

Figure 4.23. Current-density characteristics of devices with and without Au nanostructures under illumination.

Table 4.1 Comparison of performance of OPV devices with/ without Au nanostructures under illumination.

Device	**PCE (%)**	**FF (%)**	**J_{sc} (mA/cm^2)**	**V_{oc} (V)**
Pristine	2.04	33.83	12.57	0.48
Device_AuNSs	1.19	29.20	13.72	0.29
Device_AuNRs	0.92	28.26	11.90	0.27
Device_AuNPrisms	0.32	42.79	1.47	0.51

4.6.2 Electrical properties for devices after a month of fabrication

It was observed that the solar cell parameters changed when the J-V results were measured after a month of fabrication of the same sample devices. Figure 4.*24* presents the J-V characteristics curves for the fabricated device under illumination. Table 4.*2* shows the summarized solar cell parameters. These results are compared to the results measured after fabrication in section 4.4.1. The pristine and device with AuNSs have improved PCE values from 2.04%, 1.19% to 2.80%,1.72%, respectively. An increase of these parameters: J_{sc} of 16.06 and 18.74 mA/cm^2, and V_{oc} of 0.56 and 0.32 V for the pristine and device with AuNSs, respectively was observed. Meanwhile, the FF decreased for both devices with values of 30.77% (pristine) and 28.54% (a device with AuNSs). It is thus observed that for the 6 nm-

AuNSs device the J_{sc}, V_{oc}, and PCE increased compared to the results in section 4.4.1, indicating a slight increase in light absorption of this device according to Qiao *et al.* [33].

Similarly, the results obtained by Wang *et al.* showed an increase in J_{sc} from 10.79 mA/cm^2 to 11.61 mA/cm^2 and FF from 0.68 to 0.69% in a BHJ device with Ag clusters compared to the pristine. This resulted in their improvement of the efficiency of the device from 6.3% to 7.0% [38]. In the same way, Wu *et al.* reported an increase in J_{sc} for a device where silver nanotriangle (Ag-NTs) were integrated. They explained that the parameter J_{sc} is dependent on the generation and dissociation of excitons at the donor-acceptor interfaces and the charge collection at the electrodes [39]. However, in this study, the lower PCE of the device with AuNSs compared to pristine could be due to the decrease in FF. According to Wang *et al.* [38], J_{sc} and FF are critical factors to increase the efficiency of the device.

On the other hand, the devices with AuNRs and Au nanoprisms showed a decrease in PCE with values from 0.92%, 0.32% to 0.83%, 0.23%, respectively compared to the results measured after fabrication. The device with AuNRs had FF of 21.12%, J_{sc} of 8.28 mA/cm^2, and V_{oc} of 0.47 V. It was observed that FF and J_{sc} decreased, while there was an increase in V_{oc}. The device with Au nanoprisms showed a decrease in FF of 41.32%, J_{sc} of 1.09 mA/cm^2, and V_{oc} of 0.50 V. The decrease of PCE of these devices may be due to the low J_{sc}, FF, and V_{oc}. Murugesan *et al.* reported that a decrease in J_{sc} and FF values results in low PCE due to high series resistance (R_s) [9]. Similarly, Street *et al.* mentioned that the R_s have a significant influence on solar cell devices and reduce the FF and J_{sc} [40]. This could be the same reason both devices recorded a lower efficiency compared to the pristine measured after a month, hence no plasmonic enhancement was observed. Another study by Moon *et al.* observed that when the PCDTBT: PCBM active layer thickness was increased from 70 to 200 nm, the FF decreased significantly from 0.69 to 0.53%. Also, Moon *et al.* mentioned that the drop in FF could be due to an increase in carrier recombination which then limits the solar cell performance [41].

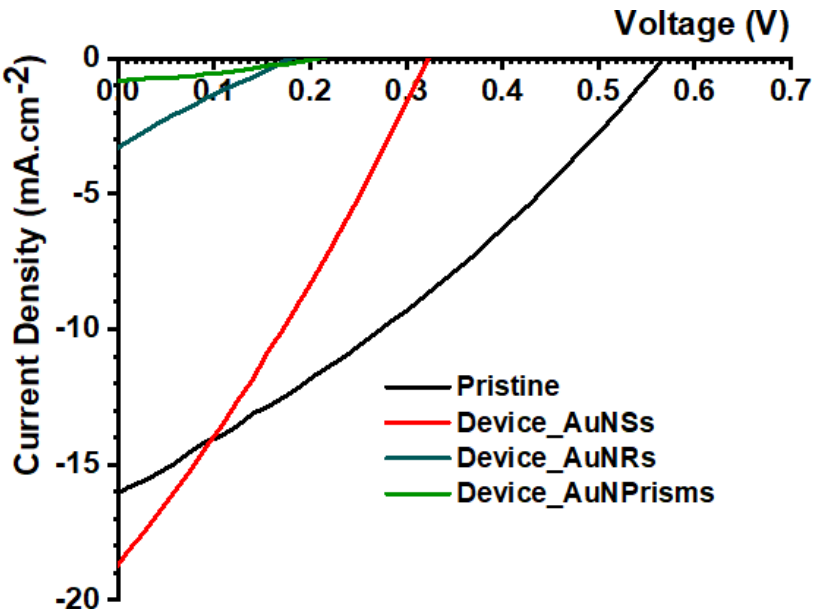

Figure 4.24. J-V characteristics of devices with/without Au nanostructures under illumination after a month.

Table 4.2 Comparison of performance of OPV devices with/ without Au nanostructures under illumination after a month.

Device	**PCE (%)**	**FF (%)**	**J_{sc} (mA/cm^2)**	**V_{oc} (V)**
Pristine	2.80	30.77	16.06	0.56
Device_AuNSs	1.72	28.54	18.74	0.32
Device_AuNRs	0.83	21.12	8.28	0.47
Device_AuNPrisms	0.23	41.32	1.09	0.50

4.6.3 Electrical properties for devices measured with pixel area of 0.001 cm^2

The I-V solar system from Ossila has been used to measure the J-V characteristics. When the pixel area was changed from 0.010 to 0.001 cm^2, the parameters of the solar cell of the same samples changed drastically. Figure 4.*25* present the J-V characteristics curve of the solar cell devices and Table 4.*3* summarized the device parameters when the pixel area was changed. The pristine device exhibited a PCE of 12.06% with FF of 39.28%, J_{sc} of 47.95 mA/cm^{2,} and V_{oc} of 0.64 V. For the device with AuNSs, a PCE of 0.017% was obtained with 7.31 % FF, 24.43 mA/cm^{2,} and a V_{oc} of 0.009 V. The device with AuNRs showed a PCE of 5.07%, FF of 29.25%, and J_{sc} of 36.03 mA/cm^2 and V_{oc} of 0.48 V. Lastly, the device with Au nanoprisms

showed PCE of 5.02%, FF of 37.81%, J_{sc} of 50.80 mA/cm^2 and V_{oc} of 0.26 V. It was seen that the efficiency, J_{sc}, V_{oc} and FF of the pristine, devices with AuNRs and Au nanoprisms increased significantly. In this case, a light absorption increase was observed. Meanwhile, for the device with AuNSs, all the parameters decreased. From Figure 4.*25*, the red graph shows the decrease of these parameters, and it is more of a straight line than curves like the other samples. This could be due to the change in the pixel area and that AuNSs is less stable compared to the other nanostructures according to Crammer *et al.* [2]. Also, this behavior could be from possible low-intensity absorption of the PCDTBT: $PC_{70}BM$_AuNSs in Figure 4.*1*. The sudden increase in the solar cell's parameters may be due to the change in the pixel area and it shows that it influences the I-V characteristics.

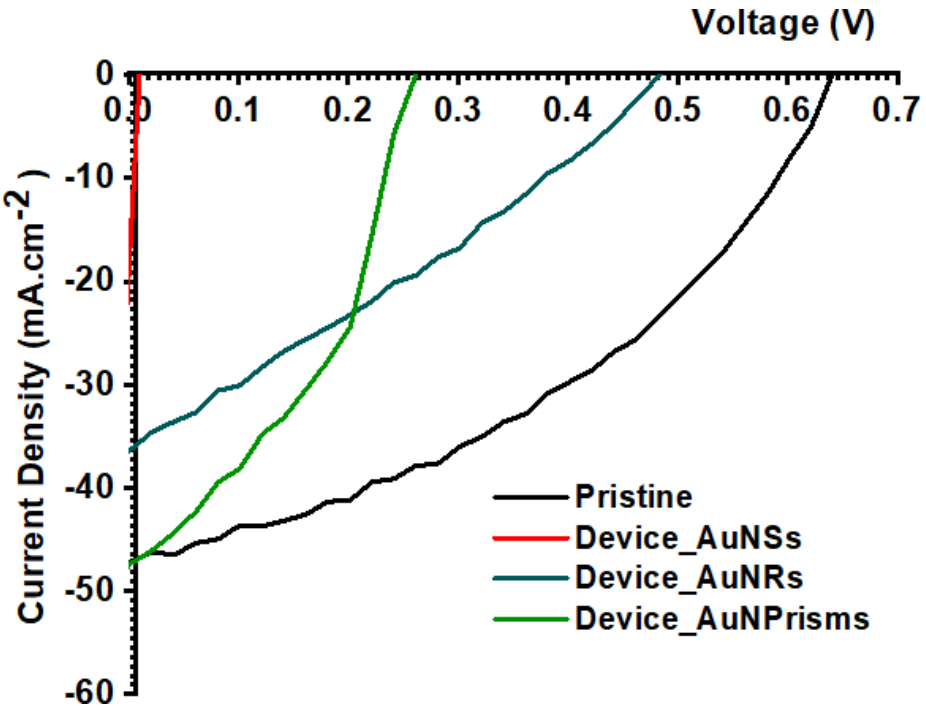

Figure 4.25 J-V characteristics of devices with/without Au nanostructures under illumination after a month.

Table 4.3 Comparison of performance of OPV devices with/ without Au nanostructures under illumination after a month.

Device	**PCE (%)**	**FF (%)**	**Jsc (mA/cm^2)**	**Voc (V)**
Pristine	12.06	39.28	47.95	0.64
Device_AuNSs	0.017	7.31	24.43	0.009
Device_AuNRs	5.07	29.25	36.03	0.48
Device_AuNPrisms	5.02	37.81	50.80	0.26

In conclusion, we reported the properties of synthesized Au nanostructures (nanospheres, nanorods, and nanoprisms) by the seed-mediated growth method. These Au nanostructures were successfully incorporated into the active layer PCDTBT: $PC_{70}BM$ and characterized. The optical, structural, and morphological properties of TiO_2 (ETL) and PEDOT: PSS (HTL) were studied. Furthermore, the current density (J-V) characteristics of the fabricated ITO/ TiO_2/ PCDTBT: $PC_{70}BM$/ PEDOT: PSS/Ag organic solar cells with and without Au nanostructures under illumination with 100 mW.cm^{-2} and electrical properties were obtained. The solar cell parameters of the plasmonic device were lower compared to the pristine, this may be due to non-radiative recombination in the active layer. Hence, no plasmonic enhancement was observed when the devices were measured after fabrication. The J-V characteristics results changed when measured after a month. The J_{sc} and V_{oc} increased which caused the efficiency of the pristine and device with AuNSs to increase. LSPR effect was observed due to the increase in J_{sc}. On the other hand, no plasmonic enhancement was obtained from devices with AuNRs and Au nanoprisms due to the decrease in PCE, FF, J_{sc}, and V_{oc}. When the pixel area was changed from 0.010 to 0.001 cm^2, the solar cell parameters of the same samples changed drastically. The pristine, devices with AuNRs and Au nanoprisms showed an enhancement in PCE, FF, J_{sc}, and V_{oc}. While the device with AuNSs all the parameters decreased significantly. This could be due to the change in the pixel area.

References

1. Zhuang, Y., et al., *Size and Shape Effect of Gold Nanoparticles in "Far-Field" Surface Plasmon Resonance*. Particle & Particle Systems Characterization, 2019. **36**(1): p. 1800077.
2. Cramer, H.E., et al., *Shape-controlled gold nanoparticle synthesis*. 2013, ARMY RESEARCH LAB ABERDEEN PROVING GROUND MD WEAPONS AND MATERIALS RESEARCH ….
3. Chang, H.-H. and C.J. Murphy, *Mini gold nanorods with tunable plasmonic peaks beyond 1000 nm.* Chemistry of Materials, 2018. **30**(4): p. 1427-1435.
4. Sun, M., et al., *The effect of iodide on the synthesis of gold nanoprisms.* Journal of Experimental Nanoscience, 2015. **10**(17): p. 1309-1318.
5. Nima, Z.A., et al., *Bimetallic gold core–silver shell nanorod performance for surface enhanced Raman spectroscopy.* RSC advances, 2017. **7**(84): p. 53164-53171.
6. Shen, X., et al., *Conformal surface plasmons propagating on ultrathin and flexible films.* Proceedings of the National Academy of Sciences, 2013. **110**(1): p. 40-45.
7. Meng, L.-q., et al., *Preparation and plasmon resonance properties of Au nanorods and Au nanorods@ SiO 2.* Gold Bulletin, 2020. **53**(1): p. 31-37.
8. Ogundare, O.D., et al., *Crystallite size determination of thermally deposited Gold Nanoparticles.* Procedia Manufacturing, 2019. **30**: p. 173-179.
9. Murugesan, V.S., et al., *Characterization of organic thin film solar cells of pcdtbt: Pc71bm prepared by different mixing ratio and effect of hole transport layer.* International Journal of Photoenergy, 2015. **2015**.
10. Song, H.-J., et al., *Optical and electrical effects of nanobump structure combined with an undulated active layer on plasmonic organic solar cells.* Organic Electronics, 2019. **71**: p. 136-142.
11. He, Y., et al., *Improved power conversion efficiency of inverted organic solar cells by incorporating Au nanorods into active layer.* ACS applied materials & interfaces, 2015. **7**(29): p. 15848-15854.
12. Mohammadnezhad, M., et al., *Hybrid PCDTBT: PCBM: Graphene-Nanoplatelet Photoabsorbers.* Journal of The Electrochemical Society, 2020. **167**(13): p. 136504.
13. Fuchs, F., et al., *Vibrational Spectroscopy of a Low-Band-Gap Donor–Acceptor Copolymer and Blends.* The Journal of Physical Chemistry C, 2017. **121**(36): p. 19543-19547.
14. Cho, S., et al., *A thermally stable semiconducting polymer.* Advanced Materials, 2010. **22**(11): p. 1253-1257.
15. Huh, Y.H. and B. Park, *Interface-engineering additives of poly (oxyethylene tridecyl ether) for low-band gap polymer solar cells consisting of PCDTBT: PCBM 70 bulk-heterojunction layers.* Optics express, 2013. **21**(101): p. A146-A156.
16. Ba-Abbad, M.M., et al., *Synthesis and catalytic activity of TiO2 nanoparticles for photochemical oxidation of concentrated chlorophenols under direct solar radiation.* Int. J. Electrochem. Sci, 2012. **7**(6): p. 4871-4888.
17. Theivasanthi, T. and M. Alagar, *Titanium dioxide (TiO2) nanoparticles XRD analyses: an insight.* arXiv preprint arXiv:1307.1091, 2013.
18. Challagulla, S., et al., *Structure sensitive photocatalytic reduction of nitroarenes over TiO 2.* Scientific reports, 2017. **7**(1): p. 1-11.
19. Su, W., et al., *Surface phases of TiO2 nanoparticles studied by UV Raman spectroscopy and FT-IR spectroscopy.* The Journal of Physical Chemistry C, 2008. **112**(20): p. 7710-7716.

20. Frank, O., et al., *Raman spectra of titanium dioxide (anatase, rutile) with identified oxygen isotopes (16, 17, 18).* Physical Chemistry Chemical Physics, 2012. **14**(42): p. 14567-14572.
21. Al-Oubidy, E.A. and F.J. Kadhim, *Photocatalytic activity of anatase titanium dioxide nanostructures prepared by reactive magnetron sputtering technique.* Optical and Quantum Electronics, 2019. **51**(1): p. 23.
22. Parreira, P., et al., *Dye-sensitized 1D anatase TiO2 nanorods for tunable efficient photodetection in the visible range.* Sensors and Actuators B: Chemical, 2012. **161**(1): p. 901-907.
23. Mustafa, M., et al., *Fabrication and characterization of organic light emitting diodes by using solution processable conjugated polymer.* Journal of nanoelectronics and optoelectronics, 2013. **8**(4): p. 343-348.
24. Susanti, E. and P. Wulandari. *Effect of localized surface plasmon resonance from incorporated gold nanoparticles in PEDOT: PSS hole transport layer for hybrid solar cell applications*. in *Journal of Physics: Conference Series*. 2018. IOP Publishing.
25. Chiu, W.W., et al., *Studies of dopant effects in poly (3, 4-ethylenedi-oxythiophene) using Raman spectroscopy.* Journal of Raman Spectroscopy: An International Journal for Original Work in all Aspects of Raman Spectroscopy, Including Higher Order Processes, and also Brillouin and Rayleigh Scattering, 2006. **37**(12): p. 1354-1361.
26. Xiong, S., L. Zhang, and X. Lu, *Conductivities enhancement of poly (3, 4-ethylenedioxythiophene)/poly (styrene sulfonate) transparent electrodes with diol additives.* Polymer bulletin, 2013. **70**(1): p. 237-247.
27. Kumar, P., et al., *Polymer morphology and interfacial charge transfer dominate over energy-dependent scattering in organic-inorganic thermoelectrics.* Nature communications, 2018. **9**(1): p. 1-10.
28. Sayyad, P.W., et al., *Chemiresistive SO 2 sensor: graphene oxide (GO) anchored poly (3, 4-ethylenedioxythiophene): poly (4styrenesulfonate)(PEDOT: PSS).* Applied Physics A, 2020. **126**(11): p. 1-8.
29. Gendron, D. and M. Leclerc, *New conjugated polymers for plastic solar cells.* Energy & Environmental Science, 2011. **4**(4): p. 1225-1237.
30. Wong, T.K., *Effect of embedded nanoparticle surface chemistry on plasmonic organic photovoltaic devices.* Materials for Renewable and Sustainable Energy, 2017. **6**(1): p. 4.
31. D'Olieslaeger, L., et al., *Tuning of PCDTBT: PC71BM blend nanoparticles for eco-friendly processing of polymer solar cells.* Solar Energy Materials and Solar Cells, 2017. **159**: p. 179-188.
32. Gusain, A., et al. *Investigation on the effects of thermal annealing on PCDTBT: PCBM bulk-heterojunction polymer solar cells*. in *AIP Conference Proceedings*. 2013. American Institute of Physics.
33. Qiao, L., et al., *Localized surface plasmon resonance enhanced organic solar cell with gold nanospheres.* Applied Energy, 2011. **88**(3): p. 848-852.
34. Puetz, A., et al., *Solution processable, precursor based zinc oxide buffer layers for 4.5% efficient organic tandem solar cells.* Organic Electronics, 2012. **13**(11): p. 2696-2701.
35. Namkoong, G., et al., *Active layer thickness effect on the recombination process of PCDTBT: PC71BM organic solar cells.* Organic Electronics, 2013. **14**(1): p. 74-79.
36. Liu, K., et al., *Efficient hybrid plasmonic polymer solar cells with Ag nanoparticle decorated TiO 2 nanorods embedded in the active layer.* Nanoscale, 2014. **6**(11): p. 6180-6186.

37. Spyropoulos, G.D., et al., *Organic bulk heterojunction photovoltaic devices with surfactant-free Au nanoparticles embedded in the active layer.* Applied Physics Letters, 2012. **100**(21): p. 213904.
38. Wang, D.H., et al., *Enhanced power conversion efficiency in PCDTBT/PC70BM bulk heterojunction photovoltaic devices with embedded silver nanoparticle clusters.* Advanced Energy Materials, 2011. **1**(5): p. 766-770.
39. Wu, B., et al., *Efficiency enhancement in bulk-heterojunction solar cells integrated with large-area Ag nanotriangle arrays.* The Journal of Physical Chemistry C, 2012. **116**(28): p. 14820-14825.
40. Street, R., K. Song, and S. Cowan, *Influence of series resistance on the photocurrent analysis of organic solar cells.* Organic Electronics, 2011. **12**(2): p. 244-248.
41. Moon, J.S., J. Jo, and A.J. Heeger, *Nanomorphology of PCDTBT: PC70BM bulk heterojunction solar cells.* Advanced Energy Materials, 2012. **2**(3): p. 304-308.

Chapter 5

Conclusion and future work

5.1 Conclusion

This study used a seed-mediated growth technique to synthesize gold (Au) nanostructures (nanospheres, nanorods, and nanoprisms). The main application, organic solar cells (OSCs) were fabricated and Au nanostructures were added between the electron transport layer (ETL) and the active layer. The objective of this study was to compare the effect of Au nanospheres, nanorods, and nanoprisms on the performance of PCDTBT: $PC_{70}BM$ based OSCs.

In section 4.2, Au nanostructures were synthesized by the seed-mediated growth method. Au nanospheres (NSs), nanorods (NRs), and nanoprisms were successfully synthesized. The variation of optical, morphological, and structural properties of Au nanostructures were presented and discussed. Transmission electron microscopy (TEM) and scanning electron microscopy (SEM) were used to study the surface morphology. TEM images revealed three different morphologies as AuNSs, AuNRs, and Au nanoprisms. The average diameter of Au seeds and AuNSs was 4 and 6 nm, respectively. An average edge length of 68 nm was observed for Au nanoprisms. The AuNRs that were well-formed had a length of 70 nm and a width of 40 nm (aspect ratio of 1.9). Similarly, SEM images revealed average grain sizes of these Au nanostructures 2.6, 15, 20, and 130 nm for Au seeds, AuNSs, Au nanoprisms, and AuNRs, respectively. The energy-dispersive X-ray spectroscopy (EDS) was used to confirm the presence of Au in all the samples. UV-Vis spectroscopy was used to study the optical properties of Au nanostructures. A redshift in the absorption spectra was noted, for Au seeds, nanospheres, nanorods, and nanoprisms. As the sizes of different Au nanostructures increased, the wavelength also increased with Au seeds being the smallest and AuNRs being the largest. The structural properties of Au nanostructures were studied using X-ray diffraction (XRD) and Raman spectroscopy. XRD studies revealed the face-centered cubic (fcc) crystalline structures of Au since the peaks were corresponding to miller indices planes. To confirm the crystalline structures, lattice parameters and crystallite sizes were calculated. All the samples showed strong and sharp Raman vibrational modes. It showed the maximum surface-enhanced Raman signal was obtained.

In section 4.3, structural, optical, and morphological properties of PCDTBT: $PC_{70}BM$ active layer, prepared using spin coating were reported. Au nanostructures such as AuNSs, AuNRs,

and Au nanoprisms were added into the active layer, and their properties were studied. UV-Vis spectroscopy was used to study the optical properties. The reference layer (PCDTBT: $PC_{70}BM$) showed three absorbance maxima at 378, 470, and 564 nm, which were similar to the layer with AuNSs. The reference layer and thin film with AuNSs samples showed very low intensity compared to the other samples. On the other hand, the thin film with AuNRs and Au nanoprisms showed absorption maxima at 380, 473, and 571 nm. Thin film with Au nanoprisms had a higher intensity compared to the other three samples. Raman spectroscopy was used to study the structural properties with the sample scan from 300 to 800 cm^{-1}. The observed vibrational modes were 573, 774, 1102, 1376, 1447, and 1596 cm^{-1} were observed and confirmed that the samples are polymer dominant. These results showed no crystalline domains present which indicated that the active layer is amorphous. To study the surface morphology of the active layer PCDTBT: $PC_{70}BM$ SEM was used. SEM images revealed that the active layer morphology was compact, the particles were well dispersed, and there were pin-hole defects. The calculated grain sizes were 17.28, 15.86, 34.51, and 20.23 nm for reference, thin film with AuNSs, AuNRs, and Au nanoprisms, respectively. EDS confirmed that the Au nanostructures were added to the active layer successfully.

In section 4.4, structural, optical, and morphological properties of titanium dioxide (TiO_2) thin film prepared by the spin-coating method. XRD and Raman spectroscopy were used to study the structural properties. From XRD, 2θ diffraction peaks at 25, 37, 51, 61, 70, and 78º corresponding to (101), (004), (200), (105), (204), (220) and (301) planes, respectively which confirms the anatase phase of TiO_2. Also, the crystallite size and lattice parameters confirmed the tetragonal crystal structure of TiO_2. Furthermore, Raman spectroscopy showed four characteristics of Raman active modes with symmetries E_g, B_{1g}, $A_{1g,}$ and E_g corresponding to 153, 406, 525, and 648 cm^{-1}. These characteristics vibrational frequencies and their intensities confirmed the anatase TiO_2 phase. UV-Vis absorption was used to measure the absorbance of TiO_2 thin films. It was observed that the TiO_2 film had a high absorbance in the ultraviolet region with the absorption maxima of 313 nm, hence it was used as the ETL in the solar cell. SEM images presented the anatase TiO_2 surface morphology which indicated that the particles are uniformly distributed, compact, and homogenous. The calculated grain size was 14.61 nm.

Section 4.5 reported the properties of the PEDOT: PSS thin film which was prepared by a spin coating method. The PEDOT: PSS was used as a hole transport layer. The absorption spectrum of the PEDOT: PSS thin film showed an absorbance peak at 310 nm. Raman

spectroscopy revealed vibrational peaks at 1254, 1443, 1508, and 1570 cm^{-1} and these attributed to C_α - C_α' inter-ring stretching, $C_\alpha = C_\beta$ symmetric stretching, and asymmetrical stretching vibration, respectively. For XRD, no diffraction peaks were observed due to the amorphous nature of PEDOT: PSS. The SEM images of PEDOT: PSS showed a homogenous and good morphology.

Section 4.6, the results of fabricated ITO/ TiO_2/ PCDTBT: $PC_{70}BM$/ PEDOT: PSS/Ag organic solar cells with and without Au nanostructures were reported. The current density (J-V) characteristics were determined under illumination. The power conversion efficiency (PCE) of the pristine device observed was 2.04% and plasmonic devices with AuNSs, AuNRs, and Au nanoprisms showed lower PCE results. This was attributed to the low J_{sc}, V_{oc}, and FF which is due to the increase in carrier recombination of the active layer and the nanostructured layer. These results were determined when measurements were done immediately after fabrication. Hence, no plasmonic enhancement was observed when the devices were measured after fabrication. Moreover, the J-V characteristics of the same devices when measured after a month showed different results. The pristine and device with AuNSs showed that J_{sc} and V_{oc} increased which enhanced the PCE from 2.04, 1.19 to 2.80 and 1.72%, respectively. Even though, for the plasmonic device with AuNSs the efficiency increased, it was still lower than the pristine. On the other hand, the plasmonic devices with AuNRs and Au nanoprisms revealed a decrease in FF, $J_{sc,}$ and V_{oc}, which caused the efficiency to decrease. LSPR effect was observed due to the increase in J_{sc} for the device with AuNSs. On the other hand, no plasmonic enhancement was obtained from devices with AuNRs and Au nanoprisms were observed. We also reported the J-V characteristics of the same devices when the pixel area was changed from 0.010 to 0.001 cm^2 in the I-V solar system settings. The change in pixel area increased the J_{sc}, FF, and V_{oc} which enhanced the PCE drastically from 2.80 to 12.06% for the pristine device. In the same way, in the plasmonic devices with AuNRs and Au nanoprisms the PCE increased significantly from 0.83, 0.23% to 5.07 and 5.02%, respectively. It was observed that the J_{sc} increased for both devices and V_{oc} increased for a device with AuNRs and decreased for Au nanoprisms device. Although the PCE increased, it is still lower than the pristine device and this may be due to the increase of carrier recombination, pin-holes defects in the active layer, and high series resistance. A drastic decrease in PCE, FF, J_{sc}, and V_{oc} values was observed for a device with AuNSs, compared to the other devices. This may be due to the change of the pixel area.

In summary, PCDTBT: $PC_{70}BM$-based organic solar cells with the addition of AuNSs, AuNRs, and Au nanoprisms between the ETL and active layer were prepared and characterized. The addition of Au nanostructures resulted in poor performance of the devices which could be due to the limitations (such as pinholes, annealing temperature, and thickness of the active layer) was observed. However, enhancement of the device performances increased after a month for the pristine and device with AuNSs. In addition, the change in pixel area affected the performance drastically for the pristine, device with AuNRS and Au nanoprisms. From the measurements of electrical properties, the device with AuNSs performs better than the other plasmonic devices, even though, the device with AuNRs showed better performance when the pixel area was changed. We conclude that the optical absorption is related to the photocurrent in plasmonic OSCs which is due to the near-field enhancement of the LSPR of Au nanostructures. We suggest that plasmonic Au nanostructures can be used to improve the performance of OSCs with minimal limitations.

5.2 Future work

From the present study, some of the gaps need to be addressed. There is a need to investigate the aging of PCDTBT: $PC_{70}BM$ based organic solar cells and study their electrical properties. The performance of devices seems to increase overtime so time may be a good factor for efficiency. More efforts are to be done in replacing PEDOT: PSS to improve the surface morphology which affects the performance of the solar cell. PEDOT: PSS is acidic and need to be replaced.